ONE- AND TWO-PHOTON STATES FOR QUANTUM INFORMATION

BY

NICHOLAS A. PETERS

B.A., Hillsdale College, 2000
M.S., University of Illinois at Urbana-Champaign, 2002

DISSERTATION

Submitted in partial fulfillment of the requirements
for the degree of Doctor of Philosophy in Physics
in the Graduate College of the
University of Illinois at Urbana-Champaign, 2006

Urbana, Illinois

ONE- AND TWO-PHOTON STATES FOR QUANTUM INFORMATION

Nicholas A.Peters
Department of Physics
University of Illinois at Urbana-Champaign, 2006
Prof. Paul G. Kwiat, Adviser

Using correlated photons from parametric downconversion, we extend the boundaries of experimentally explored one- and two-qubit Hilbert space. These states are used to explore a variety of topics in quantum information. Specifically, we have created and characterized arbitrary single-qubit states and maximally entangled mixed states (MEMS) that lie above the Werner-state boundary in the linear entropy-tangle plane. In addition, we demonstrate that such states can be efficiently concentrated via a "Procrustean method," simultaneously increasing both the purity and the degree of entanglement.

Our experimental MEMS creation directed us to examine several ways of benchmarking states in the presence of perturbations, comparing the relative sensitivity between the common state measures–fidelity, trace distance, concurrence, tangle, von Neumann entropy, and linear entropy. In particular, we illustrate a sensitivity imbalance between three of these measures for depolarized MEMS and nonmaximally entangled states. Surprisingly, the size of the imbalance depends on the state's tangle and linear entropy.

Using maximally entangled states, we experimentally demonstrate the first remote state preparation of arbitrary single-qubit states, at two wavelengths. Further, we derive theoretical bounds on the states that may be remotely prepared for given two-qubit resources. By using methods for directly and remotely preparing arbitrary single-qubit states, we make the first optical mixed-state geometric phase measurement via single-photon interferometry. Finally, we present experimental progress on the remote preparation of single-photon number states, created deterministically out of a non-deterministic spontaneous parametric downconversion source.

To my father James John Peters
and in loving memory of my mother,
Mary Elaine Peters
August 11, 1944-August 28, 2003.

Acknowledgments

I have been fortunate to work with many talented individuals and I would like to acknowledge all of my collaborators (in alphabetical order): Daryl Achilles, Joe Altepeter, Kyle Arnold, Prof. David Branning, Marie Ericsson, Prof. Mike Goggin, Prof. Paul Goldbart, Onur Hosten, Prof. Daniel James, Nathan Langford, Swagatam Mukhopadhyay, Matt Rakher, Radhika Rangarajan, Aaron VanDevender, and Joe Yasi. The discussions I have had with these individuals have helped to evolve the way I view science and the world.

Complementing the list above, I must give special thanks to several people. I have to thank my advisor Paul Kwiat who always made time for discussions and aligning interferometers. Paul has been a great mentor and has done a great deal to help me develop as a scientist and as a person. It is rare that an advisor so often stops by the lab after midnight to see how an experiment was progressing and offer encouragement. On more than one occasion, Paul and I pulled joint all-nighters. I thank Tzu-Chieh Wei for invaluable theoretical assistance on our projects. We have worked very closely on many of the theoretical studies that are contained in this dissertation. I thank Evan Jeffrey for going beyond the call of duty by helping resolve my computer hardware and software issues. I thank Julio Barreiro-Guerrero for our experimental synergy and spending more time in the lab with me than any other person. I would like to thank several professors from Hillsdale College for giving me the tools required and encouragement to succeed in graduate school: Kathy Andrews, Dean Evasius, Ken Hayes, Bob Hesse, Paul Lucas, Jim Peters, Jack Reinoehl, Adam Smith and Mark Watson. I thank Bill Vincent, my middle school science teacher and Science Olympiad coach who had a strong and lasting influence on me.

I thank all American Taxpayers who have provided funding for my graduate study through the following: the Department of Physics through a GAAN fellowship, the National Science Foundation (Grant No. EIA-0121568), the MURI Center for Photonic Quantum Information Sys-

tems (ARO/ARDA program DAAD19-03-1-0199), and the U.S. Army Research Office (Grant No. DAAD19-03-1-0282), and the Disruptive Technologies Office (funding the MURI and ARO grants).

I would like to thank the NTT corporation for funding and organizing the NTT/BRL Quantum Information Summer Science Camp in 2002. I also thank Prof. Yoshihisa Yamamoto for delivering most of the lectures and answering many questions. I very much enjoyed my time in Japan.

As for my friends, I thank Vassil Antonov, Saad Khairallah and Davit Sivil for our first year study group and international cooking explorations. I thank Amit Mehta and Swagatam Mukhopadhyay for their efforts to educate me culturally and for their support, especially in the early years of my time in Urbana. I thank Matt Brinkley for his friendship and support during the last several years. I thank my two oldest friends, Jon Doty and Seth Zeiler, for their support and encouragement. I also thank my friend Sascha Loy for expanding my cultural horizons.

I must thank my family who have lifted me up during the lows that come with research (and for that matter, life in general) and sharing successes. I thank my mother, Mary, for teaching me to do my best and be content with it. I thank my father, Jim, for teaching me physics and answering many, many questions over the years. I thank my brothers Joe, Charles and Chris and my sister Connie, my stepmother Debi Belt, my Uncle Loren, and my grandparents for their support and encouragement.

Finally, saving the best for last, I thank my wife and best friend Theresa for her love, support, and encouragement.

Table of Contents

List of Tables

List of Figures

List of Abbreviations

$|A\rangle$ Antidiagonal

APD Avalanche Photodiode

BBO β-Barium Borate

BD Beam Displacer

CQV Continuous Quantum Variables

$|D\rangle$ Diagonal

F Fidelity

$|H\rangle$ Horizontal

HWP Half-wave Plate

IF Interference Filter

$|L\rangle$ Left Circular

LC Liquid Crystal

MEMS Maximally Entangled Mixed States

QWP Quarter-wave Plate

$|R\rangle$ Right Circular

RSP Remote State Preparation

S_L Linear Entropy

SPDC Spontaneous Parametric Downconversion

SPS Single-Photon Source

T Tangle

$|V\rangle$ Vertical

Chapter 1

Introduction

Over the past decade there has been a great deal of interest in the application of quantum mechanics to disciplines not directly associated with physics. This interest has given rise to the multidisciplinary fields of quantum computation and quantum information. There have been many fascinating proposals that use the rules of quantum mechanics to manipulate information. As nearly all quantum information protocols require specific initial states and the ability to manipulate the qubits with exquisite precision, the effectiveness of these proposals often hinges on the quality of the initial quantum bits or qubits. Often, the required resource for quantum information is entanglement. And generally the entropy (or lack of it) and the entanglement of resource qubits are critical indicators of the successful implementation of a particular protocol.

Quantum computation gained popularity after the discovery of Shor's factoring algorithm [1] and Grover's search algorithm [2, 3]. A central feature of both algorithms is the use of a superposition of states. Shor's factoring algorithm displays an exponential speedup over the best known classical factoring algorithm. Grover's search achieves a quadratic speedup over classical limits in the search of an unordered list. Although superposition is necessary for the construction of a quantum computer, it is currently uncertain if entanglement is required as well, though it seems likely that it is. In any event, entanglement is certainly important for myriad other quantum information applications such as quantum dense coding [4, 5] and quantum teleportation [6].

The theoretical discovery of quantum algorithms has motivated a search for realizable systems for their implementation. Proposed implementations for a quantum computer are numerous, including: nuclear spins in silicon [7], bulk spin resonance with NMR [8], quantum dots [9], trapped ions [10], Josephson junctions [11], and linear optics [12]. Much like classical computation, the following steps are required in its quantum analogue: the ability to create a given initial state, manipulate the state to perform the given computation, and then read resulting output. All this must occur before the environment has time to degrade the quality of the computation state. Often the same coupling that is used for state manipulation exists as background noise causing state decoherence. Sometimes, it is possible to select a subspace that is more resistant to decoherence [13]. In cases where decoherence causes unavoidable information loss, one may use quantum error correction to lengthen the quantum memory of a state [14, 15]. In any case, to avoid decoherence and minimize information loss, one needs a thorough understanding of the state space of a given experimental implementation. It is our purpose to understand the state space of photon pairs created by spontaneous parametric downconversion and apply that understanding to study several problems.

1.1 Entanglement

Just as classical computers have bits 0 or 1, quantum computers have their own quantum bit analog, qubits. A qubit is any two-level quantum system whose states can be expresses as a linear combination of two orthogonal states, $|0\rangle$ and $|1\rangle$. A powerful feature of qubits is the ability to build superposition states such as $(|0\rangle + |1\rangle)/\sqrt{2}$. While superposition also exists in classical physics-e.g., leading to interference effects, qubits can exhibit additional characteristics representing gradually greater departures from classical understandings of nature, including interference, wave-particle duality, intrinsic randomness in measurement and entanglement.

Two or more qubits may exhibit nonclassical correlations due to entanglement, a resource present in some two-qubit superposition states. A pure entangled two-qubit state is a superposition of pure product states such that neither qubit carries a definite value, yet when one qubit's value is determined, its partners state is also determined[1]. Such a superposition cannot be represented as the product of any two one-qubit states. For example, the spin-$\frac{1}{2}$ singlet state $(|\uparrow\downarrow\rangle - |\downarrow\uparrow\rangle)/\sqrt{2}$ cannot be represented as a product of single qubit states. If one measures the state of the first spin to be $|\uparrow\rangle$ $(|\downarrow\rangle)$, then the second spin will be found in the state $|\downarrow\rangle$ $(|\uparrow\rangle)$. One must carefully

---

[1] Strictly speaking, in the general case of nonmaximal entanglement, the partner qubit's state is only partially determined.

observe that the measurement on the first spin is equally likely to give up or down and that this randomness prevents using entanglement for superluminal communication.

What makes a particular implementation a good choice for a qubit? The answer depends on how one wants to use the qubit. If one wanted to store information in a fixed location then an atomic state would be a good choice, owing to long coherence times. For creating controllable interactions between scalable qubits, a good choice would be spins in silicon [7]. However, if one wants to send information over long distances, a more suitable choice might be to encode the desired information into one or more degrees of freedom of a photon.

Photonic qubits have some advantages and some disadvantages (which are not mutually exclusive) for quantum information. One advantage is that they travel quickly, which is good for sending but poor for storing information. Photonic qubits are relatively resilient against decohering effects because they do not couple strongly to the environment. This is however a disadvantage for quantum computation, where the lack of strong photon-photon interactions makes realizing efficient quantum gates a difficult proposition.

One can encode a qubit in one or more photonic degrees of freedom, including polarization, energy-time, or momentum. For our primary system, qubits are encoded into the polarization of light, due to the relative ease of its control and measurement. A complete orthonormal polarization basis consists of horizontal ($|H\rangle$) and vertical ($|V\rangle$) states (or *any* two different polarization states). Using this notation, the two-qubit entangled states introduced by Bell [16] may be written as:

$$|\Psi^{\pm}\rangle = (|HV\rangle \pm |VH\rangle)/\sqrt{2}, \tag{1.1}$$

$$|\Phi^{\pm}\rangle = (|HH\rangle \pm |VV\rangle)/\sqrt{2}. \tag{1.2}$$

Although here we concentrate on discrete systems, it is worth noting that entanglement of continuous quantum variables (CQV) has recently been experimentally investigated [17], and there exist continuous analogs for many discrete variable protocols, such as teleportation [18] and error correction [19]. Lloyd and Braunstein proposed CQV computation, indicating that some tasks may be more efficient with CQV computing [20].

1.2 Overview

The goal of this dissertation is to describe how quantum states can be created and manipulated for quantum information[2]. Primarily, polarization will be used as the degree of freedom in which the qubit is encoded. In Chapter 2, we show how to create arbitrary single-qubit polarization states. Chapter 3 includes preliminaries on entanglement creation and characterization. Chapter 4 describes the generation of polarization-entangled photon pairs which will be used for several experiments, the first of which is the creation of maximally entangled mixed states (MEMS). With the MEMS, we will examine an efficient way to reduce mixedness and increase entanglement by using a "Procrustean" concentration scheme. Surprisingly, MEMS could be created having ∼0.99 fidelity with the theoretical goal (excellent agreement by most standards), but the target entanglement and entropy seemed farther off than anticipated. Chapter 5 discusses these discrepancies and several examples that illustrate how the fidelity is less sensitive to perturbations than other common state benchmarks.

In Chapter 6 we discuss the implementation of remote state preparation (RSP), a quantum communication protocol that is potentially simpler than teleportation. In RSP Alice can send a known state to her partner Bob by making a projective measurement on her half of an entangled pair shared with Bob and sending him only one bit of classical communication. We show how one may remotely prepare arbitrary qubits encoded in the polarization state of single photons by making *arbitrary* polarization projections with an arbitrary *strength*. Using techniques outlined in Chapter 2 and another form of RSP to generate mixed states, we describe the first optical measurement of mixed state geometric phases in Chapter 7. This is particularly interesting because the two ways we produce mixed states are conceptually different yet, the measured geometric phase is the same.

As sources of single photons would be useful for quantum cryptography and are required for the Knill-Laflamme-Milburn linear optics quantum computing scheme [12], Chapter 8 outlines another type of RSP, that of photon number states. Specifically, we discuss progress on the preparation of deterministic single-photon states using spontaneously generated photon pairs.

After drawing conclusions and suggesting extensions of this research in Chapter 9, we include

---

[2] This thesis is heavily based on a collection of our papers, organized and expanded upon for clarity. At the beginning of each chapter, we give the references of the relevant publications from which we adopt much of the text and many of the figures.

two appendices. Appendix A details calculations leading to the selection of the β-Barium Borate (BBO) nonlinear crystals used to generate photons. Appendix B gives a somewhat more rigorous theoretical basis for decohering with birefringent elements, which is used in Chapters 2, 4 and 8.

As this research is collaborative effort, we have attempted to give credit to those who have made significant contributions throughout this document, where appropriate. We include these contributions so that a coherent story may be presented. If we have overlooked any of these, it is certainly not intentional.

Chapter 2

Single-photon polarization states

2.1 Introduction

The basic element of quantum information is the qubit—most protocols require precise fiducial[1] qubits as the inputs. In particular for quantum communication experiments, photons are ideal information carriers due to the speed with which they travel and the fact that they are relatively robust against decoherence.

In this chapter we present the theoretical basis for and experimental verification of arbitrary single-qubit state generation, using the polarization of photons generated via spontaneous parametric downconversion, initially presented in [21]. Single-photon Fock states are conditionally realized by detecting one photon of a pair produced in the process of spontaneous parametric downconversion [22]. We manipulate the photons' polarization state using a series of birefringent wave plates (which enable a unitary transformation to any pure polarization state) and a thick birefringent decoherer (which allows the production of mixed states). Using a method of state tomography, we can experimentally determine the most likely density matrix that describes the resulting quantum state. Our precision measurement and state-reconstruction system has the capability to distinguish over 3 million states, all of which can be reproducibly generated using our state creation apparatus.

---

[1] Input qubits must have a trusted form otherwise an error in an input state could lead to even greater errors in the performance of the protocol.

2.2 Photons from spontaneous parametric downconversion

We create pairs of photons using spontaneous parametric downconversion (SPDC). To better understand this process, we first briefly discuss the relevant nonlinear optics. Nonlinear electromagnetic interactions depend on the fields involved, the type of material, and the orientation of the field with respect to the material. Generally, nonlinear materials are characterized by an expansion of the electromagnetic susceptibility χ in powers of the electric field. The i^{th} polarization component of light inside such a material is related to the electric field components E_i by:

$$P_i \;=\; \chi_{ij}^{(1)} E_j \;+\; \chi_{ijk}^{(2)} E_j E_k \;+\; \cdots \tag{2.1}$$

Our photon source is based on SPDC, first observed over 33 years ago [23]. It is governed by the lowest order perturbation from the linear response and as such is proportional to the second order susceptibility $\chi_{ijk}^{(2)}$. A pump photon with frequency ω_p interacts with a nonlinear crystal to generate daughter photons of frequency ω_1 and ω_2 such that energy is conserved:

$$\omega_1 \;+\; \omega_2 \;=\; \omega_p. \tag{2.2}$$

Similarly, momentum inside the crystal is conserved via the phase matching condition. To see an example calculation on phase matching, see Appendix B. SPDC leads to pairwise creation of photons according to:

$$|\Psi_{downconversion}\rangle = |00\rangle + \epsilon|11\rangle + \epsilon^2|22\rangle + \ldots, \tag{2.3}$$

where $|00\rangle$ is the no photon state, $|11\rangle$ is the creation of one photon in each of two different modes and $|22\rangle$ is the creation of two photons in each mode. The number ϵ is determined by the effective nonlinearity (which depends on $\chi_{ijk}^{(2)}$ and the phase matching conditions), the length of the crystal used and the intensity of the pump laser. In practice, ϵ is very small, so we collect only one pair of daughter photons in modes of interest for every 10^{14} pump photons passing though the nonlinear crystal under typical conditions in our experiments. We postselect the $|11\rangle$ term by detecting one photon in each of two detectors. As ϵ is small, the yet higher-order photon number terms are negligible. When one member of $|11\rangle$ is detected, the other mode is, to a very good approximation, in a single-photon Fock state [22].

2.3 Single-qubit state representation

We encode our logical qubits in the horizontal and vertical polarizations of single-photons,

$$|0\rangle \equiv |H\rangle \text{ and } |1\rangle \equiv |V\rangle. \tag{2.4}$$

Unless otherwise noted, we write the polarizations in the horizontal-vertical basis using

$$|H\rangle \Leftrightarrow \begin{pmatrix} 1 \\ 0 \end{pmatrix} \text{ and } |V\rangle \Leftrightarrow \begin{pmatrix} 0 \\ 1 \end{pmatrix}, \tag{2.5}$$

or in density matrix notation,

$$\rho_H = \begin{pmatrix} 1 & 0 \\ 0 & 0 \end{pmatrix} \text{ and } \rho_V = \begin{pmatrix} 0 & 0 \\ 0 & 1 \end{pmatrix}. \tag{2.6}$$

The density matrix of an arbitrary single qubit can be represented by three independent real parameters (A, B, and δ):

$$\rho = \begin{pmatrix} A & Be^{i\delta} \\ Be^{-i\delta} & 1-A \end{pmatrix}, \tag{2.7}$$

where $0 \leq$ A ≤ 1, and $|B| \leq \sqrt{A(1-A)}$ from positive semi-definiteness. Another equivalent representation is given by

$$\rho = \tfrac{1}{2}(\mathbb{1} + \vec{r} \cdot \vec{\sigma}), \tag{2.8}$$

where $\sigma_0 \equiv \mathbb{1}$ is the 2x2 identity matrix and we define the polarization analogs of the Pauli spin matrices as

$$\sigma_1 \equiv \begin{pmatrix} 0 & 1 \\ 1 & 0 \end{pmatrix}, \ \sigma_2 \equiv \begin{pmatrix} 0 & -i \\ i & 0 \end{pmatrix}, \text{ and } \sigma_3 \equiv \begin{pmatrix} 1 & 0 \\ 0 & -1 \end{pmatrix}. \tag{2.9}$$

The components of $\vec{r}$ give the degree of polarization for the photon in the Horizontal-Vertical (H-V), Diagonal-Antidiagonal (D-A), and Right-Left Circular (R-L) bases. These components r_i

are related to the Stokes parameters (S_i) of classical optics [24] by $r_i = \frac{S_i}{S_0}$. As such, they are often identified as the real parameters $r_H \equiv r_1$, $r_D \equiv r_2$, $r_R \equiv r_3$. The conversion between the representations in (2.7) and (2.8) is given by $r_H = 2A - 1$, $r_D = 2B\cos(\delta)$, and $r_R = 2B\sin(\delta)$.

2.4 The Poincaré sphere

It is useful to view the previous components as coordinates in a 3-D space of polarizations; the constraint $|\vec{r}| \leq 1$ implies that all states must lie inside or on a sphere of unit radius, known as the Poincaré sphere. Points on the *surface* of the sphere ($|\vec{r}| = 1$) represent pure polarization states (linear polarization states on the equator, right and left circular polarization on the north and south pole, respectively), whereas points inside the surface ($|\vec{r}| < 1$) represent partially mixed states. The center of the sphere ($|\vec{r}| = 0$) corresponds to a completely mixed state, i.e., an unpolarized photon.

2.5 Arbitrary qubits

Because an arbitrary state has three independent parameters, the generation of such a state requires at least three adjustable elements. Considering the Poincaré sphere, we make an ansatz that a half-wave plate (HWP), followed by a thick birefringent decoherer, a half-wave plate, and a quarter-wave plate (QWP) are sufficient to generate all one-qubit polarization states from a pure linear polarization fiducial state ($|H\rangle$ in our case).

We now derive formulae that give wave plate settings for an arbitrary state, thus proving our ansatz. The operators that represent the action of half- and quarter-wave plates, respectively, are the Jones matrices [25]

$$\mathbf{O}_{HWP}(\theta) \equiv \begin{pmatrix} -\cos 2\theta & -\sin 2\theta \\ -\sin 2\theta & \cos 2\theta \end{pmatrix} \tag{2.10}$$

and

$$\mathbf{O}_{QWP}(\theta) \equiv \begin{pmatrix} 1-(1+i)\cos^2\theta & -(1+i)\sin\theta\cos\theta \\ -(1+i)\sin\theta\cos\theta & 1-(1+i)\sin^2\theta \end{pmatrix}, \tag{2.11}$$

where in each case the parameter θ is the angle that the optic axis makes with horizontal.

To create arbitrary states as in (2.7), we can start with photons in the state ρ_H, and direct

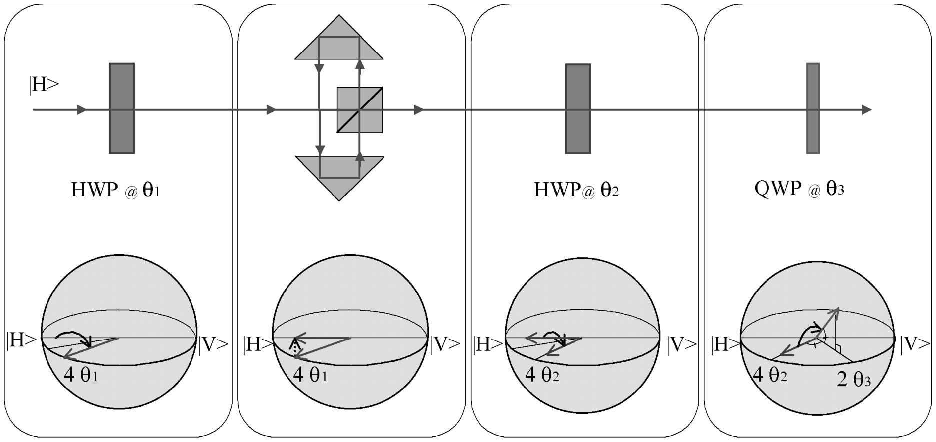

Figure 2.1: The experimental setup to realize an arbitrary single (polarization) qubit, along with the representation of the state in the Poincaré sphere at each step of state preparation. In the first stage, on the left, horizontally polarized photons are sent through a half-wave plate (HWP) with an optic axis at θ_1 from horizontal, giving the linear polarization state $|2\theta_1\rangle$. This is then sent through a decoherer that has an optical path-length difference greater than the coherence length of the photon. One method to achieve such a decoherer is with a polarizing beam splitter that sends vertical polarization in a delay loop while horizontal is transmitted, thereby suppressing the phase coherence in the horizontal-vertical basis (see Appendix A), and eliminating any amplitude in the off-diagonal elements of the state. Decoherence in the Poincaré sphere appears as a projection of the state onto the $|H\rangle - |V\rangle$ "spindle" (second box). By appropriately adjusting the first HWP, states with arbitrary mixedness can be produced, ranging from a pure state ($|\vec{r}| = 1$) to a completely mixed state ($|\vec{r}| = 0$), i.e., unpolarized photons. The last two wave plates, a HWP and a quarter-wave plate (QWP), set the final direction of the (possibly mixed) state in the sphere.

them through a half-wave plate at θ_1, giving

$$\rho_{\mathbf{1}} \equiv \mathbf{O}_{HWP}(\theta_1)\rho_H\mathbf{O}_{HWP}(\theta_1)^\dagger = \begin{pmatrix} \cos^2 2\theta_1 & \cos 2\theta_1 \sin 2\theta_1 \\ \cos 2\theta_1 \sin 2\theta_1 & \sin^2 2\theta_1 \end{pmatrix} = |2\theta_1\rangle\langle 2\theta_1|, \qquad (2.12)$$

i.e., the pure linear polarization state $|2\theta_1\rangle$. As shown in the first box in Fig. 2.1, this operation is described on the Poincaré sphere by rotating the state $|H\rangle$ by 180° about an axis – representing the optic axis of the wave plate – that lies $2\theta_1$ away on the equator; the factor of 2 arises because $|V\rangle$ lies on the *opposite* side of the Poincaré sphere[2], i.e., 180° away from $|H\rangle$.

The next step is to introduce decoherence by separating the horizontal and vertical polarization components by an optical path-length difference much longer than the coherence length of the

---

[2] A very complete discussion of the use of the Poincaré sphere to describe the action of various crystal optics may be found in [26].

photons (see Appendix A) [27]. If the coherence length is longer than a few millimeters, one can use a polarization-dependent delay line, as shown in the second box of Fig. 2.1. For our downconversion source, interference filters at the detector typically define the spectral bandwidth; for filters with 10-nm full width at half maximum, the coherence length[3] is only $\sim$50-μm. In this case it suffices to use a thick birefringent element (e.g., 1 cm of quartz) to completely decohere the polarizations within the eigenbasis of the decohering element [27]. We can control the *amount* of decoherence by tuning the polarization of the input state. For example, if the polarization before entering the decoherer is $|H\rangle$ (or $|V\rangle$) then the state purity is preserved; if the input state is diagonally polarized, (i.e., $|D\rangle$), the resulting state is completely mixed. An arbitrary value of $|\vec{r}|$ is produced by setting the orientation of the first half-wave plate to $\theta_1 = \frac{1}{4}\arccos|\vec{r}|$. After the rotated light is directed through the birefringent decohering element, the reduced density matrix describing only the polarization is of the form (see Appendix A):

$$\rho'_{\mathbf{1}} = \begin{pmatrix} \cos^2 2\theta_1 & 0 \\ 0 & \sin^2 2\theta_1 \end{pmatrix}. \tag{2.13}$$

Next, using wave plates, we unitarily transform (2.13) into the desired final state. Note that (2.13) can be rewritten as an incoherent sum of a horizontally polarized pure state and an unpolarized, completely mixed state:

$$\rho'_{\mathbf{1}} = \cos 4\theta_1 |H\rangle\langle H| + 2\sin^2 2\theta_1 \rho_{mixed}\,, \tag{2.14}$$

where $\rho_{mixed} \equiv \frac{1}{2}\mathbb{1}$ is the completely mixed state. Because quantum mechanics is linear, we may operate individually on each part of this sum to obtain the final state. As the unpolarized part is unchanged by any unitary transformation, the final form of the state is determined by operating on the $|H\rangle\langle H|$ term with a half-wave plate (at θ_2) and a quarter-wave plate (at θ_3). Algebraically determining the desired values of θ_2 and θ_3 to obtain a particular final state is non-trivial. However, by noting the geometric action of these wave plates on the Poincaré sphere (see the third and fourth boxes of Fig. 2.1), one can arrive at the following final solutions for the wave-plate angles needed

---

[3] The coherence length is approximately $\frac{\lambda^2}{\delta\lambda}$ where λ is the wavelength of interest and $\delta\lambda$ the bandwidth.

to set the values of A, B, and δ that characterize the state (2.7)[4,5]:

$$
\begin{aligned}
\theta_1 &= \frac{1}{4}\arccos\left[\sqrt{(2A-1)^2+4B^2}\right], && (2.15)\\
\theta_2 &= \frac{1}{4}\left[\arctan\left[\frac{2B\cos[\delta]}{2A-1}\right]+\arctan\left[\frac{2B\sin[\delta]}{\sqrt{(2A-1)^2+4B^2\cos^2[\delta]}}\right]\right], && (2.16)\\
\theta_3 &= \frac{1}{2}\arctan\left[\frac{2B\cos[\delta]}{2A-1}\right]. && (2.17)
\end{aligned}
$$

Armed with these equations we set up our experiment as in Fig. 2.2. The process of spontaneous parametric downconversion conditionally prepares single-photon input states [22]. A nonlinear crystal (BBO) is pumped with a vertically polarized 351-nm beam from an Argon-ion laser (average power 86 mW). The BBO is cut to produce non-collinear frequency-degenerate horizontally polarized photon pairs at 702 nm via type-I phase matching[6]. The non-collinear photon pairs are collected in two modes, separated by 6° outside of the crystal (see Appendix B for more on phase matching). The first mode impinges on to a detector assembly consisting of a 10-nm FWHM interference filter (IF) centered at 702.2 nm, a lens (f = 35 mm), and an avalanche photodiode (APD) operated in Geiger mode (Perkin-Elmer #SPCM-AQR-14). Single-photon Fock states are prepared in the second arm conditional on a "trigger" count in the first detector [22]. The second mode passes through a polarizing beam splitter (PBS) (to ensure a good fiducial state $|H\rangle$), the state preparation wave plates[7] and decoherer (∼1 cm quartz slab) discussed above, a QWP-HWP-PBS combination for state analysis (see Section 2.5), a 2.2-mm iris (located ∼1.2 m from the BBO crystal), and a detector assembly identical to that in the first mode.

---

[4] In terms of the Poincaré sphere vector $\vec{r}$, we have

$$
\begin{aligned}
\theta_1 &= \frac{1}{4}\arccos\left(|\vec{r}|\right)\\
\theta_2 &= \frac{1}{4}\quad\arctan\left(\frac{r_D}{r_H}\right)+\arctan\left(\frac{r_R}{r_H^2+r_D^2}\right)\\
\theta_3 &= \frac{1}{2}\arctan\left(\frac{r_D}{r_H}\right).
\end{aligned}
$$

[5] In any real system, the various wave plates may have slight errors in their retardations. In this case, we must numerically search for the optimal wave-plate settings to create arbitrary states. If the QWP retardance error is larger than the HWP error, then arbitrary state creation may not be possible. For example, if a QWP has a 1°-phase error and the HWP is exactly 180°, one cannot create a state arbitrarily close to $|R\rangle$.

[6] The optic axis cut was 33.9°.

[7] All of the wave plates are in motor-controlled stages (Newport PR50CC), and can be set with an accuracy of better than 0.1°.

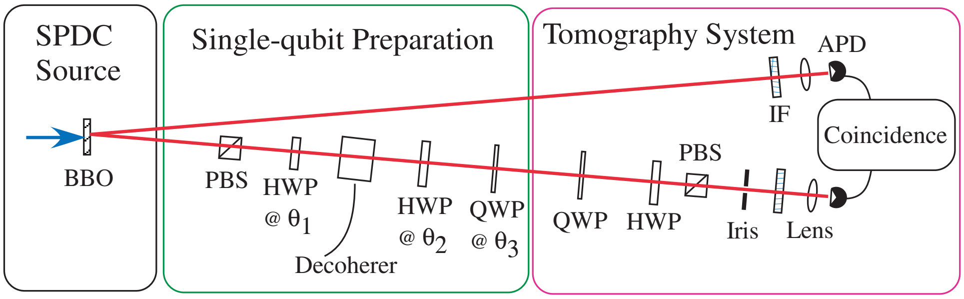

Figure 2.2: Single-qubit downconversion experiment. Detection of a photon in the upper arm conditionally prepares a single-photon state in the lower arm. The polarizing beam splitter (PBS) after the nonlinear BBO crystal[9] prepares an extremely pure initial state $|H\rangle$, which is then transformed by the wave plates and decoherer (∼1 cm quartz birefringent element). The tomography system allows an accurate measurement of the resulting density matrix ρ (see Section 2.5).

We created a variety of single-qubit states using this system. Some sample reconstructed density matrices (see Section 2.6) are shown in Fig. 2.3. One measure of our ability to accurately prepare specific states is the "fidelity," a measure of state overlap [28]. For two pure states, $|\psi_1\rangle$ and $|\psi_2\rangle$, e.g., a measured and a target state, the fidelity is simply $F(|\psi_1\rangle, |\psi_2\rangle) \equiv |\langle\psi_1|\psi_2\rangle|^2$, whereas for two general density matrices, ρ_1 and ρ_2, it is

$$F(\rho_1, \rho_2) \equiv |\mathrm{Tr}(\sqrt{\sqrt{\rho_1}\rho_2\sqrt{\rho_1}})|^2. \tag{2.18}$$

This is zero for two orthogonal states and one for identical states. We typically observed fidelities better than 0.997. In Section 2.6 we discuss the uncertainty in these measurements.

2.6 State characterization

One cannot determine the unknown polarization state of a photon with a single measurement. Instead, a large ensemble of photons prepared in an identical manner must be projected into different polarization basis states. A minimum of four measurements are needed – three to determine the relative values of the three independent parameters that characterize an unknown state, and a fourth to determine normalization. The polarization analysis is carried out by setting the quarter- and half-wave plates shown in the tomography system box of Fig. 2.2. Although there are (infinitely) many choices of the particular measurements that can be made (in principle, measuring along any three

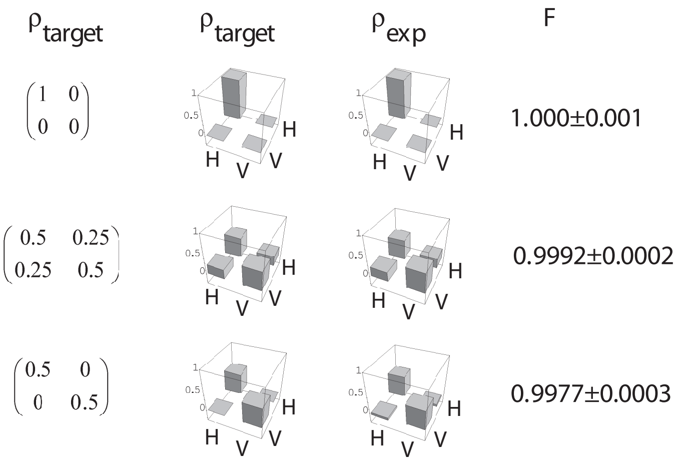

Figure 2.3: Single qubit data. Shown are the target density matrices, plots of the target and experimentally measured density matrices, and the fidelity (F) between them. The imaginary elements of the density matrices are not shown because they have zero amplitude for the target states, and are always less than 2% for the experimental states. The errors are due mostly to pump drift and statistical uncertainty, with the statistical uncertainty highest for the pure state.

non-collinear basis vectors would suffice), we choose the analysis states: $\langle\psi_0| \equiv \langle V|$, $\langle\psi_1| \equiv \langle H|$, $\langle\psi_2| \equiv \langle D|$, and $\langle\psi_3| \equiv \langle R|$ corresponding to N_0, N_1, N_2, and N_3 photon counts in some fixed measurement time interval (typically 100 s). As explained earlier, to obtain single-photon Fock states, we count in coincidence; thus, N_i are coincidence counts between the two detectors shown in Fig. 2.2. Since we need to estimate probabilities, we must measure a complete basis to normalize the photon counts. As $|H\rangle$ and $|V\rangle$ form a basis, $\mathcal{N} \equiv N_0 + N_1$ gives a convenient normalization factor for the r_i: $r_H = 2N_1/\mathcal{N} - 1$, $r_D = 2N_2/\mathcal{N} - 1$, and $r_R = 2N_3/\mathcal{N} - 1$. The density matrix of the state may then, in principle, be reconstructed as in (2.8).

Unfortunately, as this state reconstruction is necessarily based on photon counting, statistical fluctuations or drift often yield an unphysical result; therefore, we employ a maximum likelihood technique to estimate a physical density matrix that would most likely produce the measured data. James et al. describe the technique for determining the joint state of *two* qubits [29]. Here we distill their argument down to the one qubit case[10]

A physical density matrix representation has three cardinal properties: normalization, positive semidefiniteness, and hermiticity. Therefore, we first guess a density matrix that, by definition, has

---

[10] If states other than single-photon states are used, more sophisticated methods must be used to determine the quantum polarization state [30].

the aforementioned properties. A matrix that can be written as $\mathbf{T}^\dagger\mathbf{T}$ is positive semidefinite and hermitian [29]. To normalize such a matrix, we divide by its trace so that $\mathbf{T}^\dagger\mathbf{T}/\mathrm{Tr}(\mathbf{T}^\dagger\mathbf{T})$ has the three properties for a legitimate physical density matrix. We choose the following invertible form for $\mathbf{T}(\mathbf{t})$:

$$\mathbf{T}(\mathbf{t}) \equiv \mathbf{T}(t_0, t_1, t_2, t_3) \equiv \begin{pmatrix} t_0 & 0 \\ t_2 + it_3 & t_1 \end{pmatrix}. \tag{2.19}$$

Using (2.19), the density matrix formula is

$$\rho_p(t_0, t_1, t_2, t_3) = \mathbf{T}^\dagger(\mathbf{t})\mathbf{T}(\mathbf{t})/\mathrm{Tr}(\mathbf{T}^\dagger(\mathbf{t})\mathbf{T}(\mathbf{t})). \tag{2.20}$$

Next we will introduce a likelihood function that quantifies how similar $\rho_p(t_0, t_1, t_2, t_3)$ is to our experimental data:

$$\mathcal{L}(N_0, N_1, N_2, N_3; t_0, t_1, t_2, t_3) = \sum_{\nu=0}^{3} \frac{[\mathcal{N}\langle\psi_\nu|\rho_p(t_0, t_1, t_2, t_3)|\psi_\nu\rangle - N_\nu]^2}{2\mathcal{N}\langle\psi_\nu|\rho_p(t_0, t_1, t_2, t_3)|\psi_\nu\rangle}, \tag{2.21}$$

where the quantity $\mathcal{N}\langle\psi_\nu|\rho_p(t_0, t_1, t_2, t_3)|\psi_\nu\rangle$ represents the expected number of counts for a projection of our trial density matrix ρ_p onto the analysis state $|\psi_\nu\rangle$. Note that the coincidence counts are subtracted from $\mathcal{N}\langle\psi_\nu|\rho_p(t_0, t_1, t_2, t_3)|\psi_\nu\rangle$, so that the likelihood function must be *minimized* to obtain the set of $t_i^{(opt)}$, and therefore the state that best retrodicts the actual measurements[11].

Although this fidelity is quite good, there are several sources of error to which (at least in part) we can attribute imperfect agreement: Poisson counting fluctuations, drift in pump intensity/detector efficiency, wave plate phase uncertainty, and wave plate setting uncertainty. A numerical simulation helps put bounds on each of these errors. To get an idea of Poisson counting fluctuations, we used the measured photon counts as mean values in a Poisson distribution for each measurement setting. Then we selected a random number from each distribution to get a perturbed set of counts. With these counts, we ran a maximum likelihood routine to generate a density matrix, which was used to calculate a fidelity with the theoretical target state. This

---

[11] The minimization is performed using the MATLAB R12 function fminunc which requires an initial estimate for the t_i. For the initial estimate, starting guesses for the ρ_i are calculated from the measured counts N_0, N_1, N_2, and N_3; through (2.8), this gives a starting estimate for ρ, which, from (2.19) and (2.20), yields starting values for the t_i: $t_0 = 1 - \sqrt{a}$, $t_1 = \frac{\sqrt{2(1-r_H)}}{2}$, $t_2 = \frac{r_D}{\sqrt{2(1-r_H)}}$, and $t_3 = \frac{r_R}{\sqrt{2(1-r_H)}}$, with $a = t_1^2 + t_1^2 + t_3^2$.

process was repeated 3000 times to generate a distribution of fidelities from which the mean gives an idea of the error due to counting statistics. For the data in Fig. 2.3, a total ~150,000 counts were accumulated for each state, which gives mean fidelity errors of ~0.0001 to ~0.001 (the larger statistical error values come from the pure state $|H\rangle$). The statistical uncertainty depends on the state, which we illustrate below by taking repeated measurements of states with different purity.

To evaluate the effect of drift errors, two simulations were carried out, one assuming a constant drift (i.e., always increasing or decreasing) of 1% during the entire course of the measurement, the other a drift of 0.25% that could be positive or negative for each measurement (randomly chosen). A randomly selected set of "simulated measurement probabilities" gives an ideal no-drift state[12]. Then drift is randomly added or subtracted to the each simulated measurement probability. In this way, the drifted and undrifted probabilities yield two density matrices after the application of a maximum likelihood technique on each set of counts. The fidelity of the two density matrices were calculated. This process was repeated 10000 times[13] and could account for a reduction in the fidelity of 0.0002 and 0.00001 for the constant drift and random drift calculations, respectively.

To get an idea of the reduction of fidelity due to wave-plate setting uncertainty, we calculated the expected density matrix given a random set of three wave plate angles, i.e., all three independent parameters to give an arbitrary state. Then, as we believe we could set the wave plates to within 0.1°, we set up a 0-mean normal distribution with a 0.1° standard deviation. For each wave plate setting, we added a random number from the Poisson distribution, and calculated a perturbed density matrix. A fidelity was calculated from the two density matrices. The process is repeated 10000 times and, on average, accounts for a loss of 0.00002 in the fidelity. A similar calculation is done to calculate the loss in fidelity due to wave plate phase uncertainty[14]. This would account for a typical loss of fidelity of 0.0001. Adding the wave plate setting, statistical and larger of the two drift errors, and the phase error in quadrature accounts for ~0.0002 to 0.001 loss of fidelity; thus, the drift and the statistical uncertainty dominate depending on the state. There remains some as

---

[12] These probabilities were uniformly distributed between 0 and 1 so we could use a variety of different input states.

[13] Thus, 10000 randomly selected states are subjected to the drift error from which 10000 fidelities are calculated. The average of these 10000 fidelities gives us an idea of the typical fidelity loss for such errors.

[14] We used the typical manufacturer specifications of ±1.8° for HWPs and ±0.9° for the QWP for the normal distribution standard deviations. Note that this gives one an idea of what a random wave-plate phase error has on the fidelity. In reality, we use the same wave plates and the phase is fixed, which would give a systematic error. In future experiments, we eliminate (or at least substantially mitigate) this systematic error by measuring the specific phase retardance for each wavelength, and use that measurement to calculate the best wave-plate setting.

yet unaccounted for systematic error.

The question of how many distinct states can be reliably *produced* is limited by how many may be reliably experimentally *distinguished*[15]. To determine the number of accessible distinguishable states in our system, several states in different parts of the Poincaré sphere (with approximate $|\vec{r}|$ values of 0, 0.25, 0.5, 0.75, and 1) were created and measured 10 times each[16]. We measured for 10 minutes per tomography yielding ∼300,000 counts per state reconstruction. For each set of measurements the average state vector $\vec{r}$ was determined. Next, the standard deviation of the ten trials was determined for three directions: $\hat{\vec{r}}_i$, and two directions transverse to $\vec{r}$. Assuming a Gaussian distribution along these directions, we calculate that an ellipsoid with semi-axes equal to 1.69 times these standard deviations will account for over 95% of the events. These uncertainty ellipses are mainly due to count fluctuations from laser and detector efficiency drift, as well as intrinsic Poisson counting statistics. One unexpected result of our measurements was that the thickness of the ellipsoid (i.e., the length of the minor axis along the direction of $\hat{\vec{r}}$) depended on the radial coordinate $|\vec{r}|$, and varied from a minimum value of 0.0021 for $|\vec{r}| = 1$, to a maximum value of 0.0062 for $|\vec{r}| = 0.25$ (see Fig. 2.4(a)). Taking into account the varying size of the uncertainty patches, and assuming an approximate close packing of the entire Poincaré sphere volume, we estimate that we can reliably distinguish over three million states.

Numerical simulations support this observation (see Fig. 2.4(b)). In our numerical simulation, we calculated the expected counts one would measure for a state $|H\rangle$ that had been uniformly depolarized by adding the single-qubit mixed state $\frac{1}{2}\mathbb{1}$:

$$\rho(r) = r|H\rangle\langle H| + \frac{1-r}{2}\mathbb{1}. \tag{2.22}$$

These expected counts (we have assumed 100,000 counts for a complete basis measurement) are then used as the means of Poisson distributions from which a set of perturbed counts is randomly generated. A maximum likelihood calculation on the perturbed counts gives a valid density matrix

---

[15] When specifying a produced quantum state, it is an interesting question whether one should give an error ball (e.g., a patch on the surface of the sphere for a pure state), or simply average over this ball to yield a slightly mixed state. The former approach accounts for the fact that the error ball could shrink if more data were taken. The latter method acknowledges that the density matrix already encodes the totality of our knowledge, based on our measurements on identically prepared members of an ensemble. Here we adopt the error ball approach.

[16] The essential elements of this part of the experiment and analysis were done by Evan Jeffrey, who wrote the data acquisition and analysis routines.

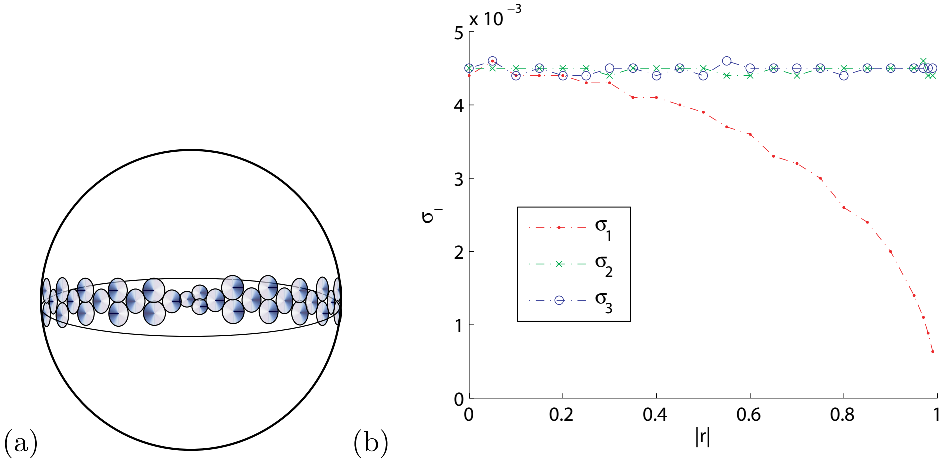

(a) (b)

Figure 2.4: (a) Filling the Poincaré sphere with experimentally determined uncertainty "patches". These arise primarily due to counting fluctuations, either from the Poisson statistical uncertainties in photon counting, or from slight drifts ($< 0.5\%$) in the laser power or detector efficiencies. The measured uncertainty patches are approximately ellipsoids (pancakes) as shown above; for clarity their dimensions are shown scaled up by a factor of 5. Note that the thickness of the pancakes depends somewhat on the mixture of the state, indicating that some regions of the Poincaré sphere are more sensitive to counting statistics. The size of uncertainty patches implies that we are able to distinguish more than three million unique single-qubit states, assuming ∼10 minutes data collection time per state, i.e., ∼300,000 detection events). (b) Standard deviation for Poisson fluctuations of "simulated photon counts" for density matrices of variable mixedness determined by $|\vec{r}| = r_1 = r$. For our test density matrices, we add $\frac{1}{2}\mathbb{1}$ to the state $|H\rangle$, thus $r_2 = r_3 = 0$.

from which we calculate the three Poincaré components r_i, and their standard deviations. In this way we generated 3000 perturbed density matrices for each value of $|\vec{r}|$. In our simulation, σ_2 and σ_3 are constant at ~ 0.0045 whereas σ_1 is the same as σ_2 and σ_3 only when $|\vec{r}| = 0$, and drops as r_1 (and therfore, for this particular state, the purity) increases. Our simulation does not account for drift, which could explain the slight discrepancies between it and our measurements.

Chapter 3

Two-qubit creation and characterization

According to Schrödinger, “entanglement is the characteristic trait of quantum mechanics.” But for an idea that has been around since the first half of the twentieth century, entanglement, even for the simplest example of a pair of entangled two-level entangled systems, still yields new and interesting physics. Although entangled states have been demonstrated in a variety of systems [31, 32, 33, 34, 17, 35], here we will restrict our attention to two-qubit entangled states encoded in photon polarization.

In this chapter, we first discuss the critical resource for two-qubit state creation (and for remote state preparation in chapter 6) – the creation of polarization entangled photon pairs. Then, we briefly describe how we can characterize two-qubit states using state tomography in an extension of the single-qubit tomography discussion of the previous chapter.

3.1 Polarization-entangled two-qubit states

We create pairs of photons using spontaneous parametric downconversion (SPDC). Recall from Section 2.2 that a pump photon with frequency ω_p interacts with a nonlinear crystal to generate daughter photons of frequency ω_1 and ω_2 such that energy is conserved. Similarly, momentum inside the crystal is conserved via the phase matching condition. Specifically we use type-I phase matching, where the pump has extraordinary polarization whereas the photons in the downconversion pair have ordinary polarization. In this case, a nonlinear crystal (e.g., beta-barium borate [BBO]) is pumped with polarization in the plane of the crystal axis. This has a small probability to generate

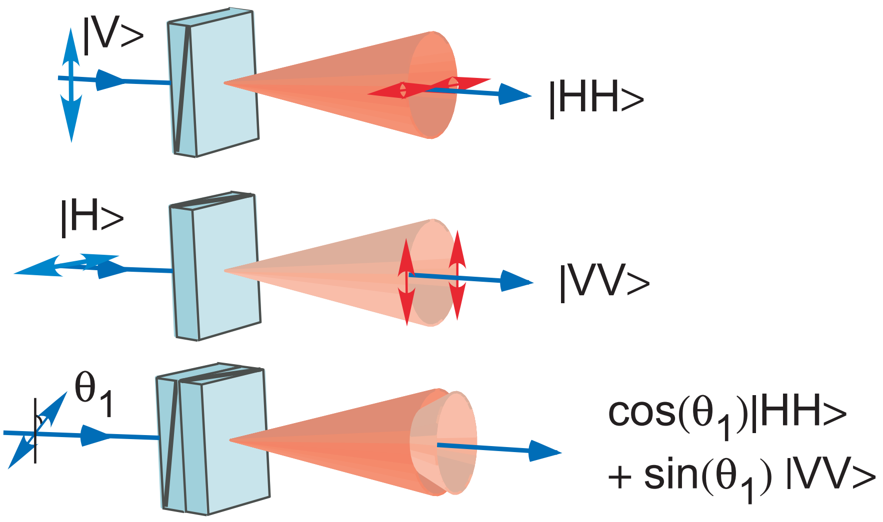

Figure 3.1: Two-crystal scheme to create polarization entanglement. Top: vertically polarized light pumping a crystal with its optic axis in the vertical plane generates pairs of horizontally polarized photons. Middle: similarly, a 90° rotation of the entire scheme produces pairs of horizontally polarized photons. Bottom: by orienting the optic axes of the crystals to be in perpendicular planes, and by pumping the crystals with light polarized at angle θ_1 (with respect to vertical), we produce a variable superposition of pairs of horizontally and vertically polarized photons.

daughter photons with polarization orthogonal to that of the pump. Thus, vertically polarized light pumping a crystal with its optic axis in the vertical plane generates pairs of horizontally polarized photons. If one instead rotates the system by 90° about the pump direction, horizontally polarized light pumping a crystal with its optic axis in the horizontal plane generates pairs of vertically polarized photons.

As in Fig. 3.1, by orienting two thin crystals such that their optic axes are in perpendicular planes, and pumping with diagonally polarized light, one obtains a coherent superposition of photon pairs created in either the first crystal or the second crystal. To create high-quality entanglement, the crystals must be thin enough such that one cannot, in principle, tell in which crystal the pair was born (short of making a polarization measurement). For a continuous-wave laser pump, we typically work in the regime where the coherence length of the pump is 100-1000 times the thickness of each nonlinear crystal; the diameter of the pump beam ($\sim$3 mm) is also much larger than the relative transverse shift of the cones ($\sim d \sin\theta$ for a crystal thickness d and a cone opening angle θ see Fig. 3.2).

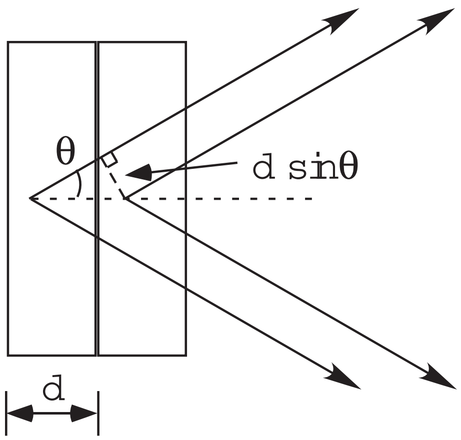

Figure 3.2: Two-crystal scheme transverse shift.

More generally, when pumping with light polarized at angle θ_1 with respect to vertical, we generate an arbitrary superposition [36, 37]:

$$\cos\theta_1|HH\rangle + e^{i\alpha}\sin\theta_1|VV\rangle, \tag{3.1}$$

where the position of the polarization labels the spatial mode of the emitted photon. For example, the state $|HH\rangle$ corresponds to a horizontally polarized photon in each of two downconversion modes. Typically, we select phase-matching conditions so that photon pairs are emitted into a cone with a 3° half-opening angle with respect to the pump at the center of the cone. Thus, one photon would be emitted into a +3° mode while the twin is emitted into -3°[1]. The phase between the polarization states of photon pairs born in different crystals is given by α. This phase is generally not zero due to the birefringence of the crystals. We will discuss the manipulation of this phase later. If we have adjusted this phase to be zero, and pump with 45° polarized light, then we will generate the Bell state [16]

$$|\Phi^+\rangle = (|HH\rangle + |VV\rangle)/\sqrt{2}. \tag{3.2}$$

By implementing unitary transformations with wave plates, we can produce the remaining Bell

---

[1] More precisely, the photons have amplitudes to be emitted into any pair of diametrically opposed directions on the emission cone.

states given by the following:

$$\begin{aligned} |\Phi^-\rangle &= (|HH\rangle - |VV\rangle)/\sqrt{2}, \qquad (3.3)\\ |\Psi^+\rangle &= (|HV\rangle + |VH\rangle)/\sqrt{2}, \text{ and} \qquad (3.4)\\ |\Psi^-\rangle &= (|HV\rangle - |VH\rangle)/\sqrt{2}. \qquad (3.5) \end{aligned}$$

Finally, note that by changing the pump polarization, we can create photon pairs with an arbitrary amount of entanglement, from the maximally entangled $|\Phi^+\rangle$ to unentangled (product state) photon pairs, e.g., $|HH\rangle$ when $\theta_1 = 0$.

3.2 Tomography

Just as one cannot determine the unknown polarization state[2] of a *single* photon with a single measurement, it is not surprising that one also cannot determine the unknown two-photon (i.e., two-qubit) polarization state with a single measurement. Instead, a large ensemble of photon pairs prepared in an identical manner must be projected into different polarization basis states. A general two-qubit state has 15 free parameters, requiring at least 15 independent measurements to characterize it. Such a state can be represented with an eigenbasis of four orthonormal states, corresponding to four measurement probabilities, which are the diagonal elements in a density matrix. Enforcing normalization for these four probabilities gives rise to three free parameters. The 12 additional free parameters are from the amplitude and phase of each off-diagonal element[3]. In practice, we measure counting rates (not probabilities), which require an additional measurement for normalization. Thus, we must make at least 16 measurements to fully characterize a two-qubit state.

The polarization analysis is carried out setting the quarter- and half-wave plates shown in the tomography system box of Fig. 3.3, followed by vertically oriented polarizers. There are (infinitely) many choices as to the particular measurements that can be made, but we choose the analysis states: $\langle HH|$, $\langle HV|$, $\langle VH|$, $\langle VV|$, $\langle HD|$, $\langle HR|$, $\langle VD|$, $\langle VR|$, $\langle DH|$, $\langle DV|$, $\langle DD|$, $\langle DR|$, $\langle RH|$,

---

[2] Here and throughout, we use "state" to refer to not only pure states but also impure density matrices.

[3] As the density matrix is Hermitian, knowledge of the upper diagonal determines the lower diagonal and vice versa.

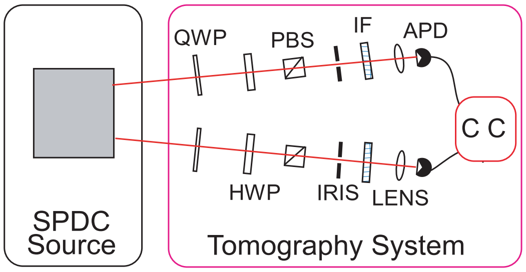

Figure 3.3: Two-qubit tomography setup. Photon pairs from a SPDC source are measured with the tomography system using a quarter-wave plate (QWP), half-wave plate (HWP), and a polarizer in each arm to analyze in arbitrary polarization bases; the transmitted photons are counted in coincidence (CC) via avalanche photodiodes (APD).

$\langle RV|$, $\langle RD|$, and $\langle RR|$, corresponding to N_0, N_1, N_2, etc. photon coincidence counts in some fixed measurement time interval (typically 100 s), in analogue with the single-photon tomography discussed in the previous chapter. Notice that the first four measurements give the incident photon flux because the measurements correspond to analysis states that span the basis, thus, the sum of measurements $\mathcal{N} \equiv \sum_{i=0}^{4} N_i$ can be used to normalize the other counting rates to give measurement probabilities. As the phase retardances of the wave plates are usually not exactly quarter- or half-waves, we calibrated each wave plate. We used these measurements to numerically determine the wave plate settings that most closely project into the states given above (see Table 3.1)[4]. Instead of using the Pauli matrices to generate the density matrix as in the single-qubit case, we use the tensor product of them, i.e., $\Gamma_i \equiv \sigma_j \otimes \sigma_k$, where the indices j and k run from 0 to 3 to give a generator Γ_i corresponding to each of the sixteen N_i, yielding the density matrix

$$\rho = \sum_{i=1}^{16} \frac{N_i}{\mathcal{N}} \Gamma_i. \tag{3.6}$$

As this state reconstruction is based on photon counting, statistical fluctuations or pump laser and detection efficiency drift often yield an unphysical result, such as a ρ with one or more negative eigenvalues; therefore as in the single qubit tomography case, we again employ a maximum

---

[4] In practical tomography, one can project into any set of states that span the basis space, as long as one knows the states. We used the settings and wave plate phase retardances to calculate the states that photons were actually projected into for making the state reconstruction. In this way, even if one could not get close to the analysis states listed above, that would be taken into account in the tomographic measurement. However, we optimized the QWP/HWP combinations to get the best projections into the analysis states listed above, so, to a very high degree, we *did* project into the analysis states listed. We estimate that the fidelity of the least accurate single-qubit state projection with its target was better than 0.999.

Wave plate (Measured phase)	Arm 1 QWP 89.90°	Arm 1 HWP 182.62°	Arm 2 QWP 86.73°	Arm 2 HWP 175.40°
State				
$\langle H\vert$	-1.30°	44.35°	2.30°	46.08°
$\langle V\vert$	0.00°	90.00°	0.00°	90.00°
$\langle D\vert$	44.06°	67.02°	-46.67°	66.69°
$\langle R\vert$	-42.81°	1.09°	-90.29°	-22.67°

Table 3.1: Two-qubit tomography optimized settings and measured wave plate phases. Notice that the $\langle V|$ measurement settings appear "perfect." Because we use vertically oriented polarizers, we set the wave plates to *not* change the state. Thus, regardless of the wave plate phases, we set the wave plates' optic axes relative to the polarizer. Also note that because there are many solutions to the numerical optimization, sometimes the wave plate settings can look different for Arm 1 and Arm 2 (as is the case for $\langle R|$).

likelihood technique to estimate the physical density matrix that would most likely produce the measured data [29]. Details of the maximum likelihood procedure for two-qubit states can be found in [29, 38].

3.3 State measures

As the successful outcome of many quantum information protocols requires entanglement and is often hindered by nonzero entropy, it is natural to want to quantify these properties. A common measure to quantify the entanglement is the tangle, $T(\rho)$, defined by [39]:

$$T(\rho) \equiv [\max\{0,\ \lambda_1 - \lambda_2 - \lambda_3 - \lambda_4\}]^2, \tag{3.7}$$

i.e., the concurrence squared. Here λ_i are the square roots of the eigenvalues of $\rho(\sigma_2 \otimes \sigma_2)\rho^*(\sigma_2 \otimes \sigma_2)$, in non-increasing order by magnitude, with σ_2 defined in equation 2.9. The tangle ranges from 0, for an unentangled state (e.g., the pure product state $|HH\rangle$), to 1, for maximally entangled states such as $|\Phi^+\rangle$. We characterize the state mixture using the linear entropy, $S_L(\rho)$, [40]

$$S_L(\rho) = \frac{4}{3}[1 - \mathrm{Tr}(\rho^2)], \tag{3.8}$$

where the trace of the square of the density matrix is the "purity" of the state. The linear entropy ranges from 0 for pure states (such as $|HH\rangle$ and $|\Phi^+\rangle$) to 1 for the completely mixed state (i.e., unpolarized photons). We choose to use the linear entropy for its simple form (as opposed to the more common von Neumann entropy) and because it was used to derive the Maximally entangled mixed states we discuss in the next chapter[5].

---

[5] For a comparison of the two-qubit von Neumann and linear entropies see reference [41].

Chapter 4

Maximally entangled mixed states and entanglement concentration

Previously, several classes of two-qubit entangled states have been realized using optical qubits; maximally entangled and nonmaximally entangled pure states [32, 36, 37], nonmaximally entangled mixed states [42], and the special case of Werner states [43] (incoherent combinations[1] of a completely mixed state and a maximally entangled pure state). For some time it was believed that Werner states possess the most entanglement for a given level of mixedness. However, a class of states that are more entangled than Werner states of the same purity was discovered [44, 45, 46]. These maximally entangled mixed states (MEMS) possess the *maximal* amount of entanglement (tangle or entanglement of formation) for a given degree of mixedness (linear entropy)[2].

In this chapter, we experimentally explore the region above the Werner-state line on the linear entropy-tangle plane by creating MEMS. Although the creation of MEMS is intrinsically fascinating considering that it is a heretofore unobserved type of entangled state, MEMS also facilitate the study of a class of quantum information protocols that can transform ensembles of weakly entangled mixed states into maximally entangled pure states. Such entanglement "concentration" techniques may well turn out to be critical, given that the success of many quantum information protocols (e.g., teleportation) assumes pure maximally entangled states as inputs. Thus, we also describe a partial-polarizer filtration/concentration technique that simultaneously increases both purity and entanglement, at the cost of decreasing the ensemble size of initial photon pairs. Al-

---

[1] An example of a Werner state is given by $(1-\lambda)|\Phi^+\rangle\langle\Phi^+| + \frac{\lambda}{4}\mathbb{1}$, where $|\Phi^+\rangle$ is a maximally entangled state defined in equation 3.2 and $\frac{1}{4}\mathbb{1}$ is the two-qubit mixed state, i.e., the identity operator scaled so that its trace is one.

[2] Note that for certain entanglement and mixedness parameterizations, the Werner states *are* the MEMS [41].

though the implementation requires initial state knowledge, we show that MEMS exist for which this "Procrustean" filtering technique [47, 48, 49] is much more efficient than other recent entanglement concentration schemes [50, 51], even after they are optimized to work on MEMS. The work in this chapter was published in [52, 53].

4.0.1 MEMS: theoretical considerations

The exact form of the MEMS density matrix depends on the measures used to determine the maximal entanglement for a given mixedness [41]. Following Munro et al., we consider the MEMS parameterized by the linear entropy and the tangle [44]. In this parameterization, the MEMS density matrices exist in two subclasses [44], $\rho_{MEMS\ I}$ and $\rho_{MEMS\ II}$,which have two and three nonzero eigenvalues, respectively:

$$\rho_{MEMS\ I} = \begin{pmatrix} \frac{r}{2} & 0 & 0 & \frac{r}{2} \\ 0 & 1-r & 0 & 0 \\ 0 & 0 & 0 & 0 \\ \frac{r}{2} & 0 & 0 & \frac{r}{2} \end{pmatrix}, \quad \frac{2}{3} \le r \le 1, \tag{4.1}$$

$$\rho_{MEMS\ II} = \begin{pmatrix} \frac{1}{3} & 0 & 0 & \frac{r}{2} \\ 0 & \frac{1}{3} & 0 & 0 \\ 0 & 0 & 0 & 0 \\ \frac{r}{2} & 0 & 0 & \frac{1}{3} \end{pmatrix}, \quad 0 \le r \le \frac{2}{3}, \tag{4.2}$$

where r is the concurrence, i.e., the square root of the tangle defined in equation 3.7.

4.0.2 MEMS: experimental creation

Our creation of MEMS involves three steps: creating an initial pure state of arbitrary entanglement, applying local unitary transformations, and inducing decoherence. First, frequency degenerate 702-nm photons are created by pumping thin nonlinear β-Barium Borate (BBO) crystals with a 351-nm Ar-ion laser. As described in the previous chapter, polarization entanglement is realized by pumping two such crystals, oriented so that their optic axes are in perpendicular planes. We create the variable entanglement superposition state of equation 3.1 by controlling the pump polarization with a half-wave plate (HWP_1 in Fig. 4.1) set to $\theta_1/2$.

To create the MEMS I, we start by setting the initial degree of entanglement to that of the target MEMS[3]. The phase α is set to zero by tipping a QWP (labeled "ϕ-plate" in Fig. 4.1) about its vertically oriented optic axis. Next, a maximum likelihood tomography [37, 29] of this initial entangled state is taken and, based on a numerical search, is used to determine the appropriate settings of HWP_2 and HWP_3 in Fig. 4.1. In particular, these wave plates set the diagonal elements of the density matrix to the target values for the desired MEMS[4]. The initial tomography must be precise, because the wave plate settings are critically dependent on the initial state, as well as on the precise birefringent retardation of the wave plates themselves. After the wave plates, the state passes through decoherers, which lower specific off-diagonal elements in the density matrix, yielding the final state (see Appendix A). In our scheme, each decoherer is a thick birefringent element ($\sim$1 cm quartz, with optic axis horizontal[5]) chosen to have a polarization-dependent optical path length difference ($\sim 140\lambda$)[6] greater than the downconverted photons' coherence length ($L_c \equiv \lambda^2/\Delta\lambda \cong 70\lambda$, determined by a 10-nm FWHM interference filter placed before each detector), but much less than the coherence length of the pump [54].

Analogous to the decoherer in the single-qubit case, here the decoherer in each arm couples the polarization with the relative arrival times of the photons[7]. While two horizontal ($|HH\rangle$) or two vertical ($|VV\rangle$) photons will be detected at the same time, the state $|VH\rangle$ will in principle be detected first in arm #1 and then in arm #2, and vice versa for the state $|HV\rangle$ (the decoherer slows horizontally polarized photons relative to vertically polarized ones). Tracing over timing

---

[3] In the ideal case, $\theta_1/2 = \frac{1}{4}\arcsin r$

[4] By calculating the two-photon state operator of HWP_2 and HWP_3, and measuring the state on which they operate, we can numerically optimize the wave-plate settings to give the best MEMS precursor. The best results are obtained when using wave plates that have a phase retardance of precisely one half-wave. Thus, we used our best half-wave plates, with phases closest to the ideal 180°, for state creation.

[5] Whether the fast axis or the slow axis of a birefringent decoherer is horizontal is irrelevant, as long as all decoherers are set the same. Therefore, we assume, for the purpose of discussion, that the slow axis is horizontal. Quartz is positive uniaxial and thus, the optic axis has a higher index of refraction than the other axis (at 90° from the optic axis and the propagation direction).

[6] The optical path length difference of the decoherers is generally not exactly an integer multiple of λ, causing an extra phase on the off-diagonal elements. This residual phase is set to zero by slightly tipping one of the decoherers about its vertical axis.

[7] As demonstrated in [55], one could instead use the *spatial* degree of freedom to induce decoherence; however, the states are then not suitable, e.g., for use in fiber optic systems, or where interference methods are needed.

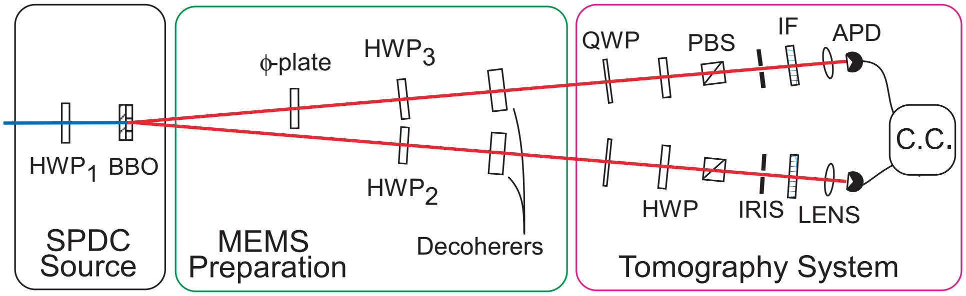

Figure 4.1: Experimental arrangement to create MEMS. A half-wave plate (HWP$_1$) sets the initial entanglement of the pure state. The ϕ-plate sets the relative phase between $|HH\rangle$ and $|VV\rangle$ in the initial state. HWP$_2$ and HWP$_3$ rotate the state into the active bases of the decoherers to adjust the amount of entropy. The tomography system uses a quarter-wave plate (QWP), HWP, and a polarizer in each arm to analyze in arbitrary polarization bases; the transmitted photons are counted in coincidence via avalanche photodiodes.

information during state analysis then erases coherence between any distinguishable terms of the state (i.e., only the coherence term between $|HH\rangle$ and $|VV\rangle$ remains). A sample tomography of a MEMS I labeled (A) is shown in Fig. 4.2(a).

MEMS II are created by first producing the MEMS I at the MEMS I/II boundary, i.e., the state with $r = \frac{2}{3}$. In order to travel along the MEMS II curve, the optical path length difference in *one* arm must be varied from 140λ. This couples different relative timings to the $|HH\rangle$ and $|VV\rangle$ states (see AppendixA), reducing the coherence between them. For instance, to make the MEMS II, labeled (B) in Fig. 4.2(a), 140λ decoherence was used in one arm, 90λ in the other. Fig. 4.2(a) indicates very good agreement between theory and experiment, with fidelities of $\sim$99%.

The states (A) and (B) are shown in the S_L-T plane in Fig. 4.2(b), along with other MEMS that we created. The states do not hit their S_L-T targets (shown as stars in the figure) within errors[8], even though the states have very high fidelities ($\gtrsim$ 99%) with their respective targets. To explore the discrepancy, for each target we numerically generated 5000 density matrices that had at least 0.99 fidelity with the target density matrix[9]. The S_L and T of the numerically

---

[8] We used the methods outlined in reference [29] to calculate the error bars shown in Fig. 4.2, which include statistical counting fluctuations and wave plate setting uncertainties of ±1°. More recently, we have found that this method of calculating the errors is an over-estimate compared to the spread we see in taking the measurement several times. However, as the difference between the errors determined these two ways are very small, compared to the 0.99 fidelity regions, our conclusions are unchanged.

[9] In more detail, we project the ideal target state into 16 basis vectors, such as $\langle 00|$, $\langle 11|$, $\langle (0+i1)0|$, etc., to obtain a list of probabilities of given "measurement" outcomes. These probabilities are then multiplied by a constant number (1000 for this Chapter and 500 for the simulations in the next chapter, where we chose a lower number to get wider fluctuations), thus simulating an expected average number of counts in a total basis measurement, e.g., what

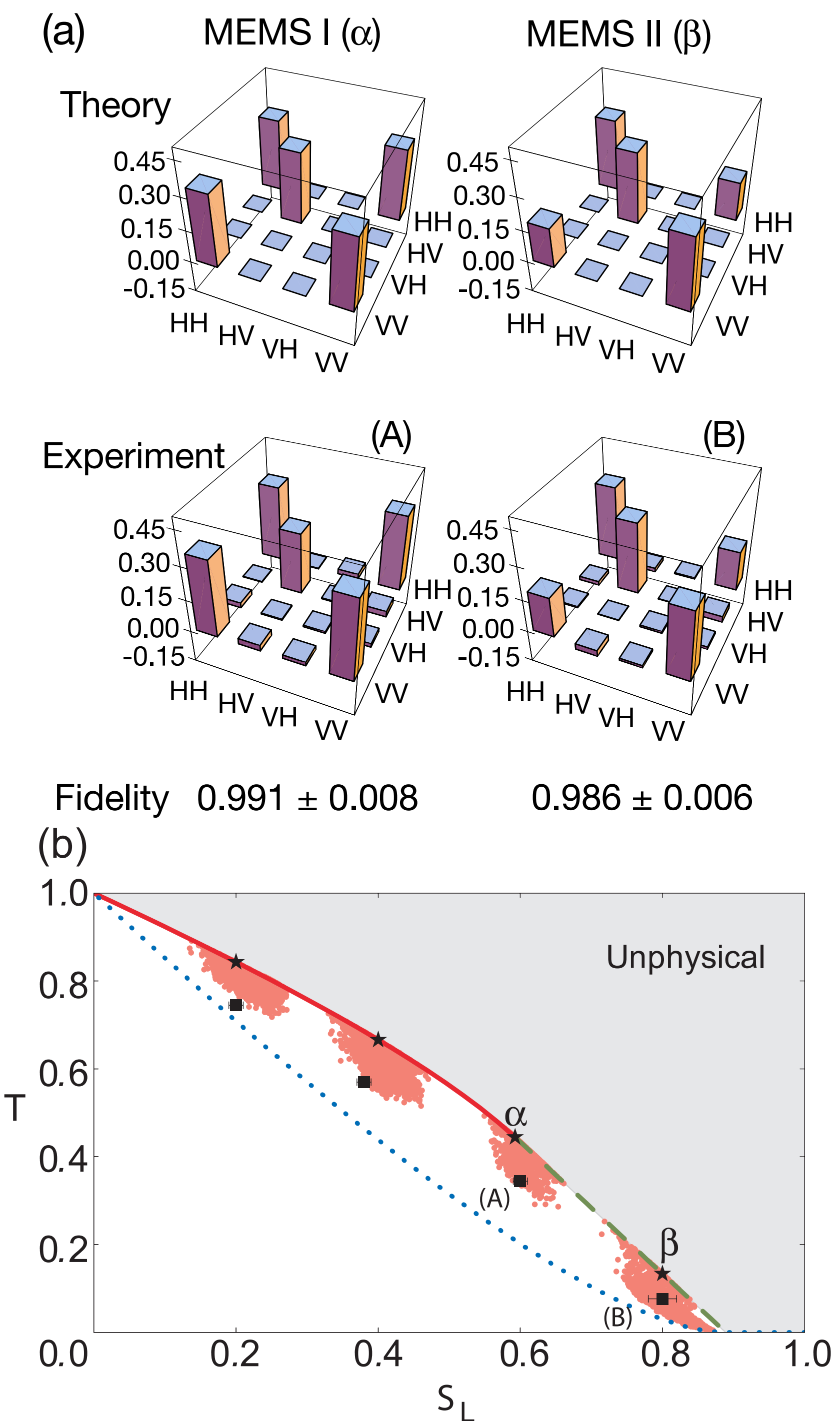

Figure 4.2: MEMS data. (a) Density matrix plots of the real components of a MEMS I ($r = \frac{2}{3}$) and a MEMS II ($r = 0.3651$). The imaginary components are negligible (on average less than 0.02) and not shown. (b) Linear entropy-tangle plane. Shown are theoretical curves for MEMS I (solid line), MEMS II (dashed line), and Werner states (dotted line). Four target MEMS are indicated by stars; experimental realizations are shown as squares with error bars. The shaded patches around each target state show the tangle (T) and linear entropy (S_L) for 5000 numerically generated density matrices that have at least 0.99 fidelity [28] with the target state. T=0 (1) corresponds to a product (maximally entangled) state. S_L=0 (1) corresponds to a pure (completely mixed) state.

generated states are plotted in Fig. 4.2(b) as shaded regions surrounding the targets. The fact that these regions are rather large (and overlap with our measured MEMS) explains our results, but is surprising nonetheless. The unexpectedly large size of these patches arises from the great difference in sensitivity between the state measures of fidelity, tangle and entropy; we will discuss this phenomenon in detail in the next chapter.

4.1 Entanglement concentration

Although our initial goal was to produce states of maximal tangle for a given linear entropy, maximally entangled *pure* states are generally more useful for quantum information protocols. However, in some cases, weakly entangled mixed states may be the only available resource. It is therefore important to study ways to simultaneously decrease the entropy and increase the entanglement of an ensemble of photon pairs (necessarily at the cost of reducing the size of the ensemble). Recently, several such entanglement concentration[10] experiments have been reported, relying on two-photon interference effects [50, 51]. An interesting characteristic of MEMS is that they can be readily concentrated by a "Procrustean" method of local filtering [47, 48][11]. Procrustean concentration requires knowledge of the quantum state. This knowledge enables the selection of a filter to reject part of the state of each system, leaving each remaining photon pair in a more entangled, lower entropy state.

4.1.1 Experimental entanglement concentration

To concentrate entanglement, we first modify the MEMS using HWP_4 at 45°, as shown in Fig. 4.3, to exchange $|H\rangle \leftrightarrow |V\rangle$ in the first arm, changing the non-zero diagonal elements of the MEMS

---

one would expect to observe when projecting into $\langle 00|$, $\langle 01|$, $\langle 10|$, and $\langle 11|$. Next, each of these ideal counts (plus one, to avoid zero distributions) is used as the mean of a Poisson distribution, from which a random number is generated. These "measurement" values are then processed using a maximum likelihood technique to give a physically valid perturbed density matrix [29, 56]. If the fidelity between the perturbed density matrix and the target state is greater than 0.99, the tangle and linear entropy are calculated and plotted in Fig. 4.2(b).

[10] Here we adopt the nomenclature suggested by Thew and Munro, where "concentration" refers to simultaneously increasing entanglement while decreasing entropy [49]. Additionally, Thew and Munro define the constant entropy process where entanglement increases as "distillation" and "purification" describes the process where entropy is reduced while entanglement remains unchanged.

[11] Procrustes was a sadistic character in Greek mythology. He offered a bed to guests but insisted that a guest fit exactly in the bed (which Procrustes could secretly adjust the size of). If one did not fit in the bed, they were either stretched or cut down to fit.

density matrix to $|HV\rangle\langle HV|$, $|VH\rangle\langle VH|$, and $|VV\rangle\langle VV|$, yielding[12]

$$\rho_{MEMS\ I_{|\phi^+\rangle}} \quad = \quad \begin{pmatrix} 0 & 0 & 0 & 0 \\ 0 & \frac{r}{2} & \frac{r}{2} & 0 \\ 0 & \frac{r}{2} & \frac{r}{2} & 0 \\ 0 & 0 & 0 & 1-r \end{pmatrix}, \quad \frac{2}{3} \leq r \leq 1, \tag{4.3}$$

$$\rho_{MEMS\ II_{|\phi^+\rangle}} \quad = \quad \begin{pmatrix} 0 & 0 & 0 & 0 \\ 0 & \frac{1}{3} & \frac{r}{2} & 0 \\ 0 & \frac{r}{2} & \frac{1}{3} & 0 \\ 0 & 0 & 0 & \frac{1}{3} \end{pmatrix}, \qquad 0 \leq r \leq \frac{2}{3}. \tag{4.4}$$

By reducing the $|VV\rangle\langle VV|$ element of the rotated MEMS (in the lower left corner of equations 4.3 and 4.4), the outcome will be driven toward the following maximally entangled pure state (this behavior is theoretically quantified below):

$$|\Phi^+\rangle\langle\Phi^+| \equiv \begin{pmatrix} 0 & 0 & 0 & 0 \\ 0 & \frac{1}{2} & \frac{1}{2} & 0 \\ 0 & \frac{1}{2} & \frac{1}{2} & 0 \\ 0 & 0 & 0 & 0 \end{pmatrix}. \tag{4.5}$$

We achieve this by inserting glass pieces oriented at Brewster's angle, as indicated in the dotted box in Fig. 4.3. Each piece consists of four ~1-mm thick microscope slides, sandwiched together

---

[12] We apply this transformation so that the $|VV\rangle\langle VV|$ element has no coherence with the other diagonal elements. As we shall soon see, this is a convenient choice, as it allows us to set our concentrating elements in the same bases in both experimental arms.

with index matching fluid[13]. Equal numbers of pieces are used in both arms[14]; they are oriented to nearly perfectly transmit horizontally polarized photons (the transmission probability for one glass sandwich was $T_H = 0.990 \pm 0.006$) while partially reflecting vertically polarized photons ($T_V = 0.740 \pm 0.002$)[15].

To see concretely the effect of the partial polarizers, consider the following arbitrary density matrix

$$\rho \equiv \begin{pmatrix} r_{11} & r_{12} & r_{13} & r_{14} \\ r_{21} & r_{22} & r_{23} & r_{24} \\ r_{31} & r_{32} & r_{33} & r_{34} \\ r_{41} & r_{42} & r_{43} & r_{44} \end{pmatrix}. \tag{4.6}$$

If one concentration glass element is inserted in each arm then this matrix becomes [49]

$$\rho \equiv \frac{1}{N} \begin{pmatrix} T_H^2 r_{11} & T_H^{\frac{3}{2}} T_V^{\frac{1}{2}} r_{12} & T_H^{\frac{3}{2}} T_V^{\frac{1}{2}} r_{13} & T_H T_V r_{14} \\ T_H^{\frac{3}{2}} T_V^{\frac{1}{2}} r_{21} & T_H T_V r_{22} & T_H T_V r_{23} & T_H^{\frac{1}{2}} T_V^{\frac{3}{2}} r_{24} \\ T_H^{\frac{3}{2}} T_V^{\frac{1}{2}} r_{31} & T_H T_V r_{32} & T_H T_V r_{33} & T_H^{\frac{1}{2}} T_V^{\frac{3}{2}} r_{34} \\ T_H T_V r_{41} & T_H^{\frac{1}{2}} T_V^{\frac{3}{2}} r_{42} & T_H^{\frac{1}{2}} T_V^{\frac{3}{2}} r_{43} & T_V^2 r_{44} \end{pmatrix}, \tag{4.7}$$

where $N = T_H^2 r_{11} + T_H T_V (r_{22} + r_{33}) + T_V^2 r_{44}$ normalizes the density matrix. N additionally gives us information on the *efficiency* of the concentration, i.e., it is the factor by which the initial photon ensemble is reduced, or equivalently, the probability that a single pair will be transmitted through the partial polarizers.

---

[13] We first attempted this with microscope cover slips but found that paths arising from multiple reflections within the glass (off the front and rear of the glass as opposed to passing directly through the glass) induced additional decoherence. To get around this, we needed to use pieces of glass thick enough so that photons reflected within the glass would be deviated away from the mode of our detectors. We chose a total thickness of ∼4 mm so that multiply reflected photons would not be collected by a 2-mm iris.

[14] There were two rotation mounts that held glass sandwiches in either arm of the experiment. With the thick pieces of glass, we had to orient the glass in compensating pairs (i.e., one stage held the glass at Brewster's angle and the other held the glass at 180° from Brewster angle) to avoid deflections of transmitted photons. Each rotation stage had four spring clip filter holders (e.g., Thorlabs FH2) mounted on it. The glass slips were held at slightly different orientations, so that the total transmission through the glass can vary a small amount. This systematic error could be improved by using an individual rotation stage for each glass sandwich.

[15] The errors in transmission values are calculated from the measurements by assuming Poisson counting fluctuations.

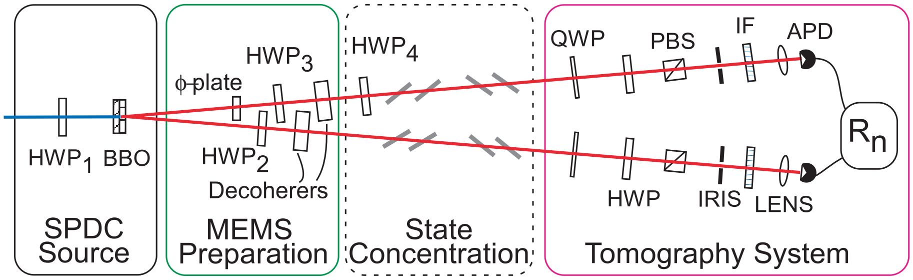

Figure 4.3: Experimental arrangement to concentrate MEMS. The dashed box contains HWP$_4$ (oriented to rotate $|H\rangle \leftrightarrow |V\rangle$ in the first arm of the experiment) and concentrating elements (a variable number of glass pieces oriented at Brewster's angle to completely transmit $|H\rangle$, but only partially transmit $|V\rangle$).

Note a characteristic difference between the two MEMS subclasses: the MEMS I have maximal coherence between the $|HV\rangle$ and $|VH\rangle$ of the parts of the state, so when the $|VV\rangle$-element is eliminated through filtering, the resulting entangled state displays maximal coherence, and therefore theoretically maximum entanglement. However, the MEMS II have less than maximum coherence between the $|HV\rangle$ and $|VH\rangle$ parts of the state, and this is not improved by filtering. Consequently, when the $|VV\rangle$-element is removed through filtering, the resulting entangled state has less than maximum coherence between $|HV\rangle$ and $|VH\rangle$, and is nonmaximally entangled.

We concentrated a variety of MEMS. Figure 4.4 shows the results for the MEMS I and II of Fig. 4.2 and an additional MEMS I (C). As the number of glass pieces is increased, the states initially become more like a pure maximally entangled state. For example, in the case of (A), the fidelity of the initial MEMS with the state $|\phi^+\rangle$ is 0.672. When the state is concentrated with eight glass sandwiches per arm, the fidelity with $|\phi^+\rangle$ is 0.90; 4.5% of the initial photon pairs survive this filtering process (the density matrices of the concentrated states are shown in Fig. 4.4 (b)). Using equation 4.7, the theoretical maximum survival probability is 6.4% when concentrating (A) with eight sandwiches per experimental arm.

While for low numbers of Brewster angle elements we observe concentration, for greater numbers we observe a reversal, indicated by stars on Fig. 4.4 (a) for various numbers of hypothetical concentrating elements. This behavior is not unexpected if one considers the density matrix of the state throughout the filtering process. Initially, the MEMS we can produce in our laboratory has the three desired large diagonal values ($|HV\rangle\langle HV|$, $|VH\rangle\langle VH|$, and $|VV\rangle\langle VV|$) and one additional

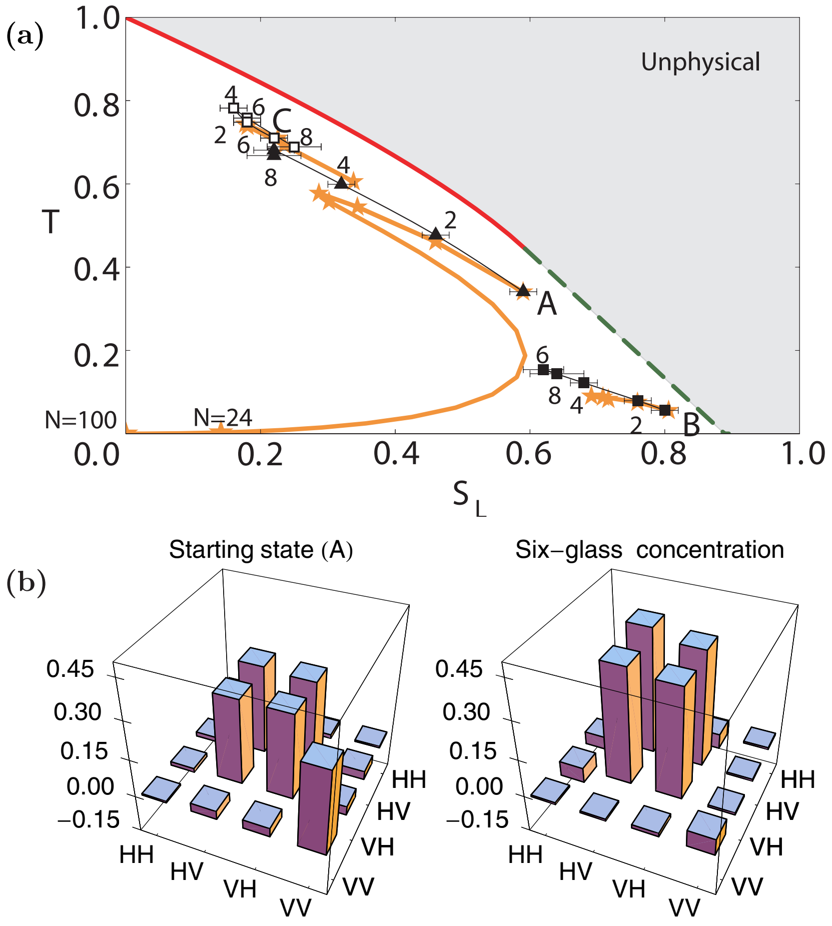

Figure 4.4: Entanglement concentration data. (a) Shown are concentrations for three initial states, A (triangles) and B (filled squares) as in Fig. 4.2, and C (open squares), along with the number of partial polarizing glass pieces in each arm. The expected concentrated state path, calculated using [49], is shown with stars. The concentrated states agree with theory for small numbers of glass pieces, but as more slips are used, the state concentrates better than expected. We believe this is because of the extreme sensitivity of the trajectory to small changes in the initial state. However, even in theory, excessive filtration will eventually produce a pure product state (shown as an extension of A's theory curve), due to small errors in the initial MEMS. (b) Real parts of the density matrix plots for the unconcentrated initial state (A), and for the same state after concentration using six glass pieces per experimental arm. The imaginary parts are negligible and not shown.

very small value ($|HH\rangle\langle HH|$), due to slight imperfections in the state. As concentration begins, all vertically polarized terms are reduced according to T_V; therefore $|VV\rangle\langle VV|$ is reduced twice as much as $|HV\rangle\langle HV|$ and $|VH\rangle\langle VH|$. Since horizontal transmission through the partial polarizers is nearly unity, the reduction of the $|HH\rangle\langle HH|$ term is negligible. As the $|VV\rangle\langle VV|$ element is reduced, the state initially becomes more entangled and less mixed. Eventually, however, the $|VV\rangle\langle VV|$ value will become equal to that of $|HH\rangle\langle HH|$, an example of a Werner state. At this point the theoretical prediction for the state starts to become *less* entangled and *more* mixed. This entanglement *un*concentration continues until the $|HH\rangle\langle HH|$ value is the same as $|HV\rangle\langle HV|$ and $|VH\rangle\langle VH|$, after which further concentration eliminates all diagonal values that have vertical polarization terms. Consequently, extreme concentration will produce the pure product state $|HH\rangle$, as illustrated for the $N = 100$ concentrating-element case in Fig. 4.4 (a).

Our states tended to concentrate slightly better than the theoretical predictions. We attribute this to the extreme sensitivity of the theoretical concentration "trajectory" to the precise initial state. To study this further, we performed a theoretical calculation using a depolarized MEMS, i.e., we added uniform noise in the same way a maximally entangled state is transformed into a Werner state. This calculation showed that small amounts of noise added to an initial state ($\rho_{MEMSI}(r = \frac{2}{3})$) can greatly change how well it may be concentrated (see Fig. 4.5). We see that noisy states (even though they have high fidelities with the perfect MEMS) can vary greatly in their trajectories on the entropy-tangle plane, and also in their final concentrated forms.

4.1.2 Theoretical concentration comparison

We now compare the theoretical efficiency of our local filtering scheme with the interference-based concentration proposal of Bennett et al. [57], assuming identical initial MEMS and the same number of photon pairs[16]. In the following analysis we use the entanglement of formation (E_F) to benchmark the success of the concentration. The entanglement of formation for a density matrix ρ is given by [39]

$$E_F(\rho) \equiv h(\frac{1}{2}[1 + \sqrt{1 - T(\rho)}]), \tag{4.8}$$

---

[16] The numbers for the interference-based concentration in this comparison were calculated by Tzu-Chieh Wei.

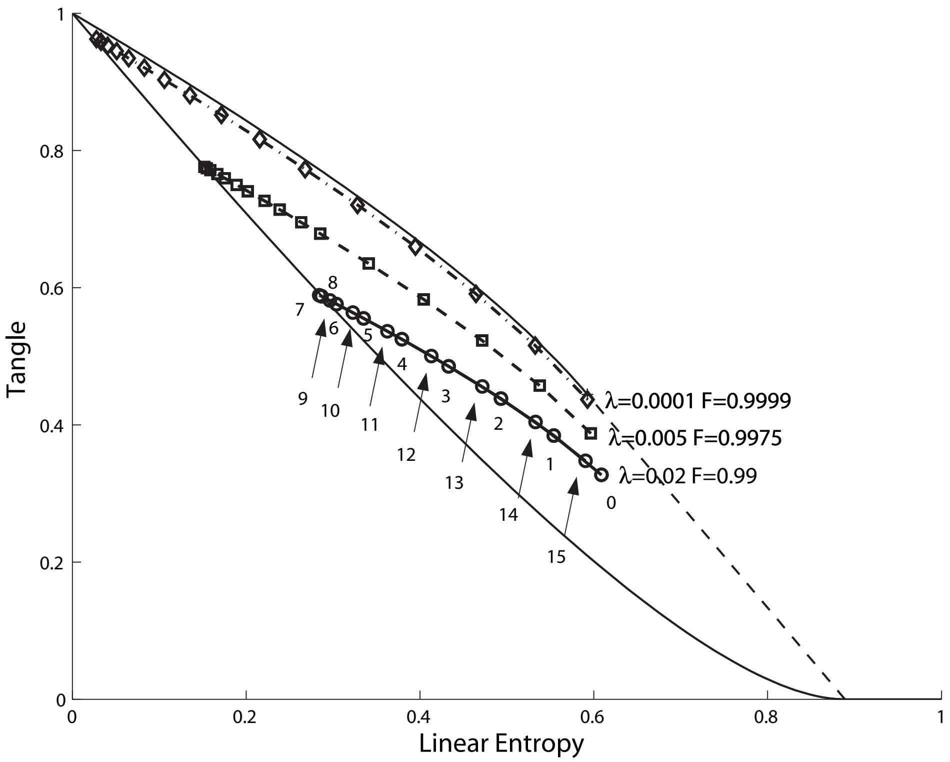

Figure 4.5: Investigation of the concentrate-ability of a MEMS state $\rho_2(\lambda, r) \equiv (1-\lambda)\rho_{MEMSI}(r) + \frac{\lambda}{4}\mathbb{1}$ (nominally with $r = \frac{2}{3}$), as a function of additional noise λ. Each step of a 15-element concentration calculation (corresponding to 1 to 15 glass pieces per experimental arm as in Fig. 4.4) is plotted for initial states of the form of $\rho_2(\lambda, r = \frac{2}{3})$. Shown are the depolarizing parameters (λ) along with the fidelity (F) of the "noisy" starting state with the ideal MEMS. Each concentration step uses the same transmission coefficients as in Fig. 4.4. Observe that relatively small perturbations in the initial state can drastically alter its concentrate-ability. Just as in Fig. 4.4 (a), here we also see that excessive concentration steps actually *unconcentrate* the state. For example, in the $\lambda = 0.02$ case, 1 to 7 concentrating steps increase the state's purity and tangle while the remaining steps undo the concentration. In the $\lambda = 0.0001$ case, all fifteen elements increase the tangle and purity. Note that the maximum concentration is reached at the Werner-state line. At this point, the most-reduced and least-reduced diagonal elements (see equation 4.7) are equal.

where $T(\rho)$ is the tangle, and $h(x) \equiv -x\log_2(x) - (1-x)\log_2(1-x)$, the relation between E_F and $T$is plotted in Fig. 4.6. We shall compare the average final entanglement of formation (i.e., the E_F of the concentrated state multiplied by the probability of success) *per initial pair*. Thus, the figure of merit we consider, the E_F per pair, is the product of the probability of a successful concentration and the E_F when a concentration succeeds divided by the number of photon pairs needed to attempt the concentration protocol. The Bennett el al. [57] scheme was recently approximated by Pan et al. [50], with CNOT operations replaced by polarizing beam splitters; however, due to incomplete

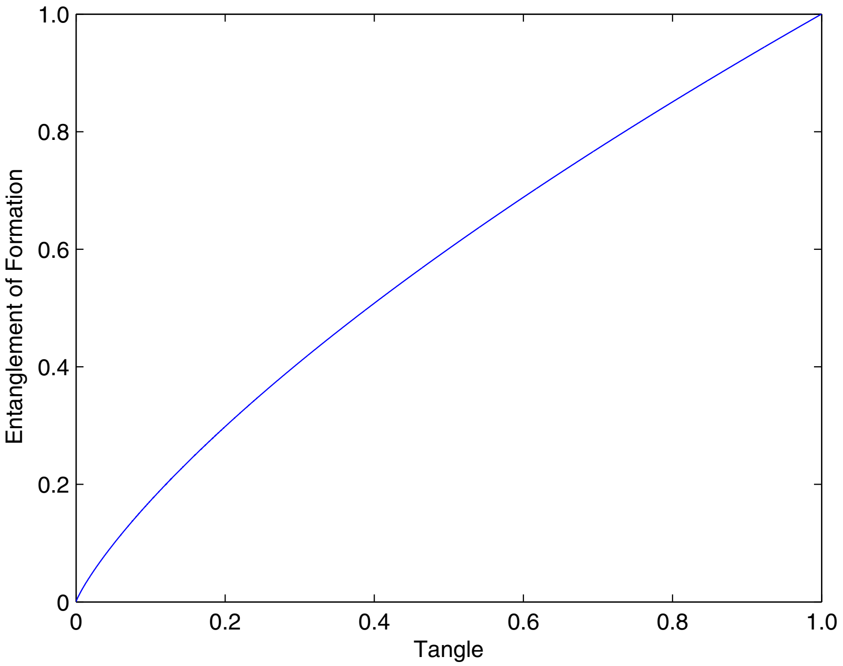

Figure 4.6: Entanglement of formation (E_F) vs. Tangle.

Bell state analysis, the probability of successful concentration is only 50% of the original proposal (the alternate concentration scheme of Yamamoto et al. [51] is wholly unable to distill MEMS). In general, the first step of both schemes is to perform a "twirling" operation[17] to transform a general entangled state into a Werner state [57, 50]; however, this initial operation usually *decreases* the entanglement, and the scheme with twirling is efficient only when r (the concurrence of the MEMS) is close to 1. In fact, MEMS I could also be distilled *without* the twirling operation, using the scheme of Pan et al.

For most MEMS, the maximum distillation efficiency from filtration can exceed that achievable using the interference-based methods. For example, as shown in Table 4.1, when the initial state is a MEMS with $r = 0.778$, the two-piece filtering technique has a theoretical E_F per pair nearly three times higher than the interference scheme without twirling, even though a successful concentration produces nearly the same E_F. If instead we allow for twirling in the interference scheme, the probability of success is nearly 50% higher than in the Procrustean case, but the entanglement

---

[17] In "twirling," a random SU(2) rotation is independently performed on each photon pair.

Concent. method	Prob. of success	E_F when successful	Ideal E_F per pair	Exp. E_F per pair
Twirling [57]	74.8%	0.51	0.19	NA
No Twirling [50]	35.2%	0.80	0.14	$\lesssim 10^{-5}$
Procrustean				
2 pieces	50.4%	0.81	0.41	0.35
4 pieces	26.4%	0.88	0.23	0.17
6 pieces	14.2%	0.93	0.13	0.08

Table 4.1: Efficiency comparison of concentration technique of Bennett et al. using ideal CNOT [57], interference-based concentration [50] without twirling, and Procrustean filtering, for an initial MEMS with $r = 0.778$ and $E_F = 0.69$. The scheme of Bennett et al. requires a twirling operation that decreases the initial E_F to 0.418 before the concentration. In all schemes, except for the final column, we assume the ideal case, i.e., no loss and perfect detector efficiency. To calculate the no-loss result for our filtering scheme, we normalize the measured partial polarizer transmission coefficients (of a single glass piece) to $T_V = 0.740/0.990$ and $T_H = 1$. In the interference schemes, columns 2-4 assume the existence of the required two identical pairs, but in practice this requirement is difficult to achieve. Because it is presently very difficult to produce simultaneous indistinguishable *pairs* of photons, the filtration technique is *much* more efficient, e.g., where typically 20% of our incident ensemble of pairs survived, less than 0.005% would survive (estimated from the 2-fold and 4-fold coincidence data reported in [50]) in the interference schemes, which require 4 photons. This limitation is reflected in column 5, which lists the average E_F per initial pair achieved in our experiment (here our starting state had E_F=0.58 instead of 0.69 for the theoretical calculations; thus the values in the last column appear lower than those in the next to last column [58]), to be compared with the much lower value ($\lesssim 10^{-5}$) achievable with current interference method technology.

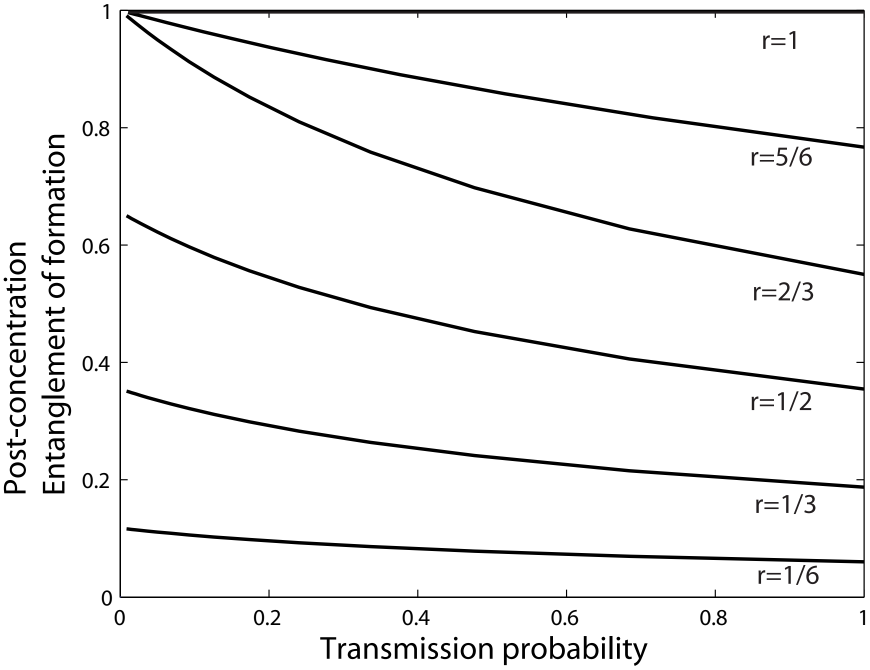

Figure 4.7: Entanglement of formation (E_F) vs. transmission probability in Procrustean concentration. Curves show Procrustean concentration for several initial MEMS with varying r. Assuming $T_V = 0.740/0.990$ and $T_H = 1$, the curves represent the transmissions and entanglements of successful Procrustean concentration for a range of 0 to 15 concentrating elements. Not surprisingly, an attempt to concentrate the maximally entangled state (r=1) does nothing to its E_F, it is a horizontal line at E_F=1. Note that states with $r < \frac{2}{3}$ cannot be concentrated to a maximally entangled state by this method.

of formation is over one third less. In theory, using 2 to 4 slips in the Procrustean concentration achieves both higher entanglement of the successful state and better average entanglement yield, regardless of whether twirling is used in the interference technique. With 6 slips the resulting E_F, when successful, is higher still, but the loss inherent in the Procrustean method leads to a lower theoretical E_F per pair. In practice, the filtration technique is *much* more efficient (see the final columns of Table 4.1). To illustrate the theoretical efficiency of the filtration technique for several distinct starting MEMS we made a plot of E_F as a function of the transmission probability (N, from equation 4.7) through a partial polarizer (see Fig. 4.7).

We have demonstrated a tunable source of high fidelity MEMS. As a consequence of comparing the T-S_L and fidelity values of generated MEMS with the theoretical targets, we have identified and explained an unsuspected difference in sensitivity in these state measures. Furthermore, we have applied a Procrustean filtering technique to several MEMS, realizing a measured efficiency that is well above that achievable using other methods. However, in the limit of very strong filtering, small perturbations in the initial state will eventually dominate the process, yielding only product states (see Fig. 4.4). In practice, therefore, it may be optimal to combine both methods of entanglement concentration. In this case, an ensemble of identically prepared photons could be divided such that the first fraction could be measured via tomography to choose the optimal Procrustean filter. Then, Procrustean concentration may be carried out until the state reaches its maximum entanglement (as shown in Figs. 4.4(a) and 4.5). At this point, interference-based concentration methods could be applied to achieve maximally entangled states.

Chapter 5

On common quantum information benchmarks

The outcome of most quantum information protocols hinges on the quality of the initial state. Often the optimal input states are pure maximally entangled states. However, decoherence and dissipation inevitably decrease the purity and entanglement of resource states, yielding partially entangled mixed states. The most common measure used to benchmark a starting state resource is the fidelity [28], as used, e.g., in entanglement purification [57, 59] and optimal mixed state teleportation [60]. Likewise, the success of these procedures is often judged using the fidelity of the output state with some target, as is the case, for example, in quantum cloning [61]. As we saw in the previous chapter, for the specific case of maximally entangled mixed states [45, 46, 44] (MEMS), using the fidelity to compare an experimentally produced state and a target state was a less sensitive way of assessing experimental agreement than comparing the tangle [62, 63] and the linear entropies [40] of those states [52]. Because one needs to understand the best way to benchmark states for quantum information protocols, here we examine the fidelity for more general entangled two-qubit mixed quantum states and note its behavior in relation to the common state measures of linear and von Neumann entropy, tangle and concurrence, and trace distance.

After some general calculations for depolarized states[1], we consider explicitly a one-qubit state as a warmup exercise and then two classes of two-qubit entangled states acted on with depolarizing channels: nonmaximally entangled states and maximally entangled mixed states. The effect of a depolarizing channel is to make the states we study similar to the Werner states (an incoherent combination of a pure maximally entangled state and completely mixed state) [64], which have

---

[1] The lion's share of these calculations were done by Tzu-Chieh Wei.

been realized with polarized photons [43, 55]. These two classes of states were chosen because they allow us to study mixed-state entanglement, and also to understand how states change under uniform depolarization. Such a uniform depolarization model is applicable to many examples of real experimental decoherence. Parts of the work in this chapter were published in references [52, 53, 65].

5.1 General sensitivities of measures

Before considering specific examples of entangled mixed states, we examine general sensitivities for several measures using generic depolarized density operators. The depolarized N-level system ($N = 2$ for a qubit, $N = 4$ for two qubits, etc.) is

$$\rho \rightarrow \rho' = (1-\epsilon)\rho + \frac{\epsilon}{N}\mathbb{1}_N, \tag{5.1}$$

where ϵ is the strength of depolarization.

5.1.1 Fidelity

Recall that for direct comparison of two mixed states, e.g., ρ_t (target states) and ρ_p (perturbed states), we used the fidelity (equation 2.18):

$$F(\rho_t, \rho_p) \equiv \left| \mathrm{Tr}\left(\sqrt{\sqrt{\rho_t}\rho_p\sqrt{\rho_t}}\right)\right|^2. \tag{5.2}$$

It is important to note that some researchers, as in [66], use an amplitude version of the fidelity: $f \equiv \sqrt{F}$. In either case, the fidelity is zero for orthogonal states and one for identical states.

Because we wish to consider small perturbations in the fidelity, the "amplitude version" f should be less sensitive because it lacks the square. We consider a generic state ρ having eigenvalues $\{\lambda_i\}$, depolarized by ϵ. The amplitude fidelity f between the output state ρ' and the input ρ is

$$\begin{aligned} f(\rho, \rho') &= \mathrm{Tr}\sqrt{(1-\epsilon)\rho^2 + \frac{\epsilon}{N}\rho} && (5.3)\\ &= \sum_i \sqrt{(1-\epsilon)\lambda_i^2 + \frac{\epsilon}{N}\lambda_i}. && (5.4)\end{aligned}$$

We assume ϵ is small such that $\epsilon \ll N\lambda/|1-N\lambda|$, where λ is the smallest nonzero eigenvalue. Thus, we can expand the above expression to second order in ϵ:

$$\begin{aligned} f &\approx \sum_{\lambda_i \neq 0} \lambda_i \left\{ 1 + \frac{1}{2}\left(\frac{1-N\lambda_i}{N\lambda_i}\right)\epsilon - \frac{1}{8}\left(\frac{1-N\lambda_i}{N\lambda_i}\right)^2 \epsilon^2 \right\} \\ &= 1 - \left(\frac{1}{2} - \frac{n_\otimes}{2N}\right)\epsilon - \sum_{\lambda_i \neq 0} \frac{\lambda_i}{8}\left(\frac{1-N\lambda_i}{N\lambda_i}\right)^2 \epsilon^2 + \mathcal{O}(\epsilon^3), \end{aligned} \tag{5.5}$$

where $n_\otimes$ is the number of nonzero eigenvalues of ρ. When ρ is of full rank (i.e., $n_\otimes = N$), the first-order term vanishes, and the fidelity is sensitive only to second order in the small depolarizing parameter. If ρ is not full rank, f *is* sensitive to first order, but becomes less so as the rank becomes higher. Note that squaring the result (5.5) in fact gives the *same* order of sensitivity for F.

5.1.2 Trace distance

Another possible measure used to compare two states is the trace distance [66], given by

$$D(\rho_t, \rho_p) \equiv \frac{1}{2}\mathrm{Tr}|\rho_t - \rho_p|. \tag{5.6}$$

Evaluating the trace distance using (5.1) gives

$$D(\rho, \rho') = \frac{1}{2}\sum_i \mid \lambda_i - \frac{1}{N} \mid \epsilon. \tag{5.7}$$

Here, the $1/N$ term comes from the $N \times N$ mixed state ($\mathbb{1}_N/N$) used to depolarize ρ to create ρ' (5.1). Thus, we see that the trace distance is always *linearly* sensitive to the strength of depolarization, except when $\rho = \mathbb{1}_N/N$, i.e., the fully mixed state. Consequently, the difference between two similar states will in general be less apparent when using f (or F) than when using D.

5.1.3 Linear entropy

To quantify the mixedness of a given state ρ, we first consider the linear entropy (S_L), which is based on the purity, and for an N-level system is given by

$$S_{\mathrm{L}}(\rho) \equiv \frac{N}{N-1}[1-\mathrm{Tr}(\rho^2)]. \tag{5.8}$$

Recall that the linear entropy is zero for pure states and one for completely mixed states, i.e., $S_L = 1$ for the normalized N-qubit identity $\mathbb{1}_N/N$. The change in the linear entropy under a depolarizing channel is

$$\Delta S_{\mathrm{L}} \equiv S_{\mathrm{L}}(\rho') - S_{\mathrm{L}}(\rho) = (2\epsilon - \epsilon^2)(1 - S_{\mathrm{L}}). \tag{5.9}$$

Therefore, as with trace distance, the linear entropy is always linearly sensitive in ϵ, except when $S_{\mathrm{L}}(\rho) = 1$, namely, when ρ is the fully mixed state $\mathbb{1}_N/N$. Thus, the linear entropy is also, in general, more sensitive to the depolarizing channel than the fidelity.

5.1.4 von Neumann entropy

Another frequently encountered entropy measure is the von Neumann entropy:

$$S_{\mathrm{V}}(\rho) \equiv -\mathrm{Tr}\left(\rho \ln \rho\right). \tag{5.10}$$

Using (5.1) and evaluating $\Delta S \equiv S_{\mathrm{V}}(\rho') - S_{\mathrm{V}}(\rho)$ to first order gives

$$\Delta S \approx -\frac{n_0}{N}\epsilon \ln \epsilon + \epsilon \left(1 - S_{\mathrm{V}}(\rho) - \frac{n_\otimes}{N} + \frac{n_0}{N}\ln N - \frac{1}{N}\sum_{\lambda_i \neq 0} \ln \lambda_i\right),$$

where $n_\otimes$ (n_0) is the number of nonzero (zero) eigenvalues of ρ, and $n_\otimes + n_0 = N$. When ρ is not a full rank matrix (i.e., $n_0 \neq 0$), the von Neumann entropy is, to leading order, sensitive in $\epsilon \ln \epsilon$ (stronger than order ϵ). As the rank become higher, this $\epsilon \ln \epsilon$ sensitivity decreases. When ρ is of full rank (i.e., $n_0 = 0$ and $n_\otimes = N$), the von Neumann entropy is linearly sensitive in ϵ unless $S_{\mathrm{V}} = -\frac{1}{N}\sum_i \ln \lambda_i$, which is again possible only when $\lambda_i = 1/N$, i.e., for the fully mixed state $\rho = \mathbb{1}_N/N$.

5.1.5 Concurrence and tangle

Here, we examine two ways of quantifying the entanglement of a system, restricting our attention to two-qubit states. We will first derive the variation of the concurrence for an entangled state acted on by a depolarizing channel, then use this to find the result for the tangle, which is the concurrence squared as introduced in Section 3.3.

Concurrence

The concurrence is given by [62]

$$C(\rho) \equiv \max\{0, \sqrt{\lambda_1} - \sqrt{\lambda_2} - \sqrt{\lambda_3} - \sqrt{\lambda_4}\}, \tag{5.11}$$

where λ_i are the eigenvalues of $\rho\tilde{\rho}$ in non-increasing order by magnitude. Here, we define $\tilde{\rho} \equiv (\sigma_2 \otimes \sigma_2)\rho^*(\sigma_2 \otimes \sigma_2)$ with $\sigma_2 = \begin{pmatrix} 0 & -i \\ i & 0 \end{pmatrix}$.

If ρ is unentangled, ρ', which has additional noise, is still unentangled. Now suppose the state ρ is entangled, so that $C(\rho) = \sqrt{\lambda_1} - \sqrt{\lambda_2} - \sqrt{\lambda_3} - \sqrt{\lambda_4}$. To find the concurrence of ρ', we have to evaluate the eigenvalues of the matrix

$$\rho'\tilde{\rho'} = (1-\epsilon)^2\rho\tilde{\rho} + \frac{\epsilon}{4}(1-\epsilon)(\rho + \tilde{\rho}) + \frac{\epsilon^2}{16}\mathbb{1}_4. \tag{5.12}$$

We can treat the last two terms as perturbations and evaluate the eigenvalues to leading order:

$$\lambda_i' \approx (1-\epsilon)^2\lambda_i + \frac{\epsilon}{4}(1-\epsilon)\langle\rho + \tilde{\rho}\rangle_i + \frac{\epsilon^2}{16}, \tag{5.13}$$

where

$$\langle\rho + \tilde{\rho}\rangle_i \equiv \langle\lambda_i|(\rho + \tilde{\rho})|\lambda_i\rangle. \tag{5.14}$$

For $\epsilon < \lambda$, where λ is the smallest nonzero value of $\{\lambda_i\}$, we have, to leading order,

$$\sqrt{\lambda_i'} \approx (1-\epsilon)\sqrt{\lambda_i} + \frac{\epsilon}{8\sqrt{\lambda_i}}\langle \rho + \tilde{\rho}\rangle_i. \tag{5.15}$$

Hence, the change in concurrence ($\Delta C \equiv C(\rho') - C(\rho)$), is given by

$$\begin{aligned} \Delta C \ &\approx \ -\sum_{\lambda_i=0} \sqrt{\frac{\epsilon}{4}(1-\epsilon)\langle \rho + \tilde{\rho}\rangle_i + \frac{\epsilon^2}{16}} - \epsilon\, C(\rho) \\ &\quad + \frac{\epsilon}{8}\left(\frac{\langle \rho + \tilde{\rho}\rangle_1}{\sqrt{\lambda_1}} - \sum_{i=2,\lambda_i\neq 0}^{4} \frac{\langle \rho + \tilde{\rho}\rangle_i}{\sqrt{\lambda_i}} \right). \end{aligned} \tag{5.16}$$

When $\rho\tilde{\rho}$ is full rank, the variation of concurrence is thus at worst first order in ϵ, except for the unlikely case that

$$C(\rho) = \frac{\langle \rho + \tilde{\rho}\rangle_1}{8\sqrt{\lambda_1}} - \sum_{i=2,\lambda_i\neq 0}^{4} \frac{\langle \rho + \tilde{\rho}\rangle_i}{8\sqrt{\lambda_i}}, \tag{5.17}$$

where, ΔC=0. When $\rho\tilde{\rho}$ is not full rank, ΔC varies as $\sqrt{\epsilon}$.

Tangle

To characterize a state's entanglement, one may also use the tangle [62, 63], i.e., the concurrence squared:

$$T(\rho) \ = \ C(\rho)^2. \tag{5.18}$$

Using the result for variation in concurrence, the variation of tangle can now be expressed as $T' - T \approx 2C\Delta C$. Thus, the tangle is also typically sensitive in the first order to depolarizing perturbations.

In summary, we have thus far shown that, except for the special cases noted above, under the influence of a small depolarizing channel the fidelity is generally not as sensitive as the change in trace distance, linear entropy, von Neumann entropy, concurrence, or tangle. Next, we shall illustrate this fact for specific states and investigate the situation for larger depolarization and for variable entanglement.

5.2 Investigation for specific states

5.2.1 One qubit

We start our exploration of noise effects with the most simple two-level quantum system–a qubit. To understand the influence of noise on a single-qubit state, we consider states of the following form[2]:

$$\rho_{d,1}(\epsilon,\theta) = (1-\epsilon)|\theta\rangle\langle\theta| + \frac{\epsilon}{2}\mathbb{1}_2, \tag{5.19}$$

where $|\theta\rangle = \cos\theta|0\rangle + \sin\theta|1\rangle$, $\mathbb{1}_2$ is the two-by-two identity and ϵ is the strength of the depolarization (mixedness). This "benchmark" state is an incoherent sum of a pure state ($|\theta\rangle$) and a fully mixed state ($\mathbb{1}_2$). From (5.8), the qubit's linear entropy is

$$S_L(\rho_{d,1}(\epsilon,\theta)) = 2\epsilon - \epsilon^2, \tag{5.20}$$

depending only on ϵ because the $|\theta\rangle$ part is pure. As the parameter θ does not affect the linear entropy, without loss of generality we set θ=0. To bound the variation in the state's behavior for different values of the mixedness (set by ϵ), we calculate the fidelity between the initial "target state" $\rho_{d,1}(\epsilon,0)$ and a slightly perturbed state $\rho_{d,1}(\epsilon+\delta\epsilon,0)$, where we have perturbed the mixedness by $\delta\epsilon$:

$$F(\rho_{d,1}(\epsilon,0),\rho_{d,1}(\epsilon+\delta\epsilon,0) = \frac{1}{4}(\sqrt{(\epsilon-2)(\epsilon+\delta\epsilon-2)} + \sqrt{\epsilon(\epsilon+\delta\epsilon)})^2. \tag{5.21}$$

From this expression, we can calculate the $\delta\epsilon$ that produces a given level of fidelity between $\rho_{d,1}(\epsilon,0)$ and $\rho_{d,1}(\epsilon+\delta\epsilon,0)$:

$$\delta\epsilon_{\pm}(\epsilon,\mathrm{F}) = 2(1-\mathrm{F}-\epsilon+\mathrm{F}\epsilon \pm \sqrt{\mathrm{F}(1-\mathrm{F})(2\epsilon-\epsilon^2)}). \tag{5.22}$$

Using $\delta\epsilon_{\pm}(\epsilon,\mathrm{F})$ we generate a series of perturbed states that have a specified fidelity with the target state, and then examine the linear entropy (S_L) of the perturbed states relative to that of the target. For example, $S_L(\epsilon)$, $S_L(\epsilon+\delta\epsilon_+)$ and $S_L(\epsilon+\delta\epsilon_-)$ are plotted in Fig. 5.1 for a fidelity of 0.99 (typically considered "high fidelity") as a function of ϵ. Note that for both a completely pure state (ϵ=0) and a completely mixed state (ϵ=1), $\delta\epsilon_+$ and $\delta\epsilon_-$ have the same magnitude; thus

---

[2] As the conclusions presented in this chapter are valid for *any* quantum system regardless of implementation, we will use the generic basis states $|0\rangle$ and $|1\rangle$ instead of $|H\rangle$ and $|V\rangle$.

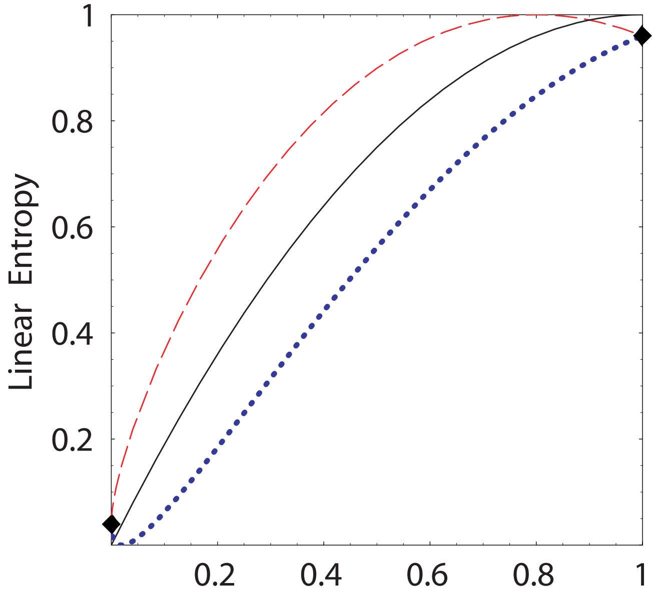

Figure 5.1: The linear entropy of a depolarized single-qubit state $|0\rangle$ as a function of an applied depolarizing channel (ϵ) (see (5.19)). The solid line is the linear entropy for the state $\rho_{d,1}(\epsilon, 0)$ while the dashed and dotted lines are curves for states ($\rho_{d,1}(\epsilon+\delta\epsilon_+)$ and $\rho_{d,1}(\epsilon+\delta\epsilon_-)$, respectively) that have 0.99 fidelity with $\rho_{d,1}(\epsilon)$. Diamonds at ϵ=0 and ϵ=1 show where the dashed and dotted lines touch (see text). When the dashed and dotted lines are above the solid line, they represent *de*polarizing behavior; when they are below the solid line, they arise from *re*polarizing behavior.

the linear entropy increases by 0.0396 for the pure state, and decreases by the same amount for the mixed state). In other words, the pure state *de*polarizes whereas the mixed state *re*polarizes to reach a 0.99 fidelity. When the target is a pure state, a ∼4% linear entropy increase can occur and still have 0.99 fidelity with the initial pure state. Things are much worse for partially mixed states. For example, the linear entropy is 0.75 for $\epsilon = 0.5$, but the 0.99-fidelity states have linear entropies of 0.90 (depolarized dashed line of Fig. 5.1) and 0.56 (repolarized dotted line).

Thus, we see that the sensitivity of S_L to constant-fidelity perturbations in the previous method depends critically on the entropy of the starting state itself. When we perturb an initial state with parameter ϵ by $\delta\epsilon_+$ and $\delta\epsilon_-$, we see how much the linear entropy can change while maintaining a constant fidelity between the initial and perturbed states. Although this bound creates a curve for a continuum of states based on the parameter ϵ, we shall soon see when we consider the tangle and linear entropy for two-qubit states, that we can map the behavior with more flexibility than that of the two points provided by $\delta\epsilon_+$ and $\delta\epsilon_-$.

5.2.2 Two qubits

We now consider a state similar to the Werner state, but we allow *arbitrary* entanglement through the use of a variable nonmaximally entangled pure state component in addition to the mixed state dilution:

$$\begin{aligned} \rho_1(\epsilon,\theta) &\equiv (1-\epsilon)|\Psi(\theta)\rangle\langle\Psi(\theta)| + \frac{\epsilon}{4}\mathbb{1}_4, \quad \text{with} && (5.23) \\ |\Psi(\theta)\rangle &\equiv \cos\theta|00\rangle + \sin\theta|11\rangle, && (5.24) \end{aligned}$$

where the parameter θ controls the entanglement and ϵ the mixedness. We choose this parameterization for simplicity and because the entropy and the entanglement of the state are somewhat uncoupled from each other, e.g., a change in θ only changes the entanglement, not the mixedness. In this case, the concurrence is $C(\rho_1(\epsilon,\theta)) = \max\{0, 2(1-\epsilon)\cos\theta\sin\theta - \epsilon/2\}$ (assuming $\cos\theta\sin\theta \geq 0$) and the linear entropy depends only on ϵ, $S_L(\rho_1(\epsilon,\theta)) = 2\epsilon - \epsilon^2$.

In a similar way to equation (5.23), we depolarize a maximally entangled mixed state (MEMS)

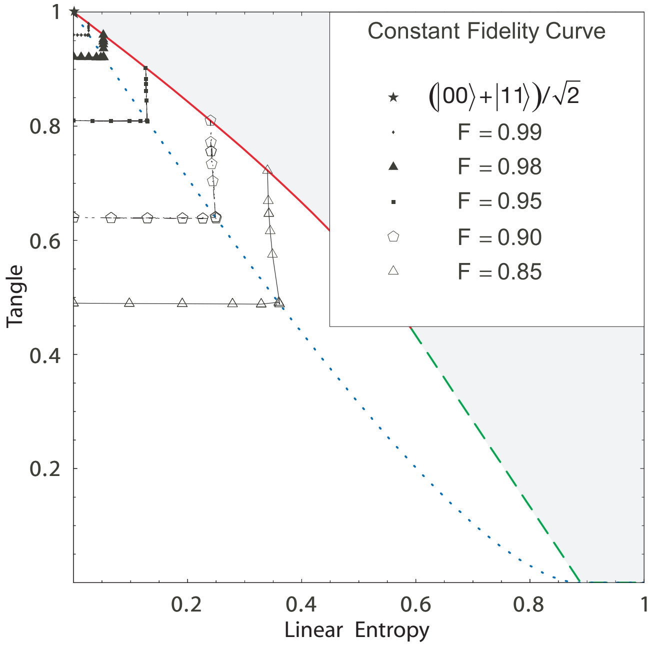

Figure 5.2: Constant fidelity curves for the maximally entangled state $(|00\rangle + |11\rangle)/\sqrt{2}$ (star, upper left corner). Also shown are the Werner state curve (dotted line) and, bounding the gray region of nonphysical entropy-tangle combinations, the MEMS curve, which is solid for $\rho_{MEMS\ I}$ and dashed for $\rho_{MEMS\ II}$. The (horizontal) constant fidelity curves below the Werner state curve are swept out by comparing the starting state with states of the form $\rho_1(\epsilon, \theta)$, equation (5.23), while the (nearly vertical) curves above the Werner state line are generated by varying the parameters of $\rho_2(\epsilon, r)$ given by equation (5.25). For comparison, the pure product state $|00\rangle$ (lower left corner) has fidelity of 0.5 with this target.

according to

$$\rho_2(\epsilon, r) \equiv (1 - \epsilon)\rho_{MEMS}(r) + \frac{\epsilon}{4}\mathbb{1}_4, \tag{5.25}$$

where the MEMS, using the parameterizations of concurrence (r) and linear entropy, is given by equations (4.1) for $\frac{2}{3} \leq r \leq 1$ and equation (4.2) for $0 \leq r \leq \frac{2}{3}$.

With these parameterizations we may map out constant fidelity curves between a target state and a perturbed state in the linear entropy-tangle plane (we choose these particular measures for calculational simplicity and because (5.23) and (5.25) cover the entire physically allowed region of the plane). It is our purpose to use these curves to gain insight as to how the entanglement and mixedness may vary over a constant fidelity curve and how this variation may in turn depend on the amount of entanglement and mixedness. To do this, we calculate the fidelity between a target noisy nonmaximally entangled state $\rho_1(\epsilon_t, \theta_t)$ and a perturbed state $\rho_1(\epsilon_p, \theta_p)$. Specifically, the parameters ϵ_p and θ_p are varied to create perturbed states of all possible tangle and entropy values, as long as the perturbed state has a given fidelity with the target. Likewise, the process is repeated for a noisy MEMS $\rho_2(\epsilon_t, r_t)$, varying the parameters of $\rho_2(\epsilon_p, r_p)$.

In the pure, maximally entangled limit, both (5.23) and (5.25) reduce to the maximally entangled state $|\Phi^+\rangle \equiv (|00\rangle + |11\rangle)/\sqrt{2}$. Therefore, this is a natural state with which to start our discussion. Because (5.23) and (5.25) occupy different regions of the entropy-tangle plane, it is not surprising that we need to use both equations to map out the constant fidelity curves for $|\Phi^+\rangle$, as shown in Fig. 5.2. The horizontal curves in the region bounded above by the Werner state curve, are traced out by computing the fidelity of $|\Phi^+\rangle$ with (5.23). This fidelity is $F = (1 + \sqrt{T})/2$ and, surprisingly, does not explicitly depend on the depolarization of the perturbed state. The maximal fidelity of any two-qubit state with maximally entangled pure states was found by Verstraete and Verschelde [67] to be bounded above by $(1+\sqrt{T})/2$. The two-qubit states (5.23) saturate this bound (as does any two-qubit pure state). Any entangled state that saturates this bound apparently has $F > 1/2$, thus allowing concentration of entanglement via the Bennett et al. scheme [57] without requiring local filtering [68]. Another consequence of this simple fidelity expression is that, when comparing (5.23) with $|\Phi^+\rangle$, the fidelity by itself cannot distinguish between pure nonmaximally entangled states and Werner states of the same tangle. For example, both the nonmaximally entangled pure state $\rho_1(0, 22.5°)$ and the Werner state $\rho_1(0.19525, 45°)$ have tangle equal to 0.5, and each has fidelity 0.854 with $|\Phi^+\rangle$[3].

To trace the curves above the Werner state line, we calculate the fidelity of $|\Phi^+\rangle$ with equation (5.25). In this case, the analytical expression for the fidelity does not provide much insight, so we only present numerical results, yielding the nearly vertical curves shown in Fig. 5.2. Notice that the vertical curves scale nearly the same as the horizontal curves, e.g., when the horizontal is 20% from the target state's value, so is the vertical curve. Thus, when comparing $|\Phi^+\rangle$ with states created using (5.23) and (5.25) that each separately have the same fidelity with $|\Phi^+\rangle$, the linear entropy

---

[3] Suppose one had a choice between two equally entangled states (as measured by the tangle), a Werner state and a pure non-maximally entangled state (this condition is true when $\epsilon = \frac{2}{3}(1 - \sin\theta)$, i.e., for $\rho_1(\frac{2}{3}(1 - \sin\theta), 45°)$, and $\rho_1(0, \theta)$); which would be a better entangled resource for teleportation? It is somewhat surprising that both states teleport a qubit with the same fidelity. One might naively assume that given the choice between a pure state and a partially mixed state, both with the same entanglement, one should choose the pure state for the best performance in other quantum protocols. However, since this is not true for our teleportation example, it may be interesting to investigate generalizations for other protocols.

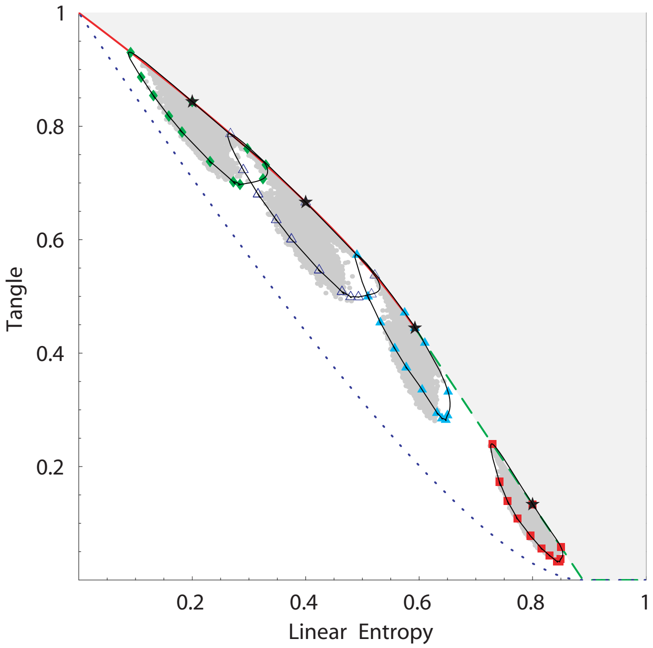

Figure 5.3: Constant 0.99-fidelity curves for several starting MEMS, plotted as stars. The constant fidelity curves are calculated by comparing the target state with $\rho_2(\epsilon, r)$ where ϵ and r are varied to give different tangles and linear entropies. The dark gray regions are 20000 points per initial MEMS, corresponding to numerically generated density matrices that have fidelity of 0.9900 or higher with the target.

and tangle for (5.23) and (5.25) change by about the same amount when the fidelity changed. So (5.23) and (5.25) display approximately the same fidelity insensitivity.

As the theoretical investigations in this chapter were motivated by an observed insensitivity when comparing target and experimental MEMS using the tangle, linear entropy and fidelity, next we consider the effect of depolarization on maximally entangled mixed states (MEMS). In this case, we calculate the 0.99-fidelity curve for several target states, shown as stars in Fig. 5.3. Note that the 0.99-fidelity curve encloses a much larger area for any of the MEMS targets than it does for the $|\Phi^+\rangle$ calculation (Fig. 5.2). We attribute this to the fact that depolarizing a pure state changes the fundamental character (as measured with the fidelity) of the state more than does depolarizing an *already* mixed state. Also shown in Fig. 5.3 are the results of a numerical Monte Carlo simulation, where we assumed an ideal starting state, then calculated the predicted counts one would expect to measure in an experiment if there were no measurement noise or fluctuations. These ideal counts are then perturbed in a statistical way to give a variation one might expect in an experimental measurement for a total collection of ~2000 counts[4]. Note that the sizes and shapes of the simulation and the constant fidelity curves are similar but not identical. As the simulation is random, it behaves somewhat like a depolarizing channel, adding uniform noise (explaining some of the similarity); however, random fluctuations are not enough to mimic the extreme changes along the MEMS curve, as the MEMS density matrices posses very specific forms.

What if we consider only small perturbations (δr) of the MEMS parameter r? For such perturbations, the fidelity between perturbed and unperturbed MEMS is only quadratic[5] in δr, whereas S_L and T are linear in δr. This helps explain some of the sensitivity imbalance noted in chapter 4. However, recall that noise in the $|HH\rangle\langle HH|$ element of the concentrated MEMS density matrix eventually caused the state to become a pure product state under extreme filtering.

The two previous cases dealt with states that have the highest entanglement values, i.e., they are bounded by the edges of the physically allowed regions of the entropy-tangle plane. To investigate

---

[4] If the fidelity between the perturbed density matrix and the target state is greater than 0.9900, the tangle and linear entropy are calculated and plotted in Fig. 5.3. This simulation is essentially the same as the one used for Fig. 4.2 (b).

[5] The leading order normalized behaviors for the measures about a target value $\rho_{MEMSi}(r_0) \equiv \rho_i(r_0)$ by an amount $\delta r \equiv r - r_0$ are $S_L(\rho_i(r))/S_L(\rho_i(r_0)) \approx 1 - A_i\delta r$, $T(\rho_i(r))/T(\rho_i(r_0)) \approx 1 + \frac{2}{r_0}\delta r$, and $F(\rho_i(r_0), \rho_i(r)) \approx 1 + B_i(\delta r)^2$, where the subscript i denotes the class of MEMS, and the constants are given by $A_I = \frac{2r_0-1}{r_0(1-r_0)}$, $A_{II} = \frac{2r_0}{\frac{4}{3}-r_0^2}$, $B_I = \frac{-1}{4r_0(1-r_0)}$, and $B_{II} = \frac{3}{2(9r_0^2-4)}$.

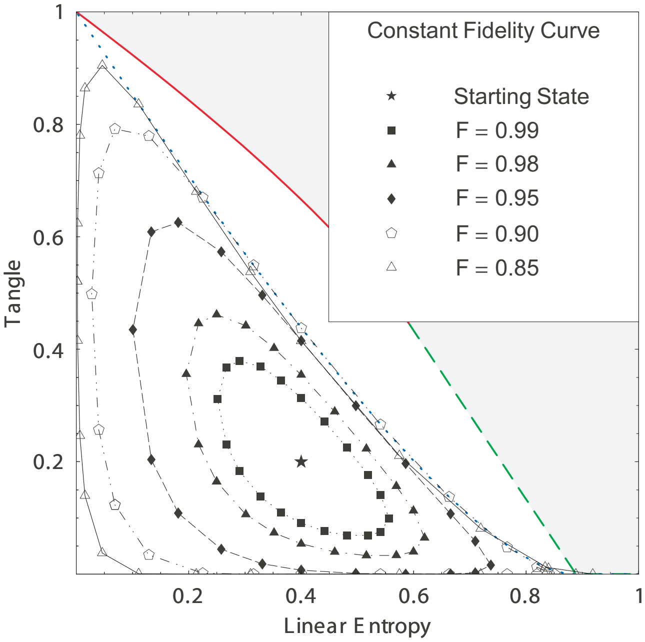

Figure 5.4: Constant fidelity curves for a nonmaximally entangled mixed state ($\rho_2(\epsilon = 0.225, \theta = 23.14°)$) compared with states calculated by varying ϵ and θ. In the case of this mixed entangled state, the constant fidelity regions are surprisingly large: for example, a 0.9 fidelity with this starting state could arise from a nearly pure entangled state or from an unentangled near fully mixed state. The 0.9 and higher fidelity region covers ∼60% of the physically allowed region of the linear entropy-tangle plane.

the behavior "on the open plane," we examine an entangled mixed target state that is a specific example of (5.23):

$$\rho_1(\sim 0.225, \sim 23.14^\circ) = \begin{pmatrix} 0.7113 & 0 & 0 & 0.2800 \\ 0 & 0.0564 & 0 & 0 \\ 0 & 0 & 0.0564 & 0 \\ 0.2800 & 0 & 0 & 0.1760 \end{pmatrix}, \tag{5.26}$$

which is shown as a star in Fig. 5.4. Note that the 0.99-fidelity region is much larger than for any of the previous target states, including the MEMS. This result is particularly astonishing when viewed in light of what is typically considered "high fidelity" experimentally for entangled states: 0.9 to 0.99 depending on the particular two-qubit implementation (although we saw in chapter 2 some *single* qubit fidelities are higher [21]). Consider the 0.9-fidelity curve in Fig. 5.4. This level of fidelity with the target states could mean one has a nearly pure maximally entangled state ($S_L \cong 0.07, T \cong 0.79$) or a nearly completely mixed unentangled state ($S_L \cong 0.85, T = 0$).

The extreme insensitivity of the fidelity for the target state (5.26) is consistent with equation (5.5), which indicates that fidelity sensitivity drops off as the rank of a state increases. In this case (5.26) has rank four whereas the MEMS have either rank two or three (and the maximally entangled pure state $|\Phi^+\rangle$ is rank 1); thus (5.26) exhibits larger constant fidelity curves than the MEMS or $|\Phi^+\rangle$. In addition, we conjecture that this effect may be further exacerbated because the addition of symmetric noise to an already highly mixed state (which has a symmetric form) changes the character of the state less than for a MEMS (which has an asymmetric form).

In summary, we have shown an imbalance between the sensitivities of the common state measures–fidelity, trace distance, concurrence, tangle, linear entropy and von Neumann entropy–for two classes of two-qubit entangled mixed states. This imbalance is surprising in light of the fact that orthogonal states which have zero fidelity with one another may have the same entanglement and mixedness; thus, one might have expected the fidelity to be a *more* sensitive means to characterize a state than quantifying state properties like entanglement and mixedness. Here we have shown an opposite effect. Specifically, we have investigated several examples at different locations in the entropy-tangle plane, where the trend shows progressively larger 0.99-fidelity regions as the state becomes more mixed and less entangled. We also have shown that, at least for maximally entangled target states, the fidelity is insensitive when comparing between Werner states and nonmaximally entangled states of the same tangle. This work has important ramifications for benchmarking the performance of quantum information processing systems, as it reveals that the usually quoted measure of fidelity is often a remarkably poor indicator, e.g., of the entanglement in a state, on which the performance of quantum information systems often depend. This may have consequences, for example, for determining the limits of fault tolerant quantum computation [69], and it may be beneficial to include other benchmarks in addition to/instead of fidelity, when characterizing resources needed for various quantum information protocols.

Chapter 6

Remote state preparation

Quantum communication is concerned with the transmission, manipulation, and detection of quantum information. Until now, this dissertation has been concerned primarily with the manipulation and detection of quantum information. In this chapter, we will take a closer look at the transmission of quantum information.

If a sender (Alice) wants to transmit an *unknown* quantum state to a receiver (Bob), they may use teleportation [6]. However, it has been shown [70, 71, 72] that the classical communication costs for sending a *known* state using remote state preparation (RSP) are less than those of teleportation. RSP is a quantum communication protocol that relies on correlations between two entangled qubits, similar to teleportation, to prepare Bob's qubit in a particular state determined by Alice, conditional on the outcome of a measurement on her qubit. However, unlike teleportation, RSP does not require the sender to perform full Bell-state analysis, currently an experimental challenge for optical implementations. Thus, RSP is an attractive alternative to teleportation because it not only requires less classical communication than teleportation, but also does not require Bell-state analysis.

Thus far, several RSP demonstrations with varying degrees of control over remotely prepared qubits have been reported: pseudo-pure states using liquid-state NMR [73] and pure-state superpositions of vacuum and single-photon states [74]. However, until recently, no RSP implementation has achieved control over the three parameters required to prepare *arbitrary* single-qubit states. Specifically, we achieve arbitrary mixed state RSP by making general polarization measurements on one photon of a polarization-entangled pair. In addition, we derive bounds on the states that may be remotely prepared using arbitrary two-qubit entangled resources and discuss two specific cases in detail [75]. This chapter is based on work published in references [75, 76, 77].

6.1 Teleportation

Quantum teleportation [6, 78, 79] is one of the best known quantum communication protocols. In quantum teleportation Alice transmits an *unknown* quantum state to Bob. Suppose Alice has an unknown qubit of the form $|\beta_1\rangle \equiv a|H_1\rangle + b|V_1\rangle$ where a and b are unknown complex amplitudes that are normalized, i.e., $|a|^2 + |b|^2 = 1$, and the subscript denotes the qubit number. If Alice and Bob share two additional qubits in the entangled state $|\Psi^+_{2,3}\rangle$ (equation 3.4), then it can be shown that the state of the three-qubit system, when written in the Bell basis, is [6]

$$\begin{aligned}|\beta_1\rangle|\Psi^+_{2,3}\rangle =& \frac{1}{2}[|\Psi^+_{1,2}\rangle(-a|H_3\rangle - b|V_3\rangle) + |\Psi^-_{1,2}\rangle(-a|H_3\rangle + b|V_3\rangle) \\ &+ |\Phi^+_{1,2}\rangle(-b|H_3\rangle + a|V_3\rangle) + |\Phi^-_{1,2}\rangle(b|H_3\rangle + a|V_3\rangle)].\end{aligned} \tag{6.1}$$

Alice next makes a Bell state measurement on qubits 1 and 2 to reveal which unitary transformation must be applied to the third qubit to obtain $|\beta_3\rangle$. Finally, Alice tells Bob her result and he applies the required unitary transformation on his qubit; e.g., if she measures $|\Psi^+_{1,2}\rangle$, then she tells Bob to do nothing as he will have the state $a|H_3\rangle + b|V_3\rangle$. If, however, Alice had measured one of the other three Bell states, Bob would have to apply a unitary transformation to get $|\beta_3\rangle$. As Alice needs to tell Bob which of the four Bell states she measured, she must use at least two bits of classical communication. When Alice makes the Bell measurement, she learns nothing of the unknown state. Also, superluminal communication is prohibited, as she is equally likely to measure any Bell state, causing Bob's qubit to be random, i.e., qubit three carries no information[1].

6.2 RSP theory

First, we describe the general idea of RSP and give several examples. Although we will make reference to photon polarization qubits, the methods described here can be generalized to any physical qubit implementation. Consider the two-photon maximally entangled state: $|\Phi^+\rangle \equiv$

---

[1] One could also see this fact by noting that the incoherent sum of the possible outcomes for the third qubit is a completely mixed state.

$(|H_tH_{rp}\rangle + |V_tV_{rp}\rangle)/\sqrt{2} \equiv (|D_tD_{rp}\rangle + |A_tA_{rp}\rangle)/\sqrt{2}$, where the subscripts label the trigger and remotely prepared photons. Measurement of the trigger photon in the state $|D_t\rangle$ (i.e., detecting the trigger photon after a diagonal polarizer) prepares the other photon in the state $|D_{rp}\rangle$. To remotely prepare an arbitrary *pure* state $|\psi_{rp}(\theta,\phi)\rangle \equiv \cos\theta|D\rangle + \sin\theta e^{i\phi}|A\rangle$, Alice can act on the trigger photon with a quarter-wave plate (QWP) and a half-wave plate (HWP), such that the two-photon state $|\Phi^+\rangle \rightarrow (|\zeta_t(\theta,\phi)D_{rp}\rangle + |\zeta_t^\perp(\theta,\phi)A_{rp}\rangle)/\sqrt{2} \equiv (|D_t\psi_{rp}(\theta,\phi)\rangle + |A_t\psi_{rp}^\perp(\theta,\phi)\rangle)/\sqrt{2}$, where $|\zeta_t(\theta,\phi)\rangle \equiv \cos\theta|D\rangle - e^{-i\phi}\sin\theta|A\rangle$, and $\langle\zeta^\perp|\zeta\rangle = 0$. Thus, when the trigger qubit is projected into $\langle D|$ ($\langle A|$), the remotely prepared qubit is in the state $|\psi(\theta,\phi)\rangle$ ($|\psi^\perp(\theta,\phi)\rangle$). The 50% efficiency in this case can be improved to 100% if the state Alice is sending is constrained to lie on a single great circle on the Poincaré sphere: Bob simply performs the appropriate transformation on his photon $|\psi_b^\perp\rangle \rightarrow |\psi_b\rangle$ whenever Alice reports that she detects her photon in the state $|A\rangle$. This procedure does *not* work in general due to the impossibility of a universal NOT operation on arbitrary qubit states [80].

If instead the trigger polarizer is removed, the trigger photon is measured in a polarization-*insensitive* way, tracing over its polarization state[2]. This prepares the remaining photon in the completely mixed state (i.e., unpolarized), according to

$$\begin{aligned}
\rho_{rp} &= \langle D_t|\Phi^+\rangle\langle\Phi^+|D_t\rangle + \langle A_t|\Phi^+\rangle\langle\Phi^+|A_t\rangle && (6.2)\\
&= \frac{1}{2}\left(|D_{rp}\rangle\langle D_{rp}| + |A_{rp}\rangle\langle A_{rp}|\right) && (6.3)\\
&\Leftrightarrow \frac{1}{2}\begin{pmatrix} 1 & 0 \\ 0 & 1 \end{pmatrix}. && (6.4)
\end{aligned}$$

By using a *partial* polarizer to tune between the two limiting cases discussed above, we can control the *strength* of the polarization measurement on the trigger, and thus the resulting mixedness of the remotely prepared qubit (RPQ). Combined with the wave plates that allow us to prepare arbitrary pure states, the partial polarizer allows us to prepare completely arbitrary mixed states:

$$\rho_{rp}((\theta,\phi,\lambda)) = (1-\lambda)|\psi(\theta,\phi)\rangle\langle\psi(\theta,\phi)| + \frac{\lambda}{2}\mathbb{1}, \qquad (6.5)$$

---

[2] Suppose one knows that a system of two or more qubits is in a pure state; then measurement of the entropy of the subsystem can quantify entanglement of the full system [47].

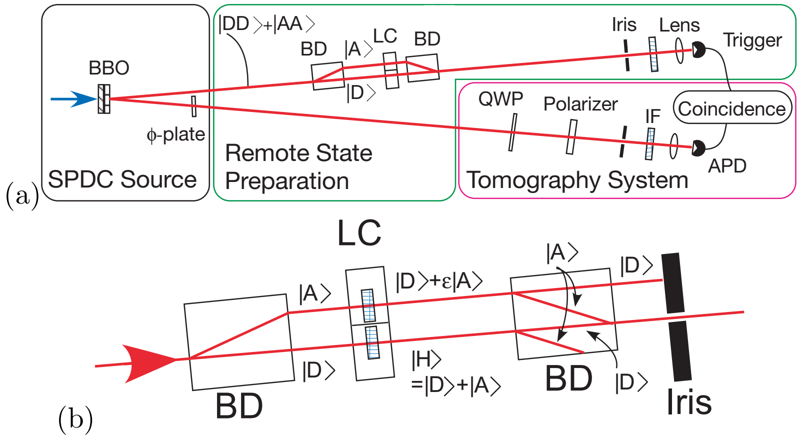

Figure 6.1: (a) Experimental arrangement to remotely prepare and measure single-photon states with variable mixedness. The BBO crystals are pumped and the ϕ-plate adjusted to create an initial entangled state $(|DD\rangle + |AA\rangle)/\sqrt{2}$. The trigger photon (upper arm) enters a partial polarizer (see closeup in (b)). Tomographies of the remotely prepared qubits are measured using a QWP and a polarizer. (b) Close-up view of the partial polarizer. It consists of a birefringent beam displacer (BD) that separates diagonal and antidiagonal polarization components, each of which passes through a separate liquid crystal (LC) element, with optic axis nominally oriented vertically. The liquid crystals rotate the polarization of each path component so that the second BD variably transmits T_D and T_A through a 1.3-mm iris (see text for details). For example, if the liquid crystal rotates the $|D\rangle$-polarized component to $|H\rangle$, an equal superposition of $|D\rangle$ and $|A\rangle$, then only the $|D\rangle$ component is transmitted through the iris, yielding $T_D = \frac{1}{2}$. In general, the liquid crystal can rotate the polarization so that there is an arbitrary ratio $|D\rangle + \epsilon|A\rangle$, giving $T_A = |\epsilon|^2$

where the value λ is determined by the partial polarizer.

6.3 RSP experiment

The experiment divides into three logical sections: entangled resource state creation (already discussed in section 3.1), measurement and detection of the trigger to remotely prepare a qubit, and tomography of the RPQ (as discussed in section 2.6)[3]. These three steps are highlighted by the different sections in a sketch of our experimental setup (Fig. 6.1). An initial tomography of the entangled resource state is taken by measuring 36 polarization correlations (such as $|HH\rangle$, $|HV\rangle$, $|DH\rangle$,..., etc.) from which a density matrix is calculated using a two-qubit maximum likelihood technique, as discussed in section 3.2 [29]. Once the entangled resource is so characterized, the remaining problem is to make an appropriate measurement on the trigger photon.

---

[3] Here we use all *six* of the cardinal states of the Poincaré sphere, instead of just four as previously discussed.

6.3.1 Mixed states and the partial polarizer

Single-photon mixed polarization states may be generated in a variety of ways [81]. Here, we demonstrate a novel method of control using partial measurement [82]. Using a *partial* polarizer, we can control the *strength* of the polarization measurement on the trigger, and thus the mixedness of the other qubit. Our partial polarizer's strength is governed by the transmission of two orthogonal polarization components, T_D and T_A, for diagonal and anti-diagonal polarizations, respectively, and normalized by $N \equiv 1/(T_D + T_A)$. Perfect transmission of one component coupled with zero transmission of the other realizes a perfect polarizer, set for the transmitted component. If $T_D = T_A$, then no polarization information is gained and the partial polarizer behaves as if no polarizer is present (though the overall amplitude may be reduced). The partial polarizer acts on the trigger, and when the trigger is used to condition RPQ, the latter becomes

$$\begin{aligned}
\rho_{rp}(T_D, T_A) &= N(T_D \langle D_t|\Phi^+\rangle\langle\Phi^+|D_t\rangle + T_A\langle A_t|\Phi^+\rangle\langle\Phi^+|A_t\rangle) \\
&= \tfrac{N}{2}(T_D|D_{rp}\rangle\langle D_{rp}| + T_A|A_{rp}\rangle\langle A_{rp}|) \\
&= \tfrac{1}{2}\begin{pmatrix} 1 & \alpha \\ \alpha & 1 \end{pmatrix} \equiv \rho_{rp}(\alpha),
\end{aligned} \tag{6.6}$$

where we have written the final density matrix in the $|H\rangle$, $|V\rangle$ basis and $\alpha \equiv N(T_D - T_A)$. We classify the mixedness of (6.6) using the linear entropy $S_L(\rho) = 2(1 - Tr(\rho^2))$, yielding

$$S_L(\rho_{rp}(\alpha)) = 1 - \alpha^2. \tag{6.7}$$

Although near-perfect entangled states have been experimentally achieved [36], this may be difficult in some cases. If instead of $|\Phi^+\rangle$, one starts with a non-ideal entangled state of the form

$$\rho_{\Phi^+}(\delta) = \frac{1}{2}\begin{pmatrix} 1 & 0 & 0 & 1-\delta \\ 0 & 0 & 0 & 0 \\ 0 & 0 & 0 & 0 \\ 1-\delta & 0 & 0 & 1 \end{pmatrix}, \tag{6.8}$$

where $|\delta| < 1$, then the remotely prepared state becomes

$$\rho_{rp}(\alpha, \delta) = \frac{1}{2} \begin{pmatrix} 1 & \alpha(1-\delta) \\ \alpha(1-\delta) & 1 \end{pmatrix}, \tag{6.9}$$

with linear entropy

$$S(\rho_{rp}(\alpha, \delta)) = 1 - \alpha^2(1-\delta)^2. \tag{6.10}$$

This model of a non-ideal entangled state is useful, as it is a close approximation to the entangled states that are often experimentally realized. Further, we will see that $1-\delta$ is precisely the two-photon fringe visibility that is typically measured to check the entanglement quality. This visibility is measured by setting polarizers in both arms of the experiment to $\langle D|$, measuring coincidence counts, and then rotating one of the polarizers to $\langle A|$ and coincidence counting for the same amount of time. For the ideal state $|\Phi^+\rangle$ there will be no $|DA\rangle$ or $|AD\rangle$ coincidences. However, if the initial state is not maximally entangled, e.g., as in $\rho_{\Phi^+}(\delta)$, then a background of $|DA\rangle$ and $|AD\rangle$ coincidences will be detected. The level of this background can be characterized by the fringe visibility when one polarizer is kept fixed at $\langle D|$ and the second polarizer is varied. For the state $\rho_{\Phi^+}(\delta)$, the maximum (minimum) coincidence rate will be observed when the second polarizer is along $\langle D|$ ($\langle A|$). The visibility is then given by

$$V(\rho_{\Phi^+}(\delta)) \equiv \frac{\langle DD|\rho_{\Phi^+}(\delta)|DD\rangle - \langle DA|\rho_{\Phi^+}(\delta)|DA\rangle}{\langle DD|\rho_{\Phi^+}(\delta)|DD\rangle + \langle DA|\rho_{\Phi^+}(\delta)|DA\rangle} = 1 - \delta. \tag{6.11}$$

For the results presented in Fig. 6.2, our entangled state had 95±2% visibility, i.e., δ=5±2%.

In the remote state preparation stage, the trigger photon passes through a partial polarizer (shown in Fig. 6.1), an iris, and is detected by an avalanche photodiode (APD). The partial polarizer is constructed using two birefringent (calcite) beam displacers (Thorlabs BD40), oriented such that, after passing through one such element, $|D\rangle$ polarized light is undeviated, while $|A\rangle$ polarized light is displaced by 4 mm. An identical element recombines these polarizations into the same mode (see Fig. 6.1). A multi-pixel liquid crystal (LC) is placed between the beam displacers, with a vertically oriented optic axis[4]. The $|D\rangle$ and $|A\rangle$ beams each goes through its own separately controlled LC

---

[4] Diagonal and antidiagonal were chosen as the basis for the partial polarizer for ease of mounting the liquid crystal.

pixel, which can rotate the polarization state according to the pixel's variable phase retardance. In the case of zero rotation, the second beam displacer transmits $|D\rangle$ polarized light undeviated as is the case without a LC, while undoing the displacement of $|A\rangle$ polarized light; consequently, both modes are recombined into the original spatial mode. If instead the LC rotates the polarized state, then only part of the beam (the original polarization component) is transmitted to the initial spatial mode; the new polarization component is directed by the second BD to a different spatial mode. At the output of the undeviated mode is an iris which screens any light that was not the same spatial mode as the light incident on the partial polarizer. In this way, the transmissions of the $|D\rangle$ and $|A\rangle$ polarization components may be arbitrarily adjusted. For example, suppose the LC rotated the polarization of light in the $|A\rangle$ spatial mode to $|H\rangle \equiv (|D\rangle + |A\rangle)/\sqrt{2}$; the second beam displacer will then deviate the $|A\rangle$ component so that it goes through the iris, while the $|D\rangle$-polarized component is transmitted undeviated and is blocked from detection by the iris. For this example, T_A=0.5. Thus, the iris selects a sub-ensemble of the trigger photons, corresponding to the transmission coefficients T_D and T_A, leaving the RPQ in the desired state.

For the rest of our discussion, the partial polarizer is treated as a black box, and is used to set the linear entropy by adjusting the relative transmissions T_D and T_A. In the ideal case, we saw that the linear entropy is a function of the *ratio* of the transmission probabilities; therefore, we fix T_D at its maximum and vary T_A to obtain the desired value of the RPQ's linear entropy:

$$T_A = T_D \frac{1-\delta-\sqrt{1-S}}{1-\delta+\sqrt{1-S}}, \tag{6.12}$$

where we have used the more general relation (6.10) to include the effects of non-maximal initial entanglement.

The transmitted trigger photon and the remotely prepared qubit photon are each detected using photon counting avalanche photodiodes, preceded by a 1.3-mm diameter collection iris and a 2-nm FWHM interference filter (IF) centered at 702 nm. Simultaneous detections within a 4.5-ns duration window are recorded as coincidences[5]. The classical communication from Alice to Bob is

---

In order for the liquid crystal to rotate polarization optimally, it must have an optic axis at 45° with respect to the polarization eigenbasis.

[5] We estimate the probability of two photons from different pairs being detected within the same coincidence window accidentally is 5×10^{-9} per coincidence window, so the accidental rate (e.g., between photons corresponding to different pairs or detector dark counts) is negligible and has not been subtracted from the data.

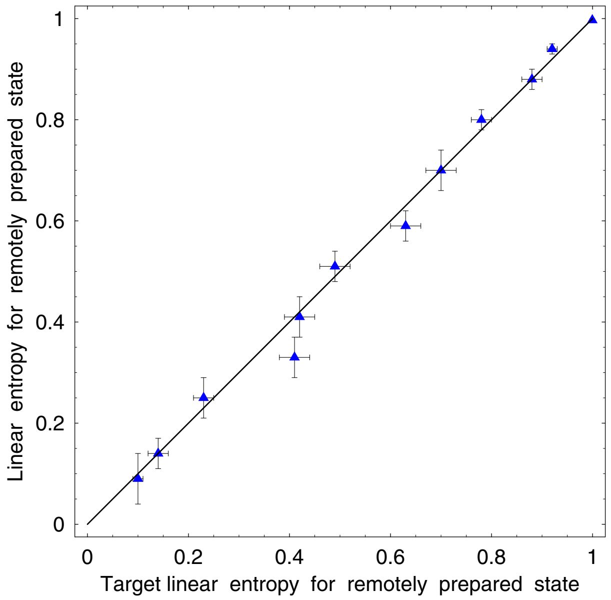

Figure 6.2: Linear entropy of remotely prepared states as described in Fig. 6.1 as a function of the target linear entropies. For comparison, the line y=x is also shown. The target linear entropy is estimated using equation (6.10) by inputting the experimentally measured values for T_D, T_A, and δ (see text).

implemented by counting the RPQs in coincidence (within a 4.5-ns window) with their triggering photons. The requirement for coincidence counting (which necessarily requires the (sub)luminal transfer of the APD signals to the coincidence circuitry) precludes all possibility of superluminal communication.

The linear entropy of our remotely prepared mixed states is shown in Fig. 6.2. The target linear entropy is estimated using equation (6.10) and plotted against the linear entropy calculated from the density matrix constructed from ∼2000 counts[6]. The error bars for the linear entropy as calculated from tomography are the result of a Monte Carlo simulation that takes simulates Poisson counting fluctuations. The target linear entropy error bars were calculated using the statistical error in the measurements of T_D, T_A, and δ, propagated through equation 6.10. We create a wide array of different entropy states in good agreement with our theoretical model, as evidenced by the distribution of the points along the line y=x as shown in Fig. 6.2. Note that unless one has a perfectly entangled resource, one cannot remotely prepare a completely pure state (linear entropy 0).

---

[6] This data appeared in reference [76].

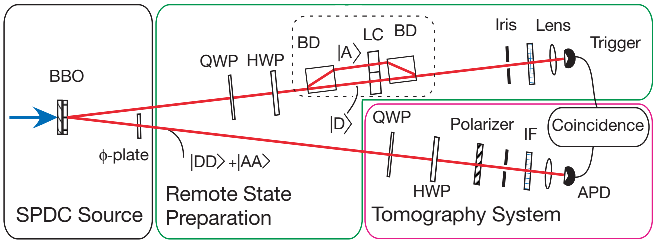

Figure 6.3: Experimental arrangement for arbitrary remote state preparation. BBO crystals produce the entangled state $(|DD\rangle + |AA\rangle)/\sqrt{2}$. The trigger photon is then *partially* projected into an arbitrary polarization state with a quarter-wave plate (QWP) and a half-wave plate (HWP) located before a partial polarizer shown in the dashed box. Conditional on detection of this photon, the sister photon is prepared in the desired state.

6.3.2 Arbitrary polarization projection

Next, we describe how the addition of a QWP and a HWP preceeding our partial polarizer enables arbitrary RSP. The trigger photon of the entangled pair is projected into an arbitrary polarization state with an adjustable strength polarizer to remotely prepare a qubit of the form (6.5). For perfect wave plates (i.e., the birefringent retardance is 180° for a HWP and 90° for a QWP), the precise wave plate angles can be readily calculated, similar to the case of *directly* preparing arbitrary states [21]. If the wave plate phases deviate much from the ideal (e.g., when using nominally 702-nm wave plates for 670-nm photons), the precise wave plate orientations can be found numerically. In this case, we maximize the fidelity between the state we wish to remotely prepare and the expected remotely prepared state calculated using the experimentally measured initial two-qubit entangled density matrix and the measured wave plate retardances.

After passing through the wave plates and the partial polarizer, the trigger photons pass through a 2.2-mm iris, an interference filter (discussed below), and a collection lens, which focuses them onto a photon-counting avalanche photodiode (Perkin-Elmer SPCM-AQR-13).

The final verification step is the tomographic measurement of the RPQ. Using the wave plates and polarizer of the tomography system shown in Fig. 6.3, the remotely prepared ensemble is projected into $\langle H|$, $\langle V|$, $\langle D|$ and $\langle A|$ states, as well as the left and right circular polarization states, $\langle L| \equiv \langle H| - i\langle V|$ and $\langle R| \equiv \langle H| + i\langle V|$, respectively. The results of this complete polarization analysis are converted to the closest physically valid density matrix using the maximum likelihood technique as discussed in section 2.6 [29].

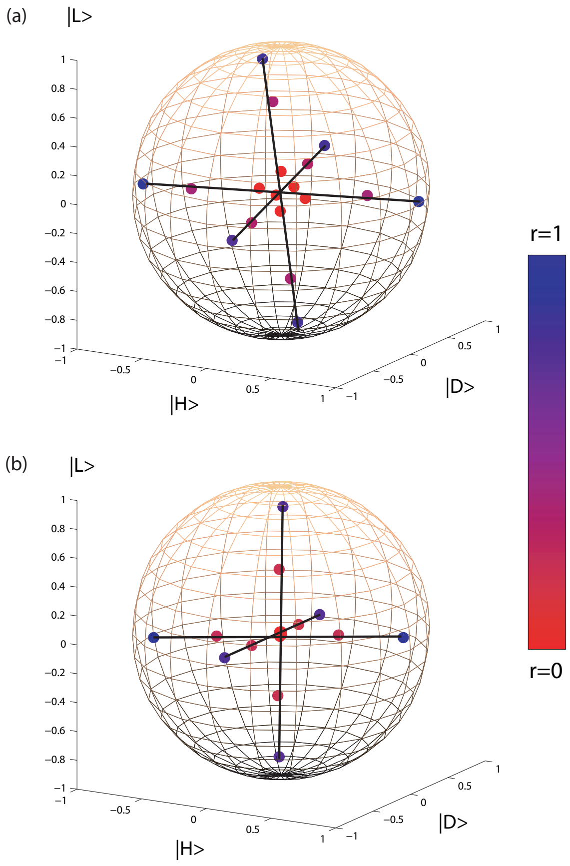

Figure 6.4: Remotely prepared states shown in the Poincaré sphere. (a) States remotely prepared at 702 nm using frequency *degenerate* entanglement. (b) States remotely prepared at 670 nm (using a 737-nm trigger). In either case, the distance of the remotely prepared state from the origin is indicated by its color: red → mixed, blue → pure. Lines are drawn along the data to guide the eye.

A summary of states remotely prepared in this way is shown in Fig. 6.4(a), along with a color bar indicating the distance of each RPQ from the center of the Poincaré sphere; the color corresponds to the state purity, from blue (pure) to red (mixed). We tested our ability to precisely remotely prepare arbitrary states by creating six states along each of three (nearly orthogonal) axes in the Poincaré sphere. We use the fidelity to quantify experimental agreement between the states we prepared and those we expected given the parameters of our system. The average fidelity for our data is 0.996, with all 18 states above 0.99.

The previous results were all taken using *degenerate* qubits, i.e., both trigger and RPQ were at ~702 nm, as defined by the cut of the BBO crystals, the position of the collection irises (corresponding to a 3°-opening angle with respect to the pump beam), and 2-nm bandpass filters in front of each detector[7]. To demonstrate the ability to remotely prepare qubits at other wavelengths, we additionally performed a similar set of measurements using *non*-degenerate entangled pairs: Detection of a trigger photon after a 5-nm bandpass filter at 737 nm corresponded to a RPQ at 670 nm. Note that all of the same physical resources, e.g., the crystals, the wave plates (by calculating wave plate phases away from design wavelengths) and the partial polarizer, were used at the different wavelengths. Results are shown in Fig. 6.4(b). The average fidelity was 0.996, with 17 of the 18 measured states above 0.99. In order to characterize the repeatability of our RSP techniques in Fig. 6.5, we show 10 repeated measurements of five 670-nm remotely prepared qubits of varying entropies. Here the average fidelity is 0.995, with all 50 states at or above 0.99. The flexibility to remotely prepare qubits at various wavelengths could be useful, e.g., for optimizing detector sensitivity, fiber or atmospheric transmission, or coupling to other quantum systems. One could even envision a sort of nonlocal wavelength division multiplexing scheme: using an adjustable filter before the trigger detector, arbitrary states could be remotely prepared at one of several detectors, each receiving a slightly different wavelength band.

6.3.3 Theoretical discussions

While a maximally entangled state resource enables the remote preparation of *any* state, it is important to consider the limits on the remotely preparable states when the two-qubit resource

---

[7] In principle, the trigger filter alone is enough to determine the wavelength of the RPQ; the second filter is used to reduce background counts, e.g., from fluorescence.

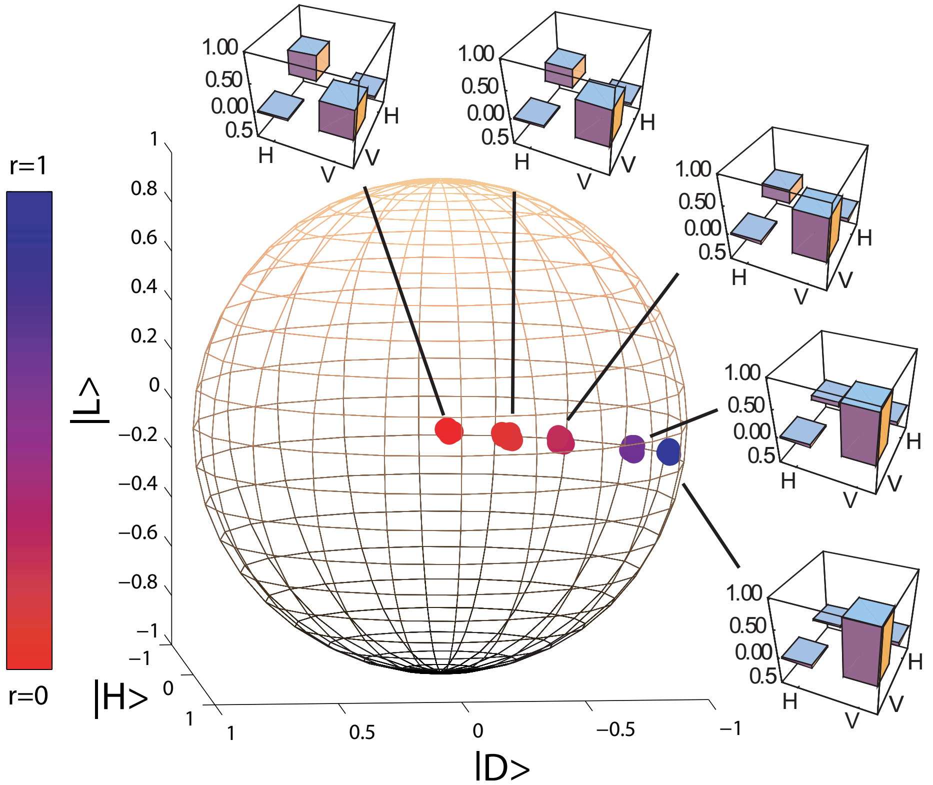

Figure 6.5: Additional states remotely prepared with nondegenerate entanglement. Shown are five different entropy states (nominally $[(1-\lambda)|V\rangle\langle V| + \frac{\lambda}{2}\mathbf{1}]$) which were measured 10 times each, showing that counting fluctuations change the plotted states negligibly. The color of the states plotted transitions from red (at the center of the sphere) for mixed (unpolarized) states to blue (at the surface of the sphere) for pure states. Also shown are one of the ten remotely prepared density matrices for each state. The average fidelity of produced states with expected states (given our wave plate, partial polarizer, and entangled resource parameters) is 0.995 for these 50 states, with no fidelities less than 0.99.

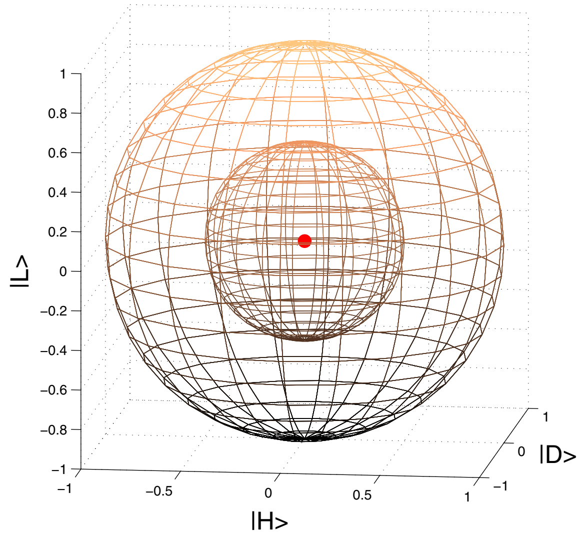

Figure 6.6: States remotely preparable via a Werner state $\rho_W(r=1/2)$. The unit sphere is Bob's Poincaré sphere, the origin being Bob's initial state, i.e., his state is completely mixed if Alice performs no polarization filtering. The smaller sphere (and its interior) represents states that Alice can remotely prepare.

is mixed or only partially entangled, as in practice all realizable states are of this type[8]. We consider the scenario that Bob simply keeps or discards his photon, based on transmission of a single classical bit from Alice. Furthermore, we restrict Alice to single-qubit operations, i.e., no collective manipulation of her qubits. This consideration is realistic, as efficient optical CNOT gates do not yet exist.

The most general operations Alice can perform on her qubit can be described by at most four local filters [66]:

$$\rho_A \to \sum_{i=1}^{4} p_i\, \mathcal{M}_i \rho_A \mathcal{M}_i^\dagger, \tag{6.13}$$

where $\sum_i p_i\, \mathcal{M}_i^\dagger \mathcal{M}_i \leq \mathbb{1}$, and each local filter $\mathcal{M}_i$ can be expressed in the singular-value decomposition

$$\mathcal{M} = V^\dagger \mathcal{D} U. \tag{6.14}$$

Here $\mathcal{D}$ is a non-negative, no-greater-than-unity diagonal matrix, and U and V are unitary matrices,

---

[8] This section is a slightly more general quantification of the way we calculate an expected remotely prepared state given the measured entangled resource and the wave plate phases. This generalization is due to T.-C. Wei [75].

not necessarily adjoint to each other.

Under the general operation (which can be non-trace preserving) performed by Alice, the initial joint two-qubit state ρ_{AB} becomes

$$\rho'_{AB} = \sum_{i=1}^{4} p_i \, \mathcal{M}_i \otimes \mathbb{1} \, \rho_{AB} \, \mathcal{M}_i^\dagger \otimes \mathbb{1}, \tag{6.15}$$

neglecting normalization, and Bob's qubit becomes $\rho'_B = \mathrm{Tr}_A \rho'_{AB}$. Thus, the most general states Alice can remotely prepare are mixtures of states which she can prepare from a single local filter. The states preparable from a single filter form a surface inside the Poincaré sphere, and all the states she can remotely prepare lie on or inside the convex hull of this surface. We now analyze the capability of a general local filter applied to RSP.

The decomposition of a general local filter (6.14) can be interpreted as a three-step procedure: (i) first, apply a local unitary transformation U, followed by (ii) a "Procrustean" operation [47, 57, 48, 52]

$$\mathcal{D} = \begin{pmatrix} a & 0 \\ 0 & b \end{pmatrix}, \tag{6.16}$$

with $0 \leq (a, b) \leq 1$, and lastly by (iii) another unitary transformation $V^\dagger$. The last step $V^\dagger$ has no effect on Bob's state, so it can be ignored in the analysis of RSP. With a suitable parameterization of U, e.g., $U = \cos\theta \mathbb{1} + i\hat{n} \cdot \vec{\sigma} \sin\theta$, where $\hat{n}$ is a unit vector and $\vec{\sigma}$ are the Pauli spin matrices, it is straightforward to analyze the states that can be remotely prepared by a single filter:

$$\rho_B = \mathrm{Tr}_A \Big[(\mathcal{D}U) \otimes \mathbb{1} \, \rho_{AB} \, (\mathcal{D}U)^\dagger \otimes \mathbb{1} \Big], \tag{6.17}$$

where ρ_{AB} is the initial shared two-qubit state (unnormalized).

To illustrate the results, we first consider the case where ρ_{AB} is a pure (but non-maximally) entangled state: $\sqrt{p}|00\rangle + \sqrt{1-p}|11\rangle$, assuming $p > 1/2$ without loss of generality. In fact, analysis of equation (6.17) reveals that with this state Alice can prepare *arbitrary* single-qubit states for Bob. She first uses Procrustean distillation $\mathcal{D}$ [47, 57, 48, 52], with $a = \sqrt{(1-p)/p}$ and $b = 1$, to obtain the perfect Bell state $|00\rangle + |11\rangle$ (though with probability < 1), with which she may remotely prepare arbitrary states as we have demonstrated experimentally.

As a rather different example, consider the starting state to be of the form [68]

$$\rho_{AB} = \frac{1}{4}\left(\mathbb{1}\otimes\mathbb{1} + t_1\,\sigma_x\otimes\sigma_x + t_2\,\sigma_y\otimes\sigma_y + t_3\,\sigma_z\otimes\sigma_z\right), \tag{6.18}$$

which has eigenvalues $\lambda_1 = (1-t_1+t_2+t_3)/4$, $\lambda_2 = (1+t_1-t_2+t_3)/4$, $\lambda_3 = (1+t_1+t_2-t_3)/4$, and $\lambda_4 = (1-t_1-t_2-t_3)/4$. This state, when described by (t_1, t_2, t_3), lies on the surface of or inside a tetrahedron, with the four vertices being $(-1,-1,-1)$, $(-1,1,1)$, $(1,-1,1)$, and $(1,1,-1)$. The state is entangled if any of the λ_i are greater than 1/2. Equation (6.18) describes a wide range of interesting resource states, as judicious choice of t_i changes the state from a maximally entangled pure state to a Werner state [64] to states with varying classical correlations. Again analyzing equation (6.17) we find that the states (in the Poincaré sphere) that Alice can remotely prepare lie on or inside the ellipsoid centered at the origin, with three axes of length $|t_1|$, $|t_2|$, and $|t_3|$. To remotely prepare states on the surface of the ellipsoid, Alice simply rotates her qubit via $i\hat{n}\cdot\vec{\sigma}$, followed by projection onto $|0\rangle$. As she varies the rotation axis $\hat{n} = (\sin\alpha\cos\beta, \sin\alpha\sin\beta, \cos\alpha)$, Bob's states will then follow the corresponding trace $(t_1\sin 2\alpha\cos\beta, t_2\sin 2\alpha\sin\beta, t_3\cos 2\alpha)$ on the ellipsoid. To obtain states inside the ellipsoid, the projection onto $|0\rangle$ is replaced by the more general partial projection (equation (6.16)).

We have seen that pure-state entanglement allows remote preparation of arbitrary states. However, pure-state entanglement may not be *required* to remotely prepare some states. Consider that the tetrahedron state (6.18) has purity

$$P_{AB} = \mathrm{Tr}\rho_{AB}^2 = \frac{1}{4}(1+t_1^2+t_2^2+t_3^2), \tag{6.19}$$

and is unentangled if (t_1, t_2, t_3) lies inside the octahedron embedded in the tetrahedron [68]. The maximum purity of the states Alice can remotely prepare via the tetrahedron state is

$$\max P_B = \frac{1}{2}(1+\max(t_1^2, t_2^2, t_3^2)). \tag{6.20}$$

Interestingly, there appears to be no general requirement for entanglement in the two-qubit resource to be able to remotely prepare a one-qubit state of arbitrary purity. Consider the classically correlated state $\rho_{cc} = \frac{1}{2}(|00\rangle\langle 00| + |11\rangle\langle 11|)$ (i.e., $t_1 = t_2 = 0$ and $t_3 = 1$). This classically correlated two-qubit state can be used to remotely prepare any state of the form $\cos^2\theta|0\rangle\langle 0| + \sin^2\theta|1\rangle\langle 1|$, possessing any purity. For unentangled resources where the classical correlations are less than in ρ_{cc}, Alice can only remotely prepare states near the origin of the Poincaré sphere.

6.4 Other ways to remotely prepare mixed states

While we have concentrated on control of the mixedness of single-photon polarization states using partial measurement [82], there are at least two additional procedures that can be used. The first is by using the method we have employed to create mixedness in single- and two-qubit states, i.e., using quartz decoherers. Essentially, one uses the scheme in Section 2.5 for creating arbitrary single-qubits but reverses the order of elements. In this case, the trigger photon is projected into a polarization state using a QWP, HWP, decoherer, a HWP and a polarizer[9]. The second method relies on using *non*maximally entangled states as resource pairs, and completely tracing over one member of the pair to yield partially mixed states. For example, if the nonmaximally entangled state is of the form $|\phi(\theta)\rangle = \cos\theta|H_t H_{rp}\rangle + \sin\theta|V_t V_{rp}\rangle$, then tracing over the trigger qubit yields

$$\begin{aligned}
\rho_{rp} &= \langle H_t|\phi(\theta)\rangle\langle\phi(\theta)|H_t\rangle + \langle V_t|\phi(\theta)\rangle\langle\phi(\theta)|V_t\rangle \\
&= \cos^2\theta|H_{rp}\rangle\langle H_{rp}| + \sin^2\theta|V_{rp}\rangle\langle V_{rp}| \\
&= \frac{1}{2}\begin{pmatrix} \cos^2\theta & 0 \\ 0 & \sin^2\theta \end{pmatrix}. \qquad (6.21)
\end{aligned}$$

Creating mixed states directly as in chapter 2 and remotely creating mixed states by tracing over a member of a nonmaximally entangled pair are conceptually different. In the former we trace over a degree of freedom carried by the same particle, while in the latter the tracing is over an entirely separate particle. However, in the next chapter, we will see that when we measure geometric phase using mixed states prepared with either of the techniques, the results are the same. While this is not proof that the two types of decoherence are identical, it does indicate that at least in some cases, both methods give states that are genuinely "mixed".

---

[9] This approach was implemented by Xiang et al. [83]. We note that they remotely prepare some single-qubit states using a Werner-state resource in addition to a near maximally entangled resource.

In this chapter, we have demonstrated the first arbitrary remote state preparation of qubits, preparing a broad range of states spanning the Poincaré sphere. The experimental methods employed may facilitate state control in linear optics feedforward quantum computation [84, 85]. Moreover, by varying the acceptance wavelength of the trigger photon (using a nondegenerate entangled source) we can also control the wavelength of the remotely prepared qubit. Such a capability may assist in the preparation of states at wavelengths more optimal for other quantum communication protocols, e.g., quantum cryptography. Finally, we have derived bounds on the single-qubit states that may be remotely prepared using certain two-qubit resource states.

Chapter 7

Mixed-state geometric phase

7.1 Mixed-state geometric phase

More importantly than allowing us to compare mixed states prepared in different ways, mixed state geometric phase is itself interesting. When a pure quantum state undergoes a cyclic progression, besides acquiring the dynamical phase that depends on the evolution Hamiltonian, it retains memory of its motion in the form of a purely geometric phase factor, i.e., the acquired phase does not depend on the time, or even the precise trajectory of evolution, but only the net solid angle subtended by the evolution of the state vector [86, 87]. This pure-state geometric phase has been experimentally demonstrated in various systems such as single-photon interferometry [88], two-photon interferometry [89, 90], and NMR [91]. Recently, it has been proposed that fault-tolerant quantum computation may be performed using geometric phases [92, 93, 94, 95], since they are independent of the speed of the quantum gate and depend only on the area of the path the state takes in Hilbert space. As states inevitably suffer decoherence, it is important to investigate the resilience of geometric phases to such effects. Some properties of geometric phases for mixed states, proposed by Sjöqvist et al. [96], have been recently investigated in NMR [97]. Here, we describe an experimental study of geometric phase for mixed quantum states with single photons[1]. The exquisite control achievable with optical qubits allows us to precisely map the behavior of the phase for various amounts of mixture, yielding experimental data in very good agreement with theoretical predictions. These results are encouraging, in light of recent work on scalable linear optics quantum computation [99, 100, 101, 102].

---

[1] The research in this section was presented in reference [98].

In order to measure a geometric phase, the dynamical phase has to be eliminated (or at least accounted for). One can parallel transport the state vector in order to ensure that the dynamical phase is zero at all times. The parallel transport condition[2] for a particular state vector $|\Psi(t)\rangle$ is $\langle\Psi(t)|\dot{\Psi}(t)\rangle = 0$, which implies that there is no change in phase when $|\Psi(t)\rangle$ evolves to $|\Psi(t+dt)\rangle$, for some infinitesimal change in time t. However, even though the state does not acquire a phase locally, it can acquire a phase globally after completing a cyclic evolution. This global phase is equal to the geometric phase, and has its origin in the underlying curvature of the state space. It is therefore resilient to certain dynamical perturbations of the evolution, e.g., it is independent of the speed (or acceleration) of evolution.

Uhlmann [103] described mixed state geometric phases where the parallel transport of a mixed state is defined in a larger state space which is a "purification" of the mixed state[3] [104]. In this approach the number of parallel transport conditions for a known $N \times N$ density matrix is N^2, but its time evolution operator U has only N free variables. This approach can only be described in a larger Hilbert space with the system and an attached ancilla evolving together in a parallel manner [105].

Sjöqvist et al. defined a mixed-state geometric phase requiring no auxiliary subsystem [96, 105]. This phase can be investigated using an interferometer in which a mixed state is parallel transported by a unitary operator in one arm; the output then interferes with the other arm, which has no geometric phase. The parallel transport of a mixed state $\rho = \sum_{k=1}^{N} p_k |k\rangle\langle k|$ is given by $\langle k(t)|\dot{k}(t)\rangle = 0,\ \forall\ k$, i.e., each eigenvector of the initial density matrix is parallel transported by the unitary operator. The resulting N conditions uniquely determine the unitary operator and ensure the gauge invariance of the geometric phase. A consequence is that each eigenvector acquires a geometric phase γ_k, and an associated interference visibility v_k. The total mixed-state geometric phase factor is the average of the individual phase factors, weighted by p_k:

$$v e^{i\gamma_g} = \sum_k p_k v_k e^{i\gamma_k}. \tag{7.1}$$

---

[2] This condition requires that the state vector amplitude does not change and that the there is no rotation about its instantaneous normal vector.

[3] If there exists a state $|R\rangle$ of some reference system R such that a system M in a mixed state ρ_M can be written as a pure state $|MA\rangle$ in a larger, joint system, then R is said to be a "purification" of ρ_M [104].

Recall that the polarization mixed state of a single photon can be represented by equation (2.8), i.e., $\rho = \frac{1}{2}(\mathbb{1} + \vec{r} \cdot \vec{\sigma})$. It represents a mixture of its two eigenvectors with eigenvalues $\frac{1}{2}(1 \pm r)$. The length of the Bloch vector r gives the measure of the purity of the state, from completely mixed ($r = 0$) to pure ($r = 1$). For photons of purity r, equation (7.1) becomes

$$ve^{i\gamma_g} = \cos(\Omega/2) - ir\sin(\Omega/2), \tag{7.2}$$

where Ω is the solid angle enclosed by the trajectory of one of the eigenvectors on the Bloch sphere with corresponding geometric phase $\Omega/2$ (the other eigenvector traverses the same trajectory, but in the opposite direction, leading to a geometric phase $-\Omega/2$). From equation (7.2) we obtain the visibility and geometric phase, respectively, [96]

$$v = \sqrt{\cos^2(\Omega/2) + r^2 \sin^2(\Omega/2)}, \qquad \text{and} \tag{7.3}$$

$$\gamma_g = -\arctan\left(r\tan(\Omega/2)\right). \tag{7.4}$$

Here, γ_g is measured in an interferometer by plotting the output intensity versus an applied dynamical phase shift in one interferometer arm. For pure states, the geometric phase given by (7.4) reduces to half the solid angle[4] ($\Omega/2$).

In our experiment, single-photon states are conditionally produced by detecting one member of a photon pair produced in spontaneous parametric downconversion (SPDC) [22] (we also took data using coherent states from a diode laser). Specifically, pairs of photons at 670 nm and the conjugate wavelength 737 nm are produced via SPDC by pumping Type-I phase matched BBO with an Ar^+ laser at $\lambda = 351$ nm. By conditioning on detection of a 737-nm "trigger" photon (with an avalanche photodiode after a 5-nm FWHM interference filter at 737 nm), the quantum state of the conjugate mode is prepared into an excellent approximation of a single-photon Fock state at 670 nm [88, 22], also with wavelength spread $\delta\lambda \sim 5$ nm. As shown in Fig. 7.1, the 670-nm photons are coupled into a single-mode optical fiber to guarantee a single spatial mode input for the subsequent interferometer. A fiber polarization controller is used to cancel any polarization

---

[4] The geometric phase is half the solid angle even though photons are spin-one particles because a 180° rotation returns a beginning polarization state to itself. This is ultimately a consequence of the massless nature of the photon.

transformations in the fiber.

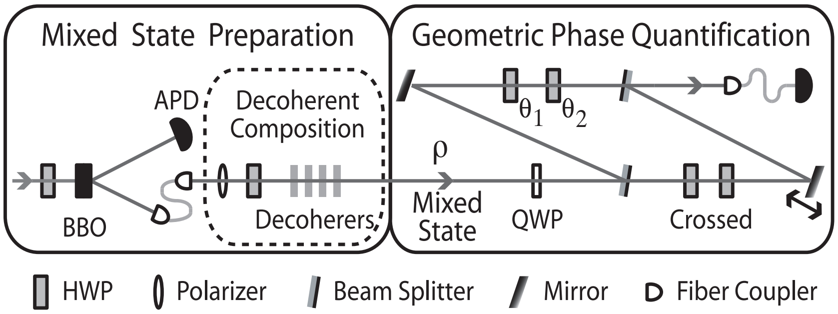

Figure 7.1: Mixed state generation and interferometer to measure geometric phase. Mixed states are prepared via two methods: 1) tracing over the polarization of one photon of a nonmaximally entangled polarization state and, 2) using an initial pure polarization state with birefringent decoherers that couple polarization to photon arrival time (see dashed box). In the latter case, tracing over this time prepares a mixed state. Half-wave plates at θ_1 and θ_2 generate geometric phase but do not otherwise alter the transmitted polarization state. Two crossed wave plates in the lower interferometer arm give no geometric phase, but compensate the optical path difference between the arms to achieve high visibility. The interferometer shape minimizes unwanted polarization changes arising from non-normal mirror and beam splitter reflections.

The mixedness of the 670-nm photons is set via two different methods (as proposed in [81]). Following the methods of chapter 2, we directly prepare mixed states. Specifically, we use thick birefringent decoherers that couple the single photon's polarization to its arrival time relative to the trigger [27][5]. Tracing over the timing information during state detection erases coherence between these distinguishable states; this is equivalent to irreversible decoherence [81]. To guarantee a pure fiducial state for this method of generating mixed states, a horizontal polarizer is placed after the polarization controller, followed by a half-wave plate, and finally the decoherers (four pieces of quartz of ∼3 cm total thickness). By rotating the HWP, the state can be prepared in an arbitrary superposition $\cos\theta|H\rangle + \sin\theta|V\rangle$. The light is then sent through the decoherers, effectively erasing the off-diagonal terms in the density matrix, resulting in purity $r = |\cos 2\theta|$. In our experiment, the eigenstates of the net geometric phase *operator* are circular polarizations; therefore, before entering the interferometer, the quantum state is rotated with a quarter-wave plate (QWP) into a mixture

---

[5] The coherent states from the diode laser is similarly mixed, using an unbalanced polarizing interferometer to separate $|H\rangle$ and $|V\rangle$ by more than the ∼1 m diode laser coherence length.

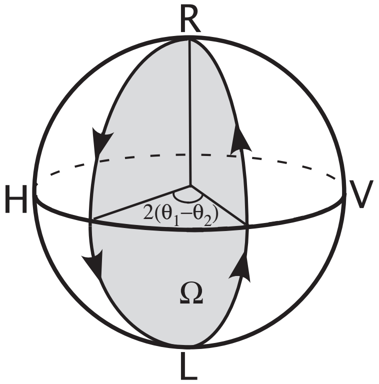

Figure 7.2: The solid angle Ω enclosed by the cyclic path of one eigenvector of the density matrix. The other eigenvector traces the same path but in the opposite direction, thus enclosing the solid angle $-\Omega$. Ω can be varied by adjusting $\theta_1 - \theta_2$, the relative angle between the optic axes of the two HWPs in the geometric phase arm of the interferometer.

of left ($|L\rangle \equiv (|H\rangle + i|V\rangle)/\sqrt{2}$) and right ($|R\rangle \equiv (|H\rangle - i|V\rangle)/\sqrt{2}$) circular polarized light[6].

Our second method to produce mixed-polarization single-photon states, a version of remote state preparation [72], is to trace over one of the photons of a pair initially in a nonmaximally entangled polarization state, $\cos\theta|HH\rangle + \sin\theta|VV\rangle$, using the two-crystal scheme described in chapter 3 [36]. In this case, the first position polarization label corresponds to the trigger photon (at 737 nm) while the second corresponds to its partner (at 670 nm). A polarization-insensitive measurement of the trigger photon prepares the partner in the polarization mixed state (as in equation 6.21)

$$\rho_{670nm} \;=\; \cos^2\theta_p|H\rangle\langle H| \;+\; \sin^2\theta_p|V\rangle\langle V|, \tag{7.5}$$

with purity $r = |\cos 2\theta_p|$. ρ_{670nm} is then transported over the single-mode fiber (still with the polarization controller so the fiber does not alter the state). As before, a QWP is used to rotate the photon's polarization state to a mixture of $|R\rangle$ and $|L\rangle$ before entering the interferometer.

After either mixed state preparation, the photon is sent into a Mach-Zehnder interferometer (Fig. 7.1). In the upper arm, the Bloch vector $\vec{r}$ is evolved unitarily using two half-wave plates with optic axes at θ_1 and θ_2, respectively. The evolution can be illustrated (Fig. 7.2) with one of

---

[6] We characterized our beam splitters with a laser at 670 nm using right and left circularly polarized light. We measured the reflected and transmitted state resulting from incident $|R\rangle$ and $|L\rangle$ polarizations. For both beam splitters, the fidelity of the output state with the expected eigenstate was very high (on average 0.995 with a standard deviation spread of 0.009). This behavior is expected because of the small angle of incidence on the beam splitters. Thus, we believe our assumption of circular polarization eigenstates is valid to within the experimental uncertainties of our results.

the eigenvectors of the density matrix, e.g., $|R\rangle$, traveling along two geodesics going from $|R\rangle$ to $|L\rangle$ and back. The trajectory encloses a solid angle $\Omega = 4(\theta_1 - \theta_2)$. The other eigenvector takes the same path but in the opposite direction, and therefore encloses the solid angle $-\Omega$. As there is an extra free parameter, without loss of generality, we can fix $\theta_2 = 0$, since Ω depends only on $\theta_1 - \theta_2$. For mixed states, the length of r is reduced, but the same solid angle is subtended. The resulting evolution fulfills the parallel transport conditions for mixed states, and the induced geometric phase is obtained by substituting $\Omega/2 = 2\theta_1$ into equations (7.3) and (7.4). A motorized rotation stage is used to set θ_1 (to within 0.01°) and thus, the geometric phase[7].

To measure γ_g and v, we apply a dynamical phase shift in the lower interferometer arm and measure the resulting interference pattern both with a geometric phase (for several settings of θ_1) and without ($\theta_1 = 0$). The dynamical phase shift is produced with a piezoelectric transducer (PZT) on the translation stage on which the lower path mirror is mounted. By adjusting the voltage across the PZT, the length difference (ΔL) between the arms is varied, giving the probability for the photon to exit the interferometer to the detector as

$$P(\Delta L) = \left(1 + \nu \cos\left(2\pi \Delta L/\lambda - \gamma_g\right)\right)/2. \tag{7.6}$$

Photons are detected using an avalanche photodiode. To conditionally prepare a single-photon Fock state with the desired bandwidth, we count only coincident detections (within a 4.5-ns timing window) with the trigger detector. We estimate the probability of two photons being present accidentally during a given coincidence window is 3×10^{-6} for the decoherer method (using a 4-mm thick BBO crystal) and 8×10^{-9} for the entanglement method (using two 0.6-mm crystals). Thus the "accidental" coincidence rate (e.g., between photons corresponding to different pairs, or from detector dark counts) is negligible, and has *not* been subtracted from the data.

Data is taken by varying the PZT voltage from 30 to 70 volts, in 5 volt steps, giving slightly more than one period of the interference pattern[8]. At each voltage, data is accumulated for 2 s (decoherer method) or 6 s (traced-over entangled state method). We plot the number of coincidences

---

[7] The adjustable wave plate must not be wedged, or the path overlap will be ruined when the wave plate is rotated.

[8] We did measure larger voltage ranges. However, over the larger ranges, the spread in the extracted parameters was larger due to interferometer drift. Thus, shorter measurements gave more consistent extracted visibilities over several repetitions.

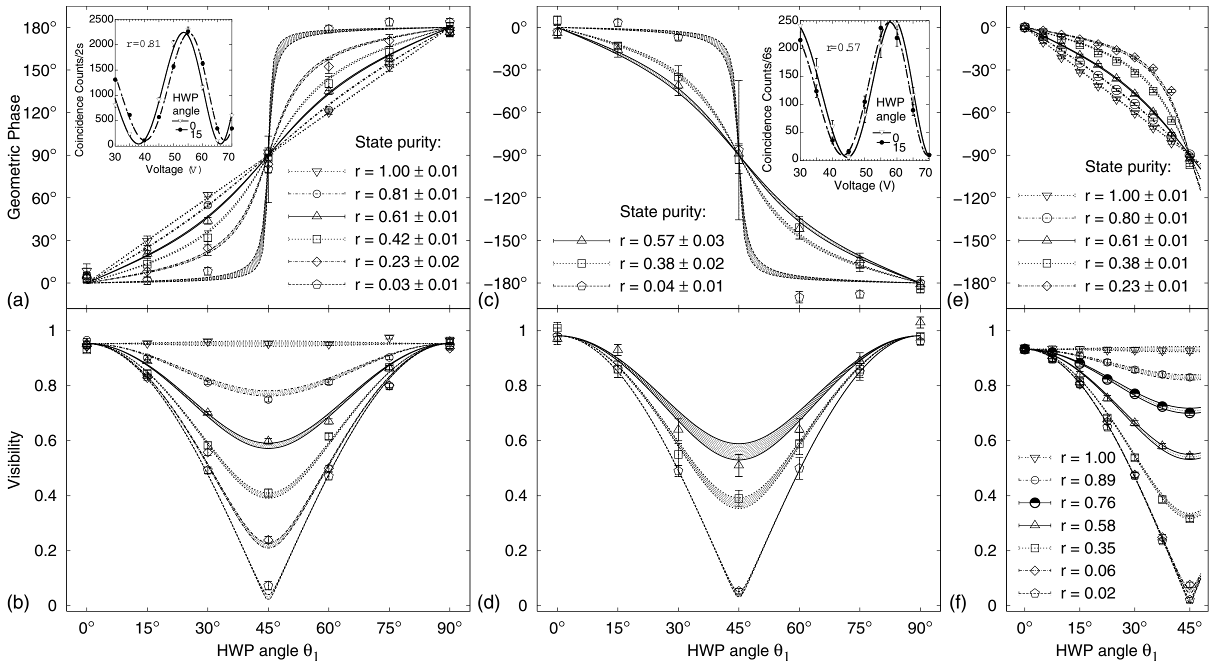

Figure 7.3: The mixed state geometric phases and visibilities as a function of the half-wave plate angle θ_1. (a)-(b) The photons in the mixed polarization state were produced with decohering quartz elements (see text). (c)-(d) The mixed polarization state photons were produced by tracing over one photon in a nonmaximally entangled state. (e)-(f) The classical laser was decohered with an imbalanced polarizing interferometer. The error bars are derived from the fit of the raw data to equation 7.6. The error in the theoretical curves shown results from uncertainties in the determination of r, due to photon counting statistics (or intensity fluctuations for (e) and (f)). The visibility theory curves are normalized to the average visibility when $\theta_1 = 0$: 95% for (b), 98% for (d), and 93% for (e). The slightly imperfect visibility is largely due to imperfect interferometer mode-matching. Typical data is shown inset in (a) ($\theta_1 = 0°$ and $\theta_1 = 15°$ for $r = 0.81$) and (c) ($\theta_1 = 0°$ and $\theta_1 = 15°$ and $r = 0.57$). Note: In (a) and (c) the curves are flipped along the x axis: in the first setup the input states possessed larger right-circular polarization eigenvalues, while in the second setup, left-circular polarization was dominant (The $r = 0.04$ initial state was prepared unintentionally more right circular polarized than left, opposite of the initial states for the $r = 0.38$ and $r = 0.57$ trials. Therefore, for ease of comparison with these curves, the $r = 0.04$ data curve is displayed flipped about the horizontal.).

as a function of PZT voltage, and then fit a curve to extract the phase and visibility information for each HWP setting[9]. To calculate the phase difference due to the geometric phase, we relate the data for each HWP setting θ_1 to the reference data with $\theta_1 = 0$ (see inset in Figs. 3(a) and 3(c))[10].

The experimental data are plotted in Figs. 7.3(a)-7.3(f), along with theoretical curves based on the measured purity of the photons. To determine the purity, we measure the $|H\rangle$ and $|V\rangle$ components of the mixed state before the last QWP in front of the interferometer. Figs. 7.3(a)-(b) show the data for the geometric phase and the visibility, respectively, for the experiment where the single photons are decohered with thick birefringent quartz. Figs. 7.3(c)-7.3(d) show the corresponding data when the mixture is due to entanglement to the trigger photon. Figs. 7.3(e)-7.3(f) show results from the coherent state[11], indicating that the data clearly fits the theoretical prediction and demonstrates that the single-photon geometric phase survives the correspondence principle classical limit [88]. Two of the geometric phase plots, Fig. 7.3(a) and Fig. 7.3(c), are flipped along the x axis: in the first setup the input states possessed larger right-circular polarization eigenvalues, while in the second setup, left-circular polarization was dominant.

Figure 7.3's error bars arise from the fitting program's uncertainty estimate of the phase and visibility from the raw fringes. This error is consistent with the standard error obtained from repeating measurements four times to calculate the spread in the geometric phase and visibility. We quantify how well the data fits the theory using a weighted reduced χ^2-analysis [12]. The Chi-squared analysis is weighted by the reciprocal of the standard deviation squared. For the determination of geometric phase, this analysis gives average values of 0.98 (with the individual curves' values ranging between 0.6 and 1.2) and 1.14 (ranging between 0.6 and 2.0) for the decoherer and entangled state preparations, respectively. In contrast, if we compare each of the data sets for the entangled state preparations with the "wrong" theory predictions, we obtain an average of the

---

[9] Because the voltage applied to the PZT creates a nonlinear increase in the path length, we fit our data to a sinusoid with nonlinear dependence on the argument. The PZT nonlinear fit parameters were determined by measuring dynamical phase fringes in our interferometer. We characterized these parameters using an empty interferometer by measuring interference fringes produced when sweeping the PZT voltage through the same range at the same rate as we did while taking the data collected in Fig. 7.3. This measurement was done many times, and the average nonlinear fit parameters were used as constants in the function that was fit to give the results in Fig. 7.3.

[10] To reduce the effect of dynamical phase drift, the reference data is taken both before and after each geometric phase-generating HWP setting. The data for each specific wave plate setting is used to calculate the geometric phase relative to both the initial and final reference data; the reported result is the average of the two calculations.

[11] These measurements were taken by Daryl Achilles.

[12] The χ^2-analysis was carried out by Julio Barreiro.

reduced Chi-squared values of 3.8, i.e., quite poor agreement; this analysis indicates that the data in Fig. 3c is not equally consistent with any of the theoretical curves. The reduced Chi-square values for the visibilities are similar, with average values of 1.36 (ranging from 0.9 to 2.3) and 0.94 (ranging from 0.6 to 1.3) for the decoherer and entangled state data, respectively. As a final check, in order to determine what purity best represents each data set, we calculated a curve fit with the purity (r) as a free parameter. This estimated purity agrees with the measured purity for each curve within the uncertainty. Here we also weighted the Chi-squared of the curve fit by the reciprocal of the standard deviation squared.

We report a measurement of geometric phases for single photons prepared in various polarization mixed states, created using two different methods. Specifically, we report a novel way of creating decohered one-qubit states from entangled two-qubit states, a simple version of remote state preparation. Both ways of creating mixed states give geometric phase and visibility data in very good agreement with the theoretical predictions even though the decoherence method is conceptually different. Our results indicate that we have a good measure of the geometric phase for mixed states, which in future work will enable the estimation of fault tolerance in geometric quantum computation with linear optical elements. We also anticipate further experiments on non-unitarily evolved mixed states [105] and non-Abelian geometric phases [106], to ultimately realize a universal set of geometric gates for quantum computation [107].

Chapter 8

Towards a deterministic single-photon source

So far we have discussed several resources for quantum communication and computation, mostly concerned with polarization state creation and manipulation. While sometimes the precise encoding of polarization states on single photons is enough to implement a quantum communication protocol such as RSP, there can be additional characteristics that are required. One such requirement is that the qubit be carried on only *one* photon. The use of single-photon states helps to ensure that quantum cryptography is secure because an eavesdropper cannot copy the quantum information without adding errors that alert the cryptographers to discard the compromised secret key [108][1]. Another more challenging requirement is that the single photons are produced at a particular time, i.e., “on-demand”. Such a single photon source (SPS) seems to be an essential requirement for linear optics quantum computing. While the KLM linear optics quantum computing approach assumes the availability of SPSs [99], the cluster state approach assumes the availability of or the ability to create many-photon entangled states [84]. The current state of the art is a five-photon entangled state produced at the rate of one every minute [110][2]. However, the availability of single-photon sources should not only increase the efficiency of entangled-state creation, but also enable the creation of even larger entangled states.

As SPSs are important for quantum information, there have been many approaches to create them. These include quantum dots [111], nitrogen vacancies in a diamond lattice [112], and single atoms or ions coupled to high-finesse cavity [113]. One disadvantage of these approaches is that

---

[1] Of course, *entangled* photon pairs can be used for even greater security benefits [109].

[2] The difficulty here is much the same as it is for multi-photon entanglement concentration, as discussed in Chapter 4.

it is very difficult to couple the emitted photon into a useful single spatial mode. As a result, the maximum out-coupling of a single photon is generally lower than 40% [114].

In this chapter we describe a different approach to realizing single-photon sources, via the process of spontaneous parametric downconversion. The basic idea is to conditionally prepare single photons by measuring one member of a spontaneously emitted photon pair, as was shown by Hong and Mandel [22], but to store the conditionally prepared photon until a predetermined time when it would be "deterministically" switched out of storage. The first experiment of this sort was carried out by Pittman, Jacobs and Franson [115].

The output of SPDC is effectively in a Poisson number distribution[3], so that if the probability of creating a pair of photons is high in a given time interval, there is also an high probability of creating multiple pairs of photons[4]. Our approach attempts to improve upon this by decreasing the power of the pump pulse to decrease the possibility of multiple pair generation. By decreasing the pump power, we also decrease the likelihood of creating exactly one photon pair, which would obviously degrade the performance of the source. To mitigate this effect, we *recycle* the pump pulse in a cavity so that it has many chances to produce exactly one photon pair in the nonlinear crystal [76]. Thus we can decrease the possibility of multiple-pair events while maintaining a high probability of producing a single pair. This approach has the further advantage that if more than one pair is generated in a given pass through the crystal, by detecting two or more photons in the trigger mode, we can veto that cycle, thereby reducing the chance of outputting of multiple photons. Finally, an extension of this approach allows a partial mitigation of the effects of storage-cavity loss, as it is possible to replace an "attenuated" photon–generated during an early pump cycle–with a newly created photon from a later cycle of the same pump pulse.

In addition to being a useful tool, the construction of a single-photon source allows us to study many of the challenges central to other quantum information technologies, including the need for low-loss optical storage, switching, and detection and fast feed-forward control.

---

[3] In fact, due to weak stimulated emission effects, the pair emission is governed by a *thermal* distribution, as was recently demonstrated [116]. However, the effect of this photon "bunching" is negligible under typical experimental conditions.

[4] Multiple pairs of photons would increase the likelihood of having more than one photon in the output of the SPS, making the source less suitable and perhaps even unacceptable, e.g., for quantum cryptography.

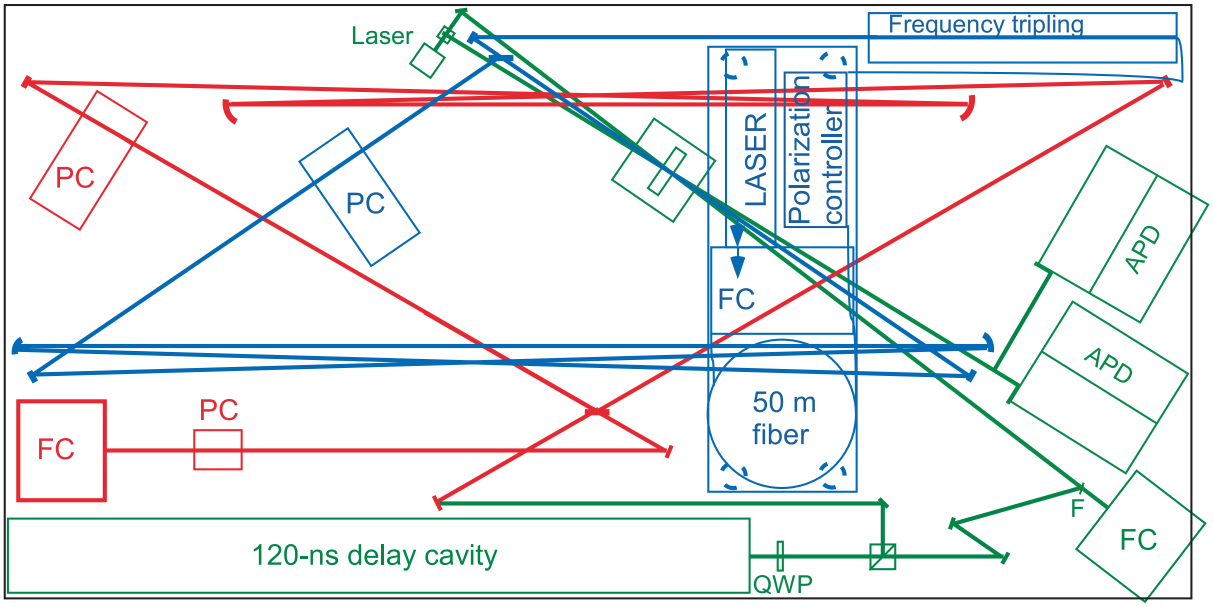

Figure 8.1: Scale drawing of single-photon source on a 8' x 4' (∼1.2 x 2.4 m) optical table.

8.1 Experimental design

In this section we will describe the idea and experimental design of our single-photon source, including the performance requirements of the optical, electro-optical, and high-speed electronic components needed to implement it. Fig. 8.1 shows the three main sections of the experiment–the pump laser and its recycling cavity; the downconversion crystal, trigger detector, and fixed optical delay; and the switchable storage cavity–color-coded blue, green and red, respectively. In the next three subsections, we discuss the rational behind our design and give available experimental details.

8.1.1 Pump laser and cavity

The process begins when a 1064-nm ∼0.5-ns long pulse leaves an Nd:YAG laser (JDS Uniphase NP-10620-110, 50-mW average power). At nearly the same time that the optical laser pulse is emitted (within a few ns), an electrical heralding pulse is also produced by the laser electronics. The optical pulse is fiber-coupled into a single-mode optical fiber (Thorlabs SM980-5.8-125), with a coupling efficiency ∼30%. The fiber is 50 m long, giving a ∼240-ns optical delay. The propagation loss in this fiber is negligible: the specified maximum fiber attenuation (3dB/km at 980 nm) predicts an attenuation of less than 3%. As indicated in Fig. 8.2, we place the fiber-coupling system on an

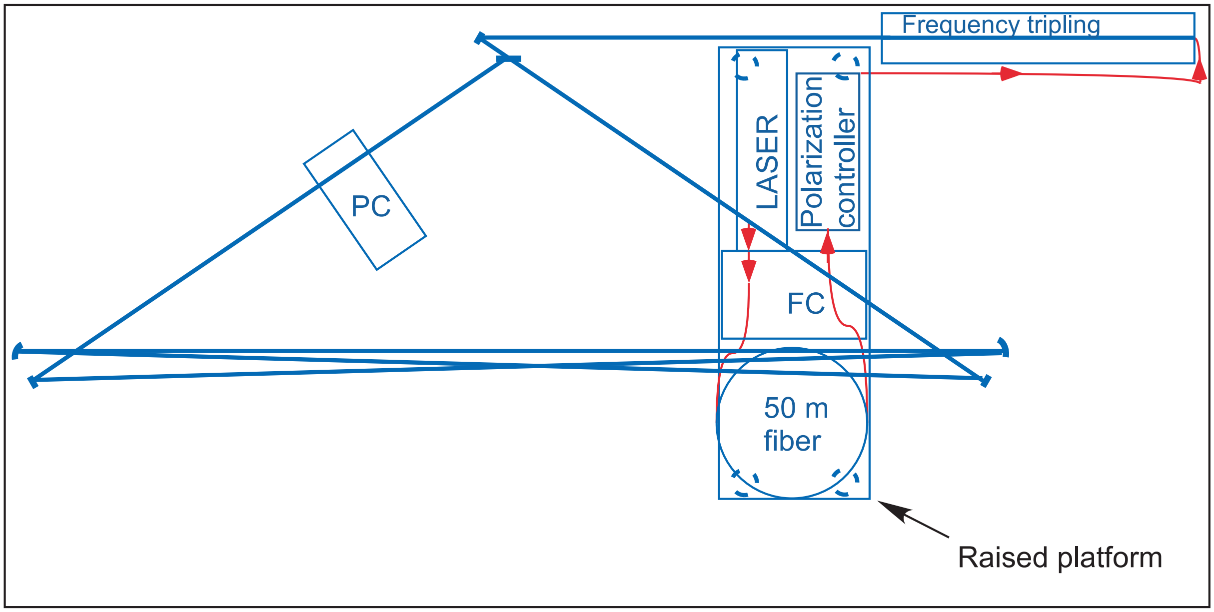

Figure 8.2: Scale drawing of single-photon source: pump laser and cavity. The pump laser (Nd:YAG) is first fiber coupled (FC) into a 50-m single-mode optical delay fiber, which passes through a “bat-wing”-type polarization controller. The beam is then frequency tripled from 1064 nm to 355 nm. The resulting UV pump pulse is switched via a Pockels cell (PC) into the cavity that stores vertically polarized light.

elevated platform above the main experiment, to free up additional space on the table.

Because the laser is passively Q-switched, there is a shot-to-shot pulse jitter of ∼2 μs. Therefore, one needs to synchronize the entire SPS on each laser pulse. The purpose of the optical delay is to give us time to switch the optical pulse into the pump recycling cavity. The optical delay must be longer than the summed latencies for the following components: the electrical pulse latency of the pump laser (∼3 ns); the latency of the Pockels-cell driver control electronics (47 ns and 62 ns, for the BME Bergmann SG04p4 and SG05p2 digital delay cards[5], respectively); and the latency of the Pockels cell driver (34 ns for a BME Bergmann PCD_dpp). Assuming use of the slower delay generator, one needs ∼100 ns of delay plus time for electrical propagation through the cables[6]. The fiber is directed through a polarization controller, and then brought to the main table height. The beam is then collimated and directed through the frequency tripling system, where the 1064-nm

---

[5] Preliminary measurements indicate that the electrical pulse from the 1064 nm laser is sufficient to trigger the delay cards directly.

[6] Using Pasternack RG 223/U cable to make a 2.22-m BNC cable gives an 11.4-ns delay. Thus, typical cables add ∼5 ns of delay for each meter.

pump pulse is converted to 355 nm.

Tripling is accomplished using two 10-mm long Lithium Triborate (LBO) crystals[7]. The first (cut at θ=90° and ϕ=11.4°, for type-I phase-matching) doubles $\sim$ 67% of the 1064-nm light to 532 nm. This 532-nm light and the remaining 1064-nm light undergo sum-frequency generation in the second LBO crystal (cut at θ=42.7° and ϕ=90°, for type-II phase-matching), resulting in 355-nm light. At present, our best attempts at frequency tripling have yielded ~8 mW of average power[8] at 355nm.

The UV cavity will be constructed[9] with a Brewster-angle polarizing beam splitter (PBS) (CVI TFP-55-PW-2025-UV), two flat mirrors, and two 2-m radius of curvature concave mirrors (CVI Y3-0537-0-2.00CC). We selected a Brewster-angle UV PBS after we found that other types of UV PBSs typically have loss of 5%. Such a loss would attenuate the pump pulse so the full benefits received from recycling would not be realized. The coated side of the UV Brewster-angle PBS should be set at 55.75° from normal angle of incidence, to achieve maximum transmission of horizontally polarized light (~95%) and maximum reflection of vertically polarized light (~96%)[10].

We intend on using a BME Bergmann Pockels cell driver to drive a BBO[11] Pockels cell (Cleveland Crystals Light Gate 5, half-wave voltage at 355 nm is 2.44 kV) to switch into the pump recycling cavity by rotating the horizontally polarized pump pulse to vertical polarization. The driver provides variable pulse lengths, with rise and fall times less than 5 ns. We expect to use a pulse length of ~10 ns for switching.

Once the pump pulse is switched into the cavity, we expect the cavity transmission to be 91.3% per round trip, due to losses in the Pockels cell (~2% loss[12]), mirrors (~0.5% loss per mirror for four mirrors), downconversion crystal (~1% loss) and UV PBS (~4% loss). We characterized the transmission/loss of the UV cavity elements using a cw Argon-ion laser at 351 nm. Such a

---

[7] This system is being constructed by Aaron VanDevender.

[8] This number was measured before we installed the fiber-optic delay. Currently, after installation of the fiber delay, we are having some difficulties with the tripling crystals. LBO is slightly damaged by moisture, thus it is possible our crystals have been damaged from long-term exposure to moisture in the air.

[9] We decided to construct and understand the conditionally-prepared photon cavity before the UV cavity for two reasons. First, it is easier to align and test with a visible laser (688 nm diode); second, we can easily make more accurate measurements by using cw or quasi-CW lasers than the 0.5-ns pulse length UV source.

[10] We think this can be improved using a better measurement technique. Even if it cannot, a custom coated optic (like the PBS we use for the switchable cavity discussed below) should achieve 99.5% for the maximum reflection of vertically polarized light.

[11] We choose BBO for its high transmission.

[12] The minimum loss n this case is not centered and on axis through Pockels cell. Perhaps it is damaged.

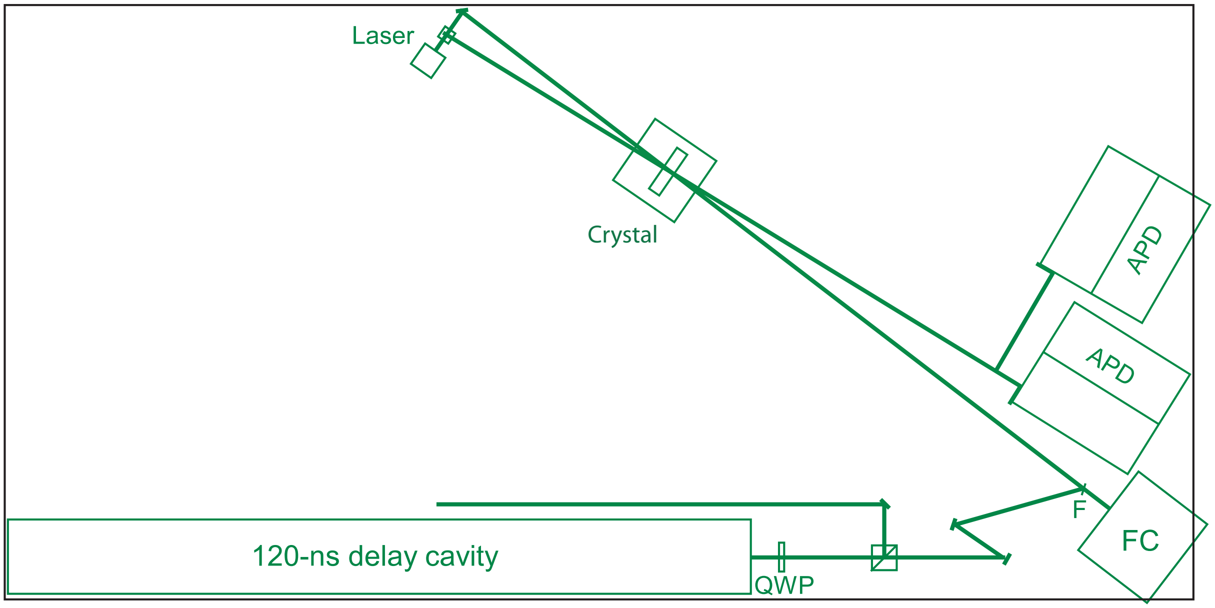

Figure 8.3: Scale drawing of single-photon source: Downconversion crystal and fixed optical delay. Also shown is an alignment laser and detectors (FC and APD, see text).

characterization avoided the difficulty associated in measuring the intensity of short pulses.

8.1.2 Downconversion and fixed optical delay

Each cycle in the cavity, the 355-nm pulse pumps the downconversion crystal to create a 710-nm trigger photon and a 702-nm conditionally-prepared photon[13,14] (see Fig. 8.3). As yet, the best phase-matching choice for collecting the photon outputs is unclear. Our original plan is to use type-II "beamlike" downconversion [117, 118][15], because we thought we could collect more of the photons from a beamlike mode than from a section of the type-I cones. After collection, the mode must be converted so that it is matched with the acceptance modes of each cavity. This is a nontrivial issue that will have to be investigated theoretically and experimentally.

Following the downconversion crystal are several detectors. The trigger photon directed by a beam splitter to one of two APDs, thereby giving partial multi-photon discrimination: the probability of multiple photons in the output is reduced because we can reject double-pair events that fire

---

[13] Both with 5 nm bandwidths, determined by an interference filter in the trigger arm.

[14] For type-II phase-matching in BBO, the phase-matching angle is 47.99° for these wavelengths.

[15] To do the calculation for type-II beamlike downconversion, we used the NIST 'Phasematch' program (http://physics.nist.gov/Divisions/Div844/facilities/cprad/PMProgram.html)[119].

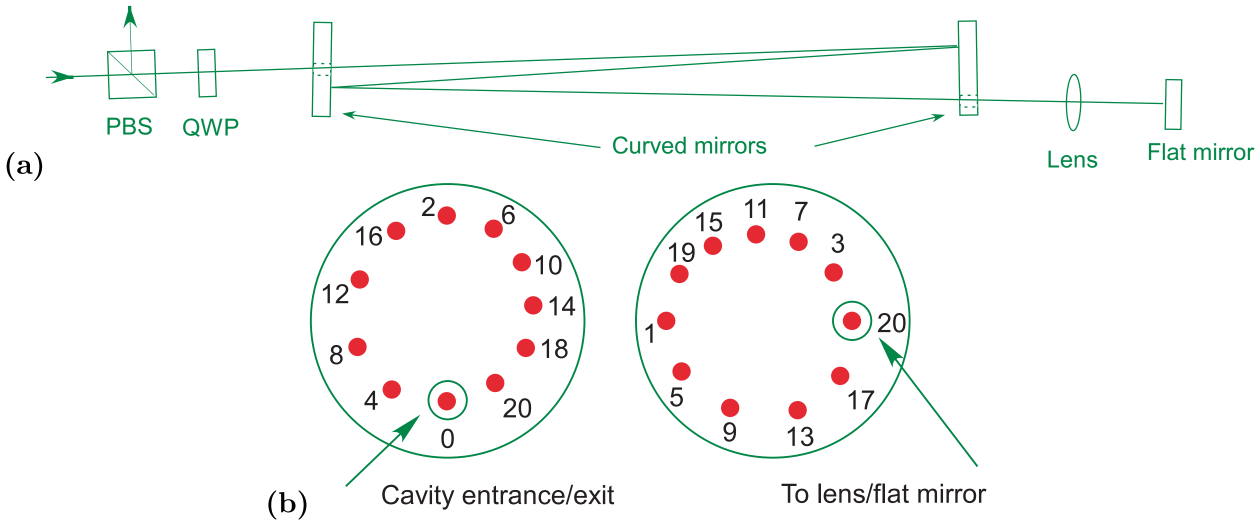

Figure 8.4: Herriot cell fixed optical delay. (a) A horizontally polarized photon is input from the left passing through a polarizing beam splitter (PBS) and a QWP set to rotate the photon's polarization to circular. The photon passes through a hole in a curved mirror bouncing several times between the two curved mirrors before it passes through the hole in the second curved mirror, where it is focused by a lens onto a flat mirror. Upon reflection off the flat curved mirror, the photon follows its previous path in reverse order. The QWP rotates the polarization state to vertical and the photon exits out the reflected port of the PBS. (b) A close-up of the spot pattern on the 2-inch mirrors. The photon enters at 0 and bounces between the mirrors in numerical order.

both APDs. On the conditionally prepared photon mode, a mirror on a kinematic or a translating mirror mount (labeled "F" on Fig. 8.3) is used so that we can place a fiber coupler (leading to another APD) behind it to collect downconversion for alignment purposes.

When the mirror F is in place, the light is directed to a fixed optical delay that serves the same purpose for the conditionally prepared-photon cavity as the fiber delay does for the UV cavity. Here we employ a Herriot cell (see Fig. 8.4) using 2-inch diameter concave curved mirrors with a 1-m radius of curvature[16]. We have built a 10-spot Herriot cell and measured a time delay of 121 ns, with a transmission of 78.4%, only slightly lower than the expected transmission (79.5%, based on individual transmission measurements on the components)[17]. The Herriot cell's delay is chosen to give us time to fire the Pockels cell in the switchable cavity conditional on a detection from

---

[16] These mirrors are custom optics from CVI with the standard 'R1' coating. Each mirror has a ∼5-mm hole centered ∼7 mm from the edge of the mirror. The holes are used for coupling light into and out of the cavity.

[17] We attribute the loss discrepancy to beam clipping at the hole in the second mirror. This loss is a strong function of the quality of the input mode. Ideally, the input mode would have a diameter d, smaller than the 5-mm in-coupling hole, and a beam waist at the center of the two curved mirrors. If the focus is not at the center of the curved mirrors, then the diameter will be larger than d at the second mirror's out-coupling hole, causing clipping.

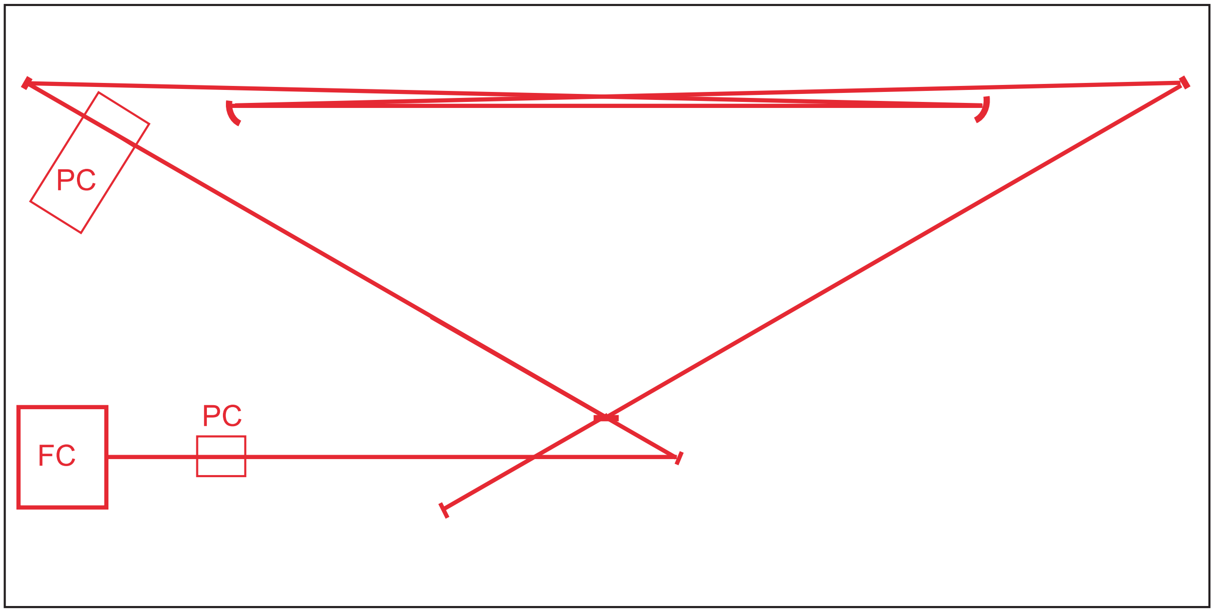

Figure 8.5: Scale drawing of single-photon source: switchable cavity.

either of the trigger APDs. The latency for a typical APD is just under 13 ns. Combined with the faster digital delay card listed above and a Pockels cell driver, we need an optical delay of ∼95 ns. Therefore, our measured optical delay of 121 ns, leaves adequate time for the extra delay added by connecting cables.

8.1.3 Switchable cavity

The switchable cavity shown in Fig. 8.5 is the heart of our approach to a deterministic single-photon source. It should be the same length as the UV pump cavity in Fig. 8.2 to synchronize the optical switching. However, we decided to design this cavity using 1.5-m radius of curvature concave mirrors (CVI R1-1037-0-1.50CC) instead of the 2-m radius of curvature mirrors of the UV cavity, as it was easier to accommodate the large cavities (and other experimental components) with slightly different shapes.

The cavity length is chosen to optimize between two competing elements, the space on our optical table and the minimum time required to fire our Pockels cell a second time for switch-out (after the initial switch-in). In the limit of unlimited table space, we would choose our cavity length to coincide with the shortest switching time we can achieve with our Pockels cell driver.

This way, we could actively switch out a photon after it has undergone one cycle in the cavity[18]. The difficulty is in obtaining a Pockels cell driver that can do everything well. With a Pockels cell driver from BME Bergmann, we can fire a second pulse no earlier than 50 ns after the previous pulse is off. Combined with a rise time that is under 5 ns, the earliest we could switch a photon out of the cavity is 55 ns after it is switched in. A 55-ns cavity with an open design such as drawn in Fig. 8.5 on a 8'x4' table is unwieldy. Thus, we have designed a 27.1-ns cavity that can switch a photon out after two cycles[19].

We have measured the transmission of the Pockels cell (BBO, Cleveland Crystals Light Gate 5, 702-nm half-wave voltage=4.9 kV) to be 99.4±0.2% at 702 nm. The reflectivities of the four mirrors are typically 0.996, and the reflectivity of the custom Brewster-angle PBS (from MLD Technologies) is 0.995 for the stored, vertical polarization[20]. Thus we expect the storage loss of the switchable cavity to be 3% per cycle. We have not yet attained this efficiency, but have constructed a cavity and need to properly match the input mode to the cavity.

In previous designs for this cavity, we were unable to get a stable spot size and shape for even two or three passes through the cavity. We discovered through an ASAP model of the cavity that hitting the curved mirrors away from normal incidence caused astigmatism in the cavity[21] mode. For this reason, we chose incident angles for the curved mirrors of $\sim 1^\circ$.

Finally, at the output of the single-photon source, we have one last Pockels cell (Lasermetrics 1147-6, Rubidium Titanyl Phosphate [RTP], 702-nm half-wave voltage 1.22 kV) and polarizer to ensure no photons leave the source except when that cell is energized. We estimate that the last cell and polarizer will have 97% transmission. After the polarizer, we initially plan to fiber couple the output of the single-photon source, in order to analyze the output using a fiber beam splitter connected to two APDs.

---

[18] If we knew we would switch out after one cycle, we would not fire the Pockels cell at all, and a photon would come out of the cavity after one pass. Then we would fire the final Pockels cell to allow that photon to leave the SPS.

[19] We would like to make the cavity a little bit longer than 27.5 ns but space limitations constrained us. If we cannot get reliable switching (there may not be enough time to reach to the half-wave voltage of the Pockels cell), we will have to consider a three-cycle minimum hold time.

[20] The Brewster angle of this PBS is 60°, as measured by Kyle Arnold.

[21] Kyle Arnold developed the ASAP optical model.

8.2 Theoretical performance

The performance of a single-photon source can be characterized using the probability of success and the probability of different types failure when a photon is switched out[22]. Success is achieved when exactly one photon is switched out. Failure occurs when no photon is switched out or when more than one photon is switched out. There are many reasons that could cause failure: no photon pair was produced, a photon pair was produced but the trigger photon was not detected (so the conditionally prepared photon was not switched into the holding cavity), the conditionally prepared photon gets absorbed or scattered, or multiple-photon pairs are created but not detected as such. There are several aspects of the source that determine the performance, including the detection efficiency, the number of times a pump pulse is recycled through the crystals, and the transmission of cavities and optics used to hold and steer the photons.

To analyze the system we will first discuss the detection of the trigger photon. Using a tree[23] of D detectors allows one to partially discriminate multi-photon events, thereby reducing the probability of a multiple-photon output. We assume these detectors have identical efficiencies (q)—where this detection efficiency, even though it is a combination of an APD quantum efficiency, and spectral and spatial filtering, is modeled as a neutral density filter followed by a tree of perfectly efficient detectors. If the detectors are of unequal efficiency, then a more sophisticated analysis is needed [120].

Following reference [76], the probability of emitting x photons for a given pump pulse cycle is:

$$p(x) = \textstyle\sum_{i=1}^{n}(1 - \sum_{k=1}^{n} \mathit{create}(k)\mathit{detect}(1|k))^{i-1} \sum_{k=1}^{\infty} \mathit{create}(k)\mathit{detect}(1|k)\mathit{emit}(x|k), \qquad (8.1)$$

where $\mathit{create}(k)$ is the probability a single pulse gives k output pairs; $\mathit{detect}(m|k)$ is the probability of detecting m trigger photons from k created pairs (from a single pulse); and $\mathit{emit}(x|k)$ is the probability of emitting x conditionally prepared photons from k created pairs. If we break this equation up, the first term is the probability that the first $i-1$ pump pulses did *not* cause a

---

[22] The original theoretical basis for this section was developed by Evan Jeffrey and published in [76]. Here we reiterate and extend the analysis in [76] to consider real experimental challenges. The plots in this section reflect these extensions.

[23] We can construct a detector tree by sending the downconversion mode into a beam splitter that will create two more modes. These modes can in turn be sent into beam splitters to create four output modes. This process can be repeated N times to create an array of $D = 2^N$ output modes, with a detector placed in each mode.

single trigger photon detection, and therefore the optical switch into the cavity did not fire. This probability is then multiplied by the probability of detecting one photon and emitting x photons on pump pulse i. Then this product is summed over n pump pulses, yielding the probability of emitting x conditionally prepared photons in one of these pulses. $p(0)$ is the probability that a pair is created, but the conditionally prepared photon is lost before reaching the output. Note that, were we to sum over all x values, the result would be *less* than unity; the remaining probability corresponds to the case where no trigger detector fires so there are no known output photons.

The forms of the generic terms in eqn. 8.1 are derived in [76]. Briefly, $create(k)$ is a Poisson distribution:

$$create(k) = P_\lambda(k) = \frac{e^{-\lambda}\lambda^k}{k!}, \tag{8.2}$$

where λ is the mean number of downconversion pairs created per pump pulse. The value of λ is a function of the pump power, the crystal material and the crystal length. The emission probability is given by

$$emit(x|k) = (\eta^{n-i})^x (1-\eta^{n-i})^{(k-x)} \binom{k}{x}, \tag{8.3}$$

where η^{n-i} is the transmission of the storage loop that holds the conditionally prepared photon for $n-i$ pump pulses. Here we have used a binomial distribution to count the number of ways x photons are emitted given k attempts, where each attempt is a created photon.

Finally, the probability of detecting exactly one trigger photon is the sum over l of the product of the probability of detection using ideal photon-number counting detectors times the probability $\left(\frac{1}{D}\right)^{l-1}$ that all l trigger photons go to the same detector (falsely giving the appearance that only a single photon was counted); the result is

$$detect(1|k) = \sum_{l=1}^{k} q^l (1-q)^{(k-l)} \binom{k}{l} \left(\frac{1}{D}\right)^{l-1}, \tag{8.4}$$

where as before, q is the detection efficiency, and D is the number of detectors in the detection tree.

There are two additional effects not accounted for in the preceeding the preceeding analysis. First is the fact that the cavity that recycles the pump is not loss free. Loss in the pump recycling cavity is due to reflection losses of mirrors, the optical switch (i.e., a Pockels cell and a polarizing

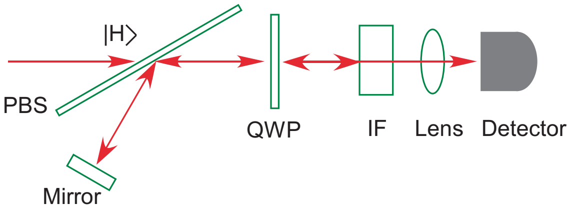

Figure 8.6: Recycling technique to improve interference filter (IF) transmission (see text).

beam splitter), and the downconversion crystal. These losses lower the pump power each cycle; when considered together, the effect is that λ, the number of downconverted pairs created, becomes a function of the number of cycles: $\lambda \to \lambda\eta_{\mathrm{UV}}^{i}$, where η_{UV} is the probability of transmission for one round trip of the pump cavity, and i is the number of cycles that the pump pulse has undergone. The second effect, discussed below, is the loss in all the miscellaneous optics through which the conditionally prepared photon passes, not including the storage cavity. (We will call the net transmission "T misc. optics" when labeling plots that follow.) We scale the probability of output single-photon events by this transmission and the probability of two-photons events by the square of the transmission (and add losses to the zero-photon emission probability).

8.2.1 Expected experimental performance

In the preceding parts of this section we have discussed the performance of various parts of the single-photon source. Here we will give details on how we expect the remaining elements to impact the performance and give realistic estimates of our ability to create single photons. There are two things left to consider, estimates of the detection efficiency and the miscellaneous optics loss.

We discuss the latter first. We expect to use two mode-matching lenses before the Herriot cell optical delay and the switchable cavity. A reasonable transmission for each non-custom coated lens is 98%. Additionally, there are 5 steering mirrors that we assume have reflectivities of 0.996, based on measurements of several similarly coated mirrors from the same manufacturer (CVI coating R1). Finally, we account for the 99.4% transmission through the custom Brewster-angle PBS on switch-in and switch-out. When the PBS, steering mirrors and mode-matching lenses are combined with the Herriot cell and the last Pockels cell/polarizer switch, we estimate that T misc. optics is 67.9%.

The detection efficiency is a function of the transmission through the coupling lens (we assume

98% transmission, typical for anti-reflection-coated lenses), the efficiency of the detecting APD 65% [24], and the ∼75% transmission of an interference filter (Omega Optical 5-nm bandpass centered at 710 nm); the product of these three numbers gives ∼48% detection efficiency. However, by using a recycling technique[25] we should be able to increase the net transmission probability through the interference filter, and therefore the detection efficiency. To do this a PBS and QWP (oriented to convert the PBS's horizontal transmitted polarization to circular polarization) are inserted before the interference filter (see Fig. 8.6). Now any light reflected from the interference filter (which is the source of most of its loss) travels back through the QWP (converting it to vertical polarization) and out the vertical port of the PBS. If a retroreflecting mirror is placed at this output, the portion of light reflected from the interference filter will get a second chance at being detected. Thus the single-pass transmission T_f of the filter is effectively improved to $T_f' = T_f + R_f T_f = T_f[1+(1-T_f)]$, where we have assumed the filter reflectance $R_f \equiv 1 - T_f$, i.e., a lossless filter. This should raise the filter transmission to ∼94% and the detection efficiency to 60%. However, when one considers the losses from required extra mirror, QWP and PBS, we estimate the detection efficiency will be 58%.

Using the experimental parameters we have discussed and the results of section 8.2, we can plot the expected performance[26] of our single-photon source versus the strength of the pump pulse (which we parameterize by λ, the average number of photon pairs created each time the pump passes through the downconversion crystal) and the number of pump cycles n before we attempt to switch out the conditionally prepared photon. To start with, we fix λ=0.5 while varying the number of pump cycles (Fig. 8.7(a))[27]. For comparison, we plot 14 pump cycles as a function of average pairs per pump pulse in Fig. 8.7(b). For our experimental parameters, using λ=1.2 with 11 pump cycles seems close to optimal[28] in terms of maximizing the difference of P(2) from P(1), giving P(0)=0.38, P(1)=0.56 and P(2)=0.06.

---

[24] The efficiency was measured by Aaron VanDevender for 631 nm. While not very near the 702-nm wavelength in which we are interested, this number provides an estimate that includes reflection loss of the APD window and detector surface.

[25] This technique was first suggested by Andrew White.

[26] These plots do not account for the double-pass required for switching, which should not have a significant effect.

[27] With a 1-mm thick BBO crystal and our 50-mW average power pump laser, we hope to reach λ=0.5. However, we lose 70% of our pump power when coupling into a single-mode fiber, and we do not yet know how efficiently we can frequency-triple the 1064-nm pulse.

[28] We searched from 1 to 50 pump cycles and from 0.1 to 1.5 average pairs per pump pulse (in steps of 0.1).

8.3 Future upgrades

The first upgrade we envision is the ability to switch a second photon into the switchable cavity if one is conditionally prepared on a pump cycle later than the first photon but before the switch-out time. Thus, the first photon which is subject to 3% loss per cycle and has a reduced probability of exiting the cavity can be replaced by a "fresh" photon that has not yet been subject to such loss. The difficulty in switching in a fresh photon lies in firing the Pockels cell a total of three times in rapid succession (to switch in the first photon, to eject the first photon and switch in the second, and finally to switch out the second). We are currently working with BME Bergmann on securing a Pockels cell driver that can make three such switchings[29]. The loss reduction improves our expected results, as shown in Fig. 8.7 (c) and (d). More quantitatively[30], for λ=1.5 and 16 pump cycles, P(0)=0.38, P(1)=0.57 and P(2)=0.05.

If in addition to switching in a "fresh" photon, one used higher reflectivity mirrors, a higher reflectivity UV PBS, higher transmission lenses and very high efficiency photon-number resolving detectors[31] (modeled with D=10), then one can enhance the performance significantly, as shown in Fig. 8.7 (e) and (f). These improvements are based on 99.9%-reflectivity mirrors and 99%-transmitting lenses for the conditionally prepared single photon, in addition to an assumed detection efficiency of 90%. The net transmission of miscellaneous optics will thereby increase to 82% (with the Herriot cell's transmission rising to 90%). Additionally, with a better UV PBS, the UV cavity transmission will rise to 96%, while the switchable cavity transmits 98.5%. In this case, the single-photon source has the following optimal performance: P(0)=0.23, P(1)=0.75 and P(2)=0.02, obtained for 44 cycles with 1.5 pairs produced per pump pulse.

In this chapter we have discussed the performance, design, and progress on the construction of a periodic single-photon source, and highlighted possible future upgrades. While our theoretical analysis does not account for limits in switching, e.g., the fact that we can only switch a photon

---

[29] However, according to Thorald Bergmann, with such a device, it seems the soonest we will be able to switch out the second photon will be 100 ns after it is switched into the final cavity, due to the time needed to recharge the driver.

[30] This analysis does not account for the three passes (∼100 ns) required to fire the Pockels cell a third time, which will slightly reduce the performance.

[31] In particular, there are at least two types of detectors that have photon-number counting capability and inferred quantum efficiencies in excess of 94% in the visible spectrum [121, 122]. We are currently in the process of setting up systems with high collection efficiency that utilize both types of detectors.

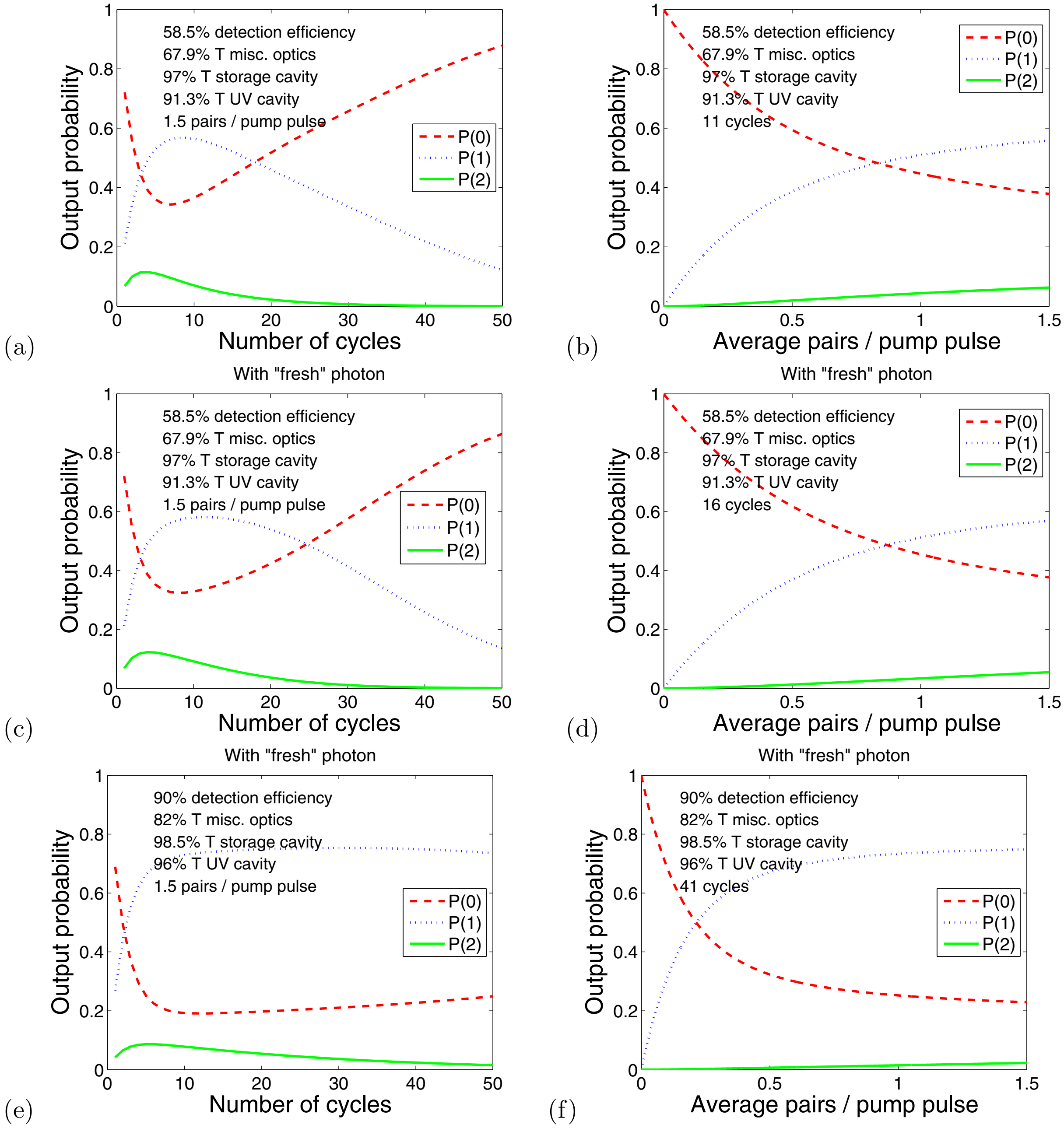

Figure 8.7: Expected performance of single-photon source. P(1) is the probability of emitting a single photon at the output. P(0) and P(2) are failure probabilities, with 0 or ≥ 2 photons (exactly two photons is the largest term here), respectively. (a), (c), and (e) shows how the probabilities change as a function of the number of pump cycles for a fixed downconversion pair creation probability of 1.5 pairs/pulse. (b) fixes the number of cycles at 11 and varies the pair-creation likelihood. (c) and (d) Expected performance of single photon source with “fresh” photon switch-in. (e) and (f) Expected performance of single-photon source with “fresh” photon switch-in, better optics, and high-efficiency photon-number resolving detectors (see text). Note that in (d) and (f), the number of pump cycles increases from what is used in (b), as it is advantageous to do so when one has the ability to switch the extra photon into the final cavity.

out of the final cavity after it has made at least two passes, it provides research direction and sets realizable performance goals. It is our hope that such a source and the techniques required for its implementation will prove useful for other quantum information tasks.

Chapter 9

Summary and conclusions

In this thesis we have described the precise creation of various photonic quantum states and their use for quantum information. Specifically, we discussed the production and characterization of arbitrary single-qubit polarization states, two-qubit polarization-entangled states, and the more complex two-qubit maximally entangled mixed states (MEMS).

These experimental studies also prompted us to consider how common state-quality benchmarks behave under variation. Specifically, we have shown an imbalance between the sensitivities of the common state measures–fidelity, trace distance, concurrence, tangle, linear entropy and von Neumann entropy–for MEMS and a generalized Werner state. We investigated several examples at different locations in the entropy-tangle plane, where the trend shows progressively larger constant-fidelity regions as the state becomes more mixed and less entangled. We also showed that, at least for maximally entangled target states, the fidelity is insensitive when comparing between Werner states and nonmaximally entangled states of the same tangle. This work has important ramifications for benchmarking the performance of quantum information processing, as it may be beneficial to include other benchmarks in addition to/instead of fidelity, when characterizing resources needed for various quantum information protocols.

One such protocol is entanglement concentration. Our creation of MEMS allowed us to study "Procrustean" entanglement concentration, which can be substantially more efficient than other concentration schemes, even if it is less general. However, in the limit of very strong filtering, small perturbations in the initial state will eventually dominate the process, yielding only product states. In practice, therefore, it may be optimal to combine both methods of entanglement concentration. In this case, an ensemble of identically prepared photons could be divided such that the first fraction could be measured via tomography to choose the optimal Procrustean filter. Then, Procrustean concentration may be carried out until the state reaches its maximum entanglement. At this point, interference-based concentration methods could be applied to achieve maximally entangled states.

We also demonstrated the first arbitrary remote state preparation (RSP), a way to send quantum information without requiring Bell-state analysis, in contrast to quantum teleportation. Specifically, we were able to remotely prepare arbitrary polarization qubits with all fidelities in excess of 0.99. The experimental methods employed for RSP may be useful for state control in linear optics feed-forward quantum computation. Moreover, by varying the acceptance wavelength of the trigger photon (using a nondegenerate entangled source) we also controlled the *wavelength* of the remotely prepared qubit. Such a capability may assist in the preparation of states at wavelengths more optimal for other quantum communication protocols, e.g., quantum cryptography.

Using both remotely and directly prepared single-qubit mixed states, we have experimentally explored the concept of geometric phase for mixed states. Even though the two methods are conceptually different, both gave geometric phase and visibility data in very good agreement with the theoretical predictions This indicates that, at least in some cases, our method of decohering with birefringent elements creates legitimate “mixed” states. With the experimental ability to manipulate geometric phase of mixed states, we envision further exploration of its use as a fault-tolerant qubit.

Finally, we discussed another special kind of remote state preparation, using pulsed downconversion to prepare a single-photon state at regular intervals, but within a narrow time window, upon the measurement of a spontaneously created trigger photon. We have given estimates of the performance of the proposed source based on preliminary measurements of individual components. We estimate that with planned future upgrades, this source will become a valuable tool for exploring quantum information science.

We have explored quantum state creation, control and measurement. We have applied these techniques to develop the technology of quantum information: transmission of quantum information, mitigation the undesirable effects of decoherence, measurement-based fast-feed forward control, and fast optical switching. While we have concentrated on free-space implementations using polarization qubits at optical wavelengths, we expect these techniques can not only be applied to different photonic degrees of freedom and wavelengths more suitable for long distance fiber communication, but also to other quantum systems. In fact, these techniques may prove even more useful in the hybridization/connection of different quantum systems, e.g., making arbitrary measurements on a photon that is entangled with an atom to remotely prepare a particular atomic state. Such schemes could play a vital role in networking between distant quantum nodes.

Appendix A

Decoherence using imbalanced polarization interferometers

Decoherence always arises from the entanglement of the quantum system being considered to some other quantum degree of freedom, which is then traced over. In our system we realize decoherence by coupling the frequency and polarization degrees of freedom and then measuring in a frequency-insensitive way [27].

A.1 Single-qubit decoherence

The state of a photon written in terms of its polarization and frequency spectrum is $|\xi\rangle = (\alpha|H\rangle + \beta|V\rangle) \otimes \int d\omega A(\omega)|\omega >$, where α and β are complex normalized coefficients, and $A(\omega)$ is the complex amplitude for frequency ω, normalized such that $\int d\omega |A(\omega)|^2 = 1$.

To decohere in the $|H\rangle/|V\rangle$ basis, we send the photon through a birefringent element (a "decoherer") whose fast axis is parallel to the horizontal polarization. Traversing a birefringent element of length L adds a phase that is polarization and frequency dependent, producing the state $|\xi_D\rangle = \int d\omega (e^{i\frac{n_H L}{c}\omega}\alpha|H\rangle + e^{i\frac{n_V L}{c}\omega}\beta|V\rangle)A(\omega)|\omega >$. Tracing over the frequency gives

$$|\xi_D\rangle \rightarrow \rho_D = \begin{pmatrix} |\alpha|^2 & \alpha\beta^* \int_{-\infty}^{\infty} d\omega |A(\omega)|^2 e^{i\phi(\omega)} \\ \alpha^*\beta \int_{-\infty}^{\infty} d\omega |A(\omega)|^2 e^{-i\phi(\omega)} & |\beta|^2 \end{pmatrix}, \tag{A.1}$$

where $\phi(\omega) = (n_H - n_V)\frac{L}{c}\omega$[1]. As long as $(n_H - n_V)L$ is much greater than the photon's coherence length[2], the off-diagonal elements of expression (A.1) will effectively average to zero, and the polarization state will be fully decohered. Note that although this form of decoherence due to dephasing is reversible (i.e., by using a compensating birefringent element), it is fundamentally no different than any other type of decoherence, which *in principle* is always reversible if one could access the entire Hilbert space describing all parts of the experiment.

---

[1] Here we neglect the slight variation of n with ω.

[2] The coherence length (L_c) of the photon is determined by the Fourier transform of the spectrum $A(\omega)$. For example, if $A(\omega)$ is a Gaussian of full width at half maximum $\Delta\omega$, then $L_c = \frac{2\pi c}{\Delta\omega}$.

Appendix B

Phase-matching in BBO

First observed by Burnham and Weinberg, we use spontaneous parametric downconversion (SPDC) to create photons pairs [23]. In this Appendix, we will describe how one calculates the type-I phase matching angles for a uniaxial nonlinear crystal. We will illustrate this method with a specific calculation for the phase-matching angles that were used most commonly in this dissertation using β-Barium Borate (BBO).

A pump photon with wavelength λ_p interacts with a nonlinear crystal to generate daughter photons of wavelengths λ_1 and λ_2 such that energy is conserved:

$$\frac{1}{\lambda_1} + \frac{1}{\lambda_2} = \frac{1}{\lambda_p}. \tag{B.1}$$

Similarly, momentum inside the crystal is conserved via the phase-matching condition:

$$\vec{\kappa}_1 + \vec{\kappa}_2 = \vec{\kappa}_p, \tag{B.2}$$

where we define $\vec{\kappa}_i \equiv |\kappa_{i,e}|\hat{e} + |\kappa_{i,o}|\hat{o} \equiv \frac{2\pi}{\lambda_i}[n_e(\lambda_i)\hat{e} + n_o(\lambda_i)\hat{o}]$ for $i = \{1, 2, p\}$ where n_o (n_e) is the crystal's ordinary (extrordinary) index of refraction, and $\hat{o}$ and $\hat{e}$ are unit vectors that indicate the ordinary and extraordinary axes, respectively. The phase-matching condition is illustrated graphically in Fig. B.1. In type-I phase matching, the pump has extraordinary polarization while the downconversion pair has ordinary polarization. For example, a nonlinear crystal (e.g., β-barium borate [BBO]) is pumped with polarization in the plane of the crystal axis. This generates daughter photons with polarization orthogonal to that of the pump, e.g., vertically polarized light pumping

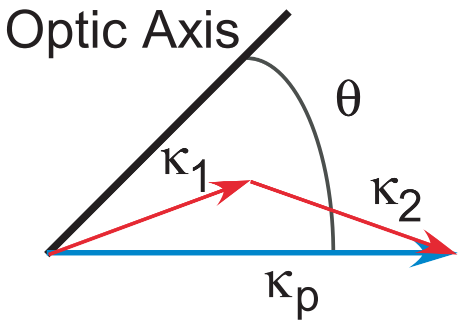

Figure B.1: Graphical phase matching condition. Corresponding to equation B.2, shown is the phase matching condition for a pump at angle θ with respect to the optic axis.

i	A_i	B_i	C_i	D_i	$n_o(\lambda{=}0.351\ \mu\text{m})$	$n_e(\lambda{=}0.351\ \mu\text{m})$
o	2.7359	0.01878	0.01822	0.01354	1.707	1.665
e	2.3753	0.01224	0.01667	0.01516	1.578	1.548

Table B.1: Sellmeier coefficients for BBO at 20°C [123]. Using the Sellmeier coefficients and equations B.4 and B.3, we can calculate BBO's indices of refraction for 351 and 702 nm.

a crystal with its optic axis in the vertical plane generates pairs of horizontally polarized photons.

As a function of wavelength (λ), the two indices of refraction are given by

$$n_o^2(\lambda) = A_o + \frac{B_o}{\lambda^2 - C_o} - D_o\lambda^2 \quad \text{and} \tag{B.3}$$

$$n_e^2(\lambda) = A_e + \frac{B_e}{\lambda^2 - C_e} - D_e\lambda^2, \tag{B.4}$$

where A_i, B_i, C_i, and D_i are the Sellmeier coefficients (for BBO values, see table B.1), and λ is the wavelength in μm. For our typical experimental setup, relevant values of the indices of refraction for BBO are given in table B.1.

The ordinary polarized light always has the same index of refraction, but the index for extraordinary polarized light can vary from n_o to n_e depending on the propagation direction relative to the optic axis of the birefringent crystal (θ, see Fig. B.2). It can be shown that [123]

$$n_e(\theta,\lambda) = n_o\left[\frac{1+\tan^2\theta}{1+\left(\frac{n_o(\lambda)}{n_e(\lambda)}\right)^2\tan^2\theta}\right]^{\frac{1}{2}}. \tag{B.5}$$

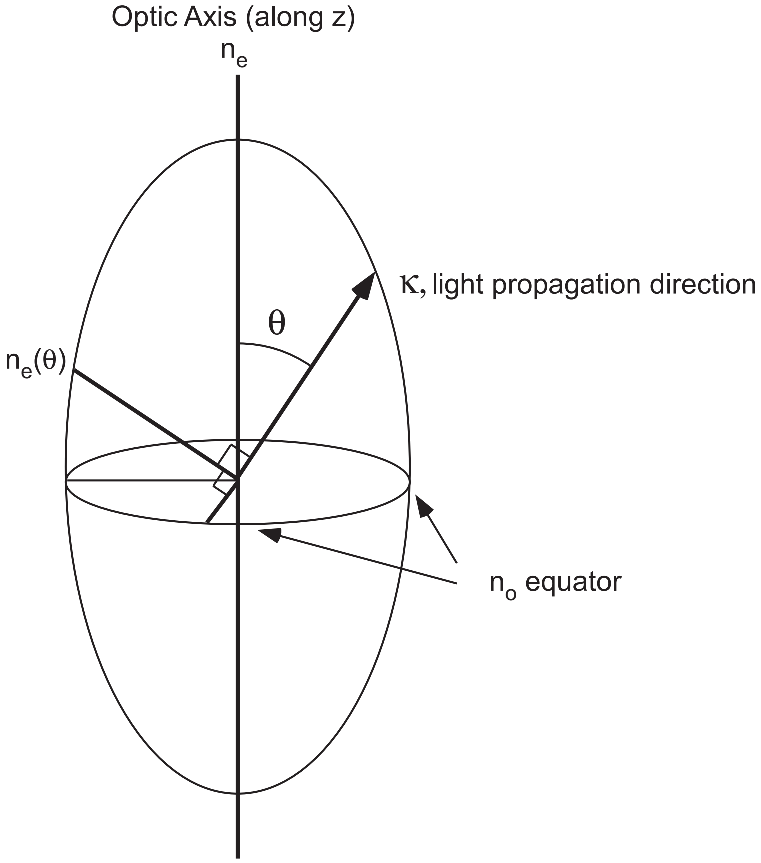

Figure B.2: The index ellipsoid shows how light propagating in a birefringent nonlinear crystal propagates. There are two polarizations, both in planes perpendicular to the propagation direction. The first polarization, the extraordinary polarization, lies along the line labeled $n_e(\theta)$. Orthogonal to the extraordinary polarization is the ordinary polarization which must lie in the plane defined by the n_o equator. The length of the n_o and $n_e(\theta)$ vectors gives the index corresponding to ordinary and extraordinary polarized light.

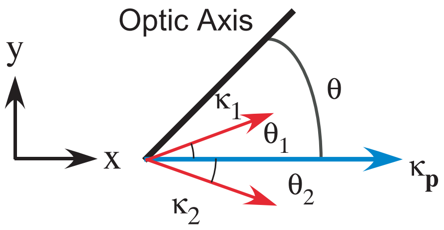

Figure B.3: Graphical representation for phase matching. Corresponding to equations B.6 and B.7, shown is the phase matching condition for a pump at angle θ with respect to the optic axis to generate a pair of photons at angles θ_1 and θ_2 (inside the crystal) with respect to the pump.

Now we discuss the phase matching for type-I noncollinear downconversion, where the daughter photons are created at angles θ_1 and θ_2 with respect to the pump inside the crystal (see Fig. B.3). In this case, Equation B.2 can be broken into x and y-components giving the following phase-matching equations for the x and y components, respectively,

$$\frac{n_o(\lambda_p)}{\lambda_p}\left[\frac{1+\tan^2\theta}{1+\left(\frac{n_o(\lambda_p)}{n_e(\lambda_p)}\right)^2\tan^2\theta}\right]^{\frac{1}{2}} = \frac{n_o(\lambda_1)}{\lambda_1}\cos\theta_1+\frac{n_o(\lambda_2)}{\lambda_2}\cos\theta_2 \quad \text{and} \tag{B.6}$$

$$\frac{n_o(\lambda_1)}{\lambda_1}\sin\theta_1 = \frac{n_o(\lambda_2)}{\lambda_2}\sin\theta_2. \tag{B.7}$$

Generally, one desires phase matching at particular angles *outside* the pump ($\theta_{a,1}$, and $\theta_{a,2}$), so we must use Snell's law to account for the angle change from BBO to air ($n = 1$). Thus we can write θ_j, ($j = \{1,2\}$) as

$$\theta_i = \mathrm{Sin}^{-1}\left[n_o(\lambda_j)\sin\theta_{a,j}\right]. \tag{B.8}$$

Using Equations B.8, B.6 and B.7, gives the expression for the phase matching angle, θ (and hence the crystal cut). For BBO, with $\lambda_1 = \lambda_2 = 702\mu m$, $\theta_{a,1} = \theta_{a,2} = 3^\circ$ and $\lambda_p = 0.351$ μm, the phase matching angle is 33.7°.

References

[1] P. W. Shor, in *Proc. of the 35th Annual Symp. on found. of Comp. Science* (IEEE Computer Society, Los Alamitos, CA, 1994), pp. 124–134.

[2] L. K. Grover, Phys. Rev. Lett. **79**, 325 (1997).

[3] L. K. Grover, Phys. Rev. Lett. **80**, 4329 (1998).

[4] C. H. Bennett and S. J. Wiesner, Phys. Rev. Lett. **69**, 2881 (1992).

[5] K. Mattle, H. Weinfurter, P. G. Kwiat, and A. Zeilinger, Phys. Rev. Lett. **76**, 4656 (1996).

[6] C. H. Bennett *et al.*, Phys. Rev. Lett. **70**, 1895 (1993).

[7] B. E. Kane, Nature **393**, 133 (1998).

[8] N. A. Gershenfeld and I. L. Chuang, Science **275**, 350 (1997).

[9] D. Loss and D. P. DiVincenzo, Phys. Rev. A **57**, 120 (1998).

[10] J. I. Cirac and P. Zoller, Phys. Rev. Lett. **74**, 4091 (1995).

[11] D. V. Averin, Fortschr. Phys. **48**, 1055 (1994).

[12] E. Knill, R. Laflamme, and G. J. Milburn, Nature **409**, 46 (2001).

[13] D. A. Lidar, I. L. Chuang, and K. B. Whaley, Phys. Rev. Lett. **81**, 2594 (1998).

[14] P. W. Shor, Phys. Rev. A **52**, R2493 (1995).

[15] A. M. Steane, Phys. Rev. Lett. **77**, 793 (1996).

[16] J. S. Bell, Physics **1**, 195 (1965).

[17] W. P. Bowen, R. Schnabel, P. K. Lam, and T. C. Ralph, Phys. Rev. Lett. **90**, 043601 (2003).

[18] S. L. Braunstein and H. J. Kimble, Phys. Rev. Lett. **80**, 869 (1998).

[19] S. L. Braunstein, Phys. Rev. Lett. **80**, 4084 (1998).

[20] S. Lloyd and S. L. Braunstein, Phys. Rev. Lett. **82**, 1784 (1999).

[21] N. Peters *et al.*, J. Quant. Inf. and Comp. **3**, 503 (2003).

[22] C. K. Hong and L. Mandel, Phys. Rev. Lett. **56**, 58 (1986).

[23] D. C. Burnham and D. L. Weinburg, Phys. Rev. Lett. **25**, 84 (1970).

[24] M. Born and E. Wolf, *Principles of Optics*, sixth ed. (Pergamon Press, New York, 1987).

[25] G. Fowles, *Introduction to Modern Optics*, 2nd ed. (Holt, Reinhart and Winston, New York, 1975).

[26] G. N. Ramachandran and S. Ramaseshan, Crystal Optics, 1961.

[27] A. J. Berglund, Dartmouth College B.A. Thesis, also quant-ph/0010001 (2000).

[28] R. Jozsa, J. Mod. Optics **41**, 2315 (1994).

[29] D. F. V. James, P. G. Kwiat, W. J. Munro, and A. G. White, Phys. Rev. A **64**, 052312 (2001).

[30] M. G. Raymer, D. F. McAlister, and A. Funk, in *Quantum Communication, Computing, and Measurement '98*, edited by P. Kumar (Plenum, New York, 2000), pp. 147–162.

[31] J. G. Rarity and P. R. Tapster, Phys. Rev. Lett. **64**, 2495 (1990).

[32] P. G. Kwiat *et al.*, Phys. Rev. Lett. **75**, 4337 (1995).

[33] J. Brendel, N. Gisin, W. Tittel, and H. Zbinden, Phys. Rev. Lett. **82**, 2594 (1999).

[34] C. A. Sackett *et al.*, Nature **404**, 256 (2000).

[35] J. Bao, A. V. Bragas, J. K. Furdyna, and R. Merlin, Nature Materials **2**, 175 (2003).

[36] P. G. Kwiat *et al.*, Phy. Rev. A **60**, R773 (1999).

[37] A. G. White, D. F. V. James, P. H. Eberhard, and P. G. Kwiat, Phys. Rev. Lett. **83**, 3103 (1999).

[38] http://www.physics.uiuc.edu/Research/QI/Photonics/Tomography/index.html .

[39] W. K. Wooters, Phys. Rev. Lett. **80**, 2245 (1998); V. Coffman and J. Kundu and W. K. Wooters, Phys. Rev. A **61**, 052306 (2000).

[40] S. Bose and V. Vedral, Phys. Rev. A **61**, R040101 (2000).

[41] T. C. Wei *et al.*, Phys. Rev. A **67**, 022110 (2003).

[42] A. G. White, D. F. V. James, W. J. Munro, and P. G. Kwiat, Phys. Rev. A **65**, 012301 (2001).

[43] Y. S. Zhang, Y. F. Huang, C. F. Li, and G. C. Guo, Phys. Rev. A **66**, 062315 (2002).

[44] W. J. Munro, D. F. V. James, A. G. White, and P. G. Kwiat, Phys. Rev. A **64**, R030302 (2001).

[45] S. Ishizaka and T. Hiroshima, Phys. Rev. A **62**, 022310 (2001).

[46] F. Verstraete, K. Audenaert, and B. DeMoor, Phys. Rev. A **64**, 012316 (2001).

[47] C. H. Bennett, H. J. Bernstein, S. Popescu, and B. Schumacher, Phys. Rev. A **53**, 2046 (1996).

[48] P. G. Kwiat, S. Barraza-Lopez, A. Stefanov, and N. Gisin, Nature **409**, 1014 (2001).

[49] R. T. Thew and W. J. Munro, Phys. Rev. A **63**, R030302 (2001).

[50] J. W. Pan, C. Simon, Č. Brukner, and A. Zeilinger, Nature **410**, 1067 (2001); J. W. Pan *et al.*, Nature **423** 417 (2003); Z. Zhao *et al.*, Phys. Rev. Lett. **90** 207901 (2003).

[51] T. Yamamoto, M. Koashi, S. K. Özdemir, and N. Imoto, Nature **421**, 343 (2003).

[52] N. A. Peters *et al.*, Phys. Rev. Lett. **92**, 133601 (2004).

[53] N. A. Peters, T.-C. Wei, and P. G. Kwiat, Proc. of SPIE Fluc. and Noise **5468**, 269 (2004).

[54] A. J. Berglund, Dartmouth College B.A. Thesis, also quant-ph/0010001 (2000); N. A. Peters *et al.*, J. Quant. Inf. Comp. **3**, 503 (2003).

[55] M. Barbieri, F. DeMartini, G. DiNepi, and P. Mataloni, Phys. Rev. Lett. **92**, 177901 (2004).

[56] J. B. Altepeter, D. F. V. James and P. G. Kwiat, Chapter 3 in *Quantum state estimation*, M. Paris and J. Rehacek, Eds., Springer-Verlag (2004).

[57] C. H. Bennett *et al.*, Phys. Rev. Lett. **76**, 722 (1996).

[58] N. A. Peters *et al.*, Phys. Rev. Lett. **96**, 159901 (2006).

[59] A. Kent, Phys. Rev. Lett. **81**, 2839 (1998).

[60] F. Verstraete and H. Verschelde, Phys. Rev. Lett. **90**, 097901 (2003).

[61] N. Gisin and S. Massar, Phys. Rev. Lett. **79**, 2153 (1997).

[62] W. K. Wooters, Phys. Rev. Lett. **80**, 2245 (1998).

[63] V. Coffman, J. Kundu, and W. K. Wooters, Phys. Rev. A **61**, 052306 (2000).

[64] R. F. Werner, Phys. Rev. A **40**, 4277 (1989).

[65] N. A. Peters, T.-C. Wei, and P. G. Kwiat, Phys. Rev. A **70**, 052309 (2004).

[66] M. A. Nielsen and I. L. Chuang, *Quantum Computation and Quantum Information* (Cambridge University Press, Cambridge, U. K., 2000).

[67] F. Verstraete and H. Verschelde, Phys. Rev. A **66**, 022307 (2002).

[68] M. Horodecki, P. Horodecki, and R. Horodecki, Phys. Rev. Lett. **78**, 574 (1997).

[69] E. Knill, R. Laflamme, and W. H. Zurek, Science **279**, 574 (1998).

[70] H.-K. Lo, Phys. Rev. A **62**, 012313 (2000).

[71] A. K. Pati, Phys. Rev. A **63**, 014302 (2001).

[72] C. H. Bennett *et al.*, Phys. Rev. Lett. **87**, 077902 (2001).

[73] X. Peng *et al.*, *Phys. Lett. A*, **306**, 271, (2003) ("remote" here means from one side of a molecule to the other).

[74] S. A. Babichev, B. Brezger, and A. I. Lvovsky, Phys. Rev. Lett. **92**, 047903 (2004).

[75] N. A. Peters *et al.*, Phys. Rev. Lett. **95**, 150502 (2005).

[76] E. Jeffrey, N. A. Peters, and P. G. Kwiat, New J. Phys. **6**, 100 (2004).

[77] N. A. Peters *et al.*, Proc. of SPIE Optics and Photonics **5893**, 589308 (2005).

[78] D. Bouwmeester *et al.*, Nature **390**, 575 (1997).

[79] D. Boschi *et al.*, Phys. Rev. Lett. **80**, 1121 (1998).

[80] V. Buzek, M. Hillery, and R. F. Werner, Phys. Rev. A **60**, R2626 (1999).

[81] P. G. Kwiat and B.-G. Englert, in *Science and Ultimate Reality: Quantum Theory, Cosmology and Complexity*, J. D. Barrow, P. C. W. Davies, and C. L. Harper, Jr., Eds., Cambridge Univ. Press (2004).

[82] D. W. Berry and B. C. Sanders, Phys. Rev. Lett. **90**, 057901 (2003).

[83] G.-Y. Xiang *et al.*, Phys. Rev. A **72**, 012315 (2005).

[84] R. Raussendorf and H. J. Briegel, Phys. Rev. Lett. **86**, 5188 (2001).

[85] P. Walther *et al.*, Nature (London) **434**, 169 (2005).

[86] S. Pancharatnam, Proc. Ind. Acad. Sci. A **44**, 247 (1956).

[87] M. V. Berry, Proc. Roy. Soc. A **392**, 45 (1984).

[88] P. G. Kwiat and R. Y. Chiao, Phys. Rev. Lett. **66**, 588 (1991).

[89] J. Brendel and W. D. W. Martienssen, Phys. Rev. A **52**, 2551 (1995).

[90] D. V. Strekalov and Y. H. Shih, Phys. Rev. A **56**, 3129 (1997).

[91] D. Suter, K. T. Mueller, and A. Pines, Phys. Rev. Lett. **60**, 1218 (1988).

[92] J. A. Jones, V. Vedral, A. Ekert, and G. Castagnoli, Nature **403**, 869 (2000).

[93] P. Zanardi and M. Rasetti, Phys. Lett. A **264**, 94 (1999).

[94] L. M. Duan, J. I. Cirac, and P. Zoller, Science **292**, 1695 (2001).

[95] S.-L. Zhu and Z. D. Wang, Phys. Rev. Lett. **91**, 187902 (2003).

[96] E. Sjöqvist *et al.*, Phys. Rev. Lett. **85**, 2845 (2000).

[97] J. Du *et al.*, Phys. Rev. Lett. **91**, 100403 (2003).

[98] M. Ericsson *et al.*, Phys. Rev. Lett. **94**, 050401 (2005).

[99] E. Knill, R. Laflamme, and G. Milburn, Nature **409**, 46 (2001).

[100] T. B. Pittman, B. C. Jacobs, and J. D. Franson, Phys. Rev. Lett. **88**, 257902 (2002).

[101] T. B. Pittman *et al.*, Phys. Rev. A **68**, 032316 (2003).

[102] J. L. O'Brien *et al.*, Nature **426**, 264 (2003).

[103] A. Uhlmann, Rep. Math. Phys. **24**, 229 (1986).

[104] M. A. Nielsen and I. L. Chuang, in *Quantum Computation and Quantum Information* (Cambridge University Press, Cambridge, U. K., 2000), pp. 109–111.

[105] M. Ericsson *et al.*, Phys. Rev. Lett. **91**, 090405 (2003).

[106] F. Wilczek and A. Zee, Phys. Rev. Lett. **52**, 2111 (1984).

[107] J. Pachos, P. Zanardi, and M. Rasetti, Phys. Rev. A **61**, 010305(R) (1999).

[108] N. Gisin, G. Ribordy, W. Tittel, and H. Zbinden, Rev. Mod. Phys. **74**, 145 (2002).

[109] A. K. Ekert, Phys. Rev. Lett. **67**, 661 (1991).

[110] Z. Zhao *et al.*, Nature **430**, 54 (2004).

[111] C. Santori *et al.*, Phys. Rev. Lett. **86**, 1502 (2001).

[112] C. Kurtsiefer *et al.*, Phys. Rev. Lett. **85**, 290 (2000).

[113] A. Kuhn, M. Hennrich, and G. Rempe, Phys. Rev. Lett. **89**, 067901 (2002).

[114] P. Kumar *et al.*, Quantum Inf. Processing **3**, 215 (2004).

[115] T. B. Pittman, B. C. Jacobs, and J. D. Franson, Phys. Rev. A **66**, 042303 (2002).

[116] F. Paleari, A. Andreoni, G. Zambra, and M. Bondani, Optics Express **12**, 2816 (2004).

[117] S. Takeuchi, Optics Lett. **26**, 843 (2001).

[118] C. Kurtsiefer, M. Oberparleiter, and H. Weinfurter, J. Mod. Optics **48**, 1997 (2001).

[119] N. Boeuf *et al.*, Opt. Eng. **39**, 1016 (2000).

[120] D. Achilles *et al.*, J. Mod. Optics **54**, 1499 (2004).

[121] P. H. Eberhard *et al.*, in *Applications of Photonic Technology*, edited by G. A. Lampropoulous *et al.* (Plenum Press, New York, 1995), pp. 471–474.

[122] S. Takeuchi *et al.*, Appl. Phys. Lett. **74**, 902 (1999).

[123] V. G. Dmitriev, G. G. Gurzadyan, and D. N. Nikogosyan, *Handbook of Nonlinear Optical Crystals*, third, revised ed. (Springer-Verlag, Berlin Heidelberg New York, 1999).

Author's Biography

Nicholas A. Peters was born in Michigan on September 25, 1977. He received a B. A. Summa Cum Laude with Majors in Physics and Mathematics, and a minor in Computer Science from Hillsdale College in 2000. He entered the Ph.D. program in Physics at the University of Illinois at Urbana-Champaign in 2000, earning an M.S. in 2002. He is married to Theresa Marie Peters.

List of Publications

1. P. Kwiat, J. Altepeter, D. Branning, E. Jeffrey, N. Peters and T.-C. Wei, “Taming Entanglement,” Proc. of the 6th Int. Conf. on Quant. Comm. Meas. and Comp. J.H. Shapiro and O. Hirota, eds. 117, (Rinton Press, 2003); quant-ph/0303040 (2003).
2. N. Peters, J. Altepeter, D. Branning, E. Jeffrey and P. Kwiat, “Precise creation, characterization, and manipulation of single optical qubits,” Quant. Info. and Comp. **3**, 503 (2003).
3. P. G. Kwiat, J. Altepeter, J. Barreiro, D. A. Branning, E. R. Jeffrey, N. Peters and A. P. VanDevender, “Optical technologies for quantum information science,” Proc. SPIE Int. Soc. Opt. Eng. **5161**, 87 (2004).
4. N. A. Peters, J. B. Altepeter, D. Branning, E. R. Jeffrey, T.-C. Wei and P. G. Kwiat, “Maximally entangled mixed states: Creation and concentration,” Phys. Rev. Lett. **92**, 133601 (2004); N. A. Peters, J. B. Altepeter, D. Branning, E. R. Jeffrey, T.-C. Wei and P. G. Kwiat, “Erratum: Maximally Entangled Mixed States: Creation and Concentration [Phys. Rev. Lett. **92**, 133601 (2004)],” ibid. **96**, 159901 (2006).
5. E. Jeffrey, N. A. Peters and P. G. Kwiat, “Towards a periodic deterministic source of arbitrary single-photon states,” New J. of Physics **6**, 100 (2004).
6. N. A. Peters, T.-C. Wei and P. G. Kwiat, “Benchmarking and Procrustean noise reduction of entangled mixed states,” Proc. SPIE Int. Soc. Opt. Eng. **5468**, 269 (2004).
7. N. A. Peters, T.-C. Wei and P.G. Kwiat, “Mixed state sensitivity of several quantum information benchmarks,” Phys. Rev. A **70**, 052309 (2004).
8. M. Ericsson, D. Achilles, J. T. Barreiro, D. Branning, N. A. Peters and P. G. Kwiat, “Geometric phase for mixed states using single-photon interferometry,” AIP Conf. Proc. **734**, 370

(2004).

9. P. G. Kwiat, J. B. Altepeter, J. T. Barreiro, M. E. Goggin, E. Jeffrey, N. A. Peters and A. P. VanDevender, “The conversion revolution: down, up and sideways,” AIP Conf. Proc. **734**, 337 (2004).
10. M. Ericsson, D. Achilles, J. T. Barreiro, D. Branning, N. A. Peters and P. G. Kwiat, “Measurement of geometric phase for mixed states using single photon interferometry,” Phys. Rev. Lett. **94**, 050401 (2005).
11. T.-C. Wei, J. B. Altepeter, D. Branning, P. M. Goldbart, D. F. V. James, E. Jeffrey, P. G. Kwiat, S. Mukhopadhyay and N. A. Peters, “Schemes for synthesizing arbitrary two-photon polarization mixed states,” Phys. Rev. A **71**, 032329 (2005).
12. N. A. Peters, J. T. Barreiro, M. E. Goggin, T.-C. Wei and P. G. Kwiat, “Remote state preparation: Arbitrary remote control of photon polarization,” Phys. Rev. Lett. **94**, 150502 (2005).
13. N. A. Peters, J. T. Barreiro, M. E. Goggin, T.-C. Wei and P. G. Kwiat, “Remote state preparation: arbitrary remote control of photon polarizations for quantum communication,” Proc. SPIE Int. Soc. Opt. Eng. **5893**, 589308 (2005).
14. J. T. Barreiro, N. K. Langford, N. A. Peters and P. G. Kwiat, “Generation of hyperentangled photons,” Phys. Rev. Lett. **95**, 260501 (2005).
15. O. Hosten, M. T. Rakher, J. T. Barreiro, N. A. Peters and P. G. Kwiat, “Counterfactual quantum computation via quantum interrogation,” Nature **439**, 949 (2006).